THE UNIVERSITY OF CHICAGO

ENERGY DISSIPATION CONTROLS EMERGENT ORDER IN MODEL DRIVEN LIQUIDS AND BIOCHEMICAL CLOCKS

A DISSERTATION SUBMITTED TO
THE FACULTY OF THE DIVISION OF THE PHYSICAL SCIENCES
IN CANDIDACY FOR THE DEGREE OF
DOCTOR OF PHILOSOPHY

DEPARTMENT OF CHEMISTRY

BY
CLARA ELISABETH DEL JUNCO

CHICAGO, ILLINOIS
AUGUST 2020

In memory of Andrés del Junco

[...] We are all chimeras, theorized and fabricated hybrids of machine and organism; in short, we are cyborgs.

—Donna Haraway, *A Cyborg Manifesto*

Table of Contents

List of Figures

List of Tables

Acknowledgments

Thanks to Suri for being an unfailingly encouraging advisor, for always overestimating me, for accepting if not understanding my need for schedules and structure and space. For allowing me to be a full person, politics, frustrations, emotions, etc. I am inspired by your creativity and generosity.

Thanks to Vaikuntanathan lab members and alumni, for creating a positive and sympathetic group culture and for patiently listening to me talk about why capitalism is bad for so many hours of group lunches. I hope I've convinced you.

Thanks to my committee, Aaron and Margaret, for your support and for your inspiring research. Thanks to postdocs of the James Franck Institute past and present, Sofia, Kinjal, and Kabir, for kind help and stimulating discussions. Merci à André et aux membres du Laboratoire Jean Perrin pour votre chaleureux accueil. Vous m'avez fait voir la place—et la nécessité—des prises de position radicales en science.

À Mathilde: tu me connais mieux que personne à Chicago et je n'aurais jamais pu survivre ces années sans ton amitié. Tu me pousses à vivre mes valeurs. Thanks to Ella for workouts and raves, incisive and insane ideas. I look forward to many more years of scheduled friendship. Thanks to Andrew for making me laugh, making me vegan, and for reminding me to get out of Hyde ParK, let loose and be ridiculous—always with integrity. Thanks to Becca for being my first intentional friend, for commiserating about chemistry, for valuing the things that it does not value and for having the faith and energy to try to change it. Thanks to Elena, for taking me to a trauma center campaign meeting on my first night in Chicago—teaching me early to mistrust UChicago—and for dinners, a shared love of dance and a shared family history. Thanks to Catherine, my twin flame.

To my GSU comrades: without the purpose and community of our union struggle, I would have left my PhD years ago. Organizing in the initially hostile environment of chemistry was a terrifying experience, but without it I never would have found the people who give me hope that we can move the needle, or maybe, burn it all down: Jonathan Fetherolf,

Elizabeth Bain, Bodhi Vani, Jake Higgins, and (happily) too many others to name.

To Bowers: thank you for feeding me, keeping me company through coronavirus, and showing me the joys and challenges of close community, poetry, DIY haircuts.

Thanks to Paula and Nina, with whom I have become so much closer over the past few years, for your unconditional love and support. I am deeply grateful to have you.

To my extended rave family, in Chicago and around the world—thanks for teaching me to know what I want and for endless hours of joy.

Thanks to the Collège crew for enduring friendship through change. Special thanks to Emma, who on top of science fiction and fantasy recommendations, provided her invaluable editing services on this dissertation.

Thanks to NTS radio for being my companion through long hours of work and frustration.

Throughout this dissertation, I use the pronoun "we" in describing research. This is a convention and communicates that the work was coauthored—but beyond that, it acknowledges that research is never done in a vacuum. Thanks to all those not explicitly named who have provided the material conditions for my intellectual production, the emotional support for my intellectual labor. I couldn't have done it without you.

While carrying out the research in this dissertation, I was financially supported by a Natural Sciences and Engineering Research Council of Canada Postgraduate Scholarship - Doctoral; by the University of Chicago John C. Light Fellowship in Theoretical Chemistry; and by the National Science Foundation (NSF) through the University of Chicago Materials Research Science and Engineering Center, which is funded by NSF Award DMR-1420709.

Abstract

Thermodynamic equilibrium is a strong constraint on the statistics of physical systems that has led to a correspondingly powerful theory, equilibrium statistical mechanics, that connects microscopic forces to macroscopic properties. Experiments now confirm the longstanding speculation that living systems can be fruitfully modeled using physical principles, and the challenge is to develop statistical mechanics for such systems, which violate thermodynamic equilibrium. Progress in nonequilibrium statistical mechanics has been made by focusing on energy dissipation, the amount of energy consumed via currents of work and heat. In this dissertation I look at energy dissipation in two systems displaying fundamentally nonequilibrium collective behavior in order to understand, quantitatively and qualitatively, how nonequilibrium driving produces this behavior.

First, I explore the relation between dissipation and changes in the structure and transport properties of a minimal, chiral driven liquid that undergoes nonequilibrium phase separation. The model mimics recent experiments that use an external magnetic field to reversibly break symmetry and phase separate liquids of colloidal particles. These and other similar experiments are in turn broadly inspired by biological "active matter" systems such as bacterial swarms. Using concepts from stochastic thermodynamics and liquid state theories, I show how the work performed on the system by various nonconservative, time-dependent forces—which represents the nontrivial contribution to the energy dissipation—modifies the force fluctuations and diffusion of the liquid, leading to phase separation. I then characterize interfaces in the phase-separated state, showing that they exhibit fluctuations unlike those seen in equilibrium systems.

Second, I explore how energy dissipation enables precise timing in minimal Markov state models of biological clocks known generically as biochemical oscillators. These oscillators are ubiquitous in biology and allow organisms to properly time their biological functions. Using a transfer matrix perturbation theory, I obtain analytical expressions for the coherence and period of oscillations in single-cycle Markov models that reveal that higher energy dissipation

enables higher precision of both quantities among a population of oscillators with randomly distributed rates. I then develop a mapping based on first passage time distribution between models with multiple small cycles and single-cycle models. The mapping allows the analytical theory to be extended to multi-cycle oscillators, revealing that energy dissipation also enables robust timing among a population of oscillators with different topologies.

The case studies presented here demonstrate how energy dissipation enables precise and adaptive collective behavior in nonequilibrium systems.

Chapter 1

Introduction

The power of statistical mechanics as an approach lies in the idea that the macroscopic properties of equilibrium systems are determined by a competition between enthalpy and entropy, and that we can in principle derive these properties from the microscopic interactions between particles. By extension, we should be able to design materials by designing microscopic interactions. Yet the vast majority of systems of interest consume energy and are out of equilibrium, and for this broad class of systems no such principle exists. In particular, evolution has produced a whole host of incredible machines and materials, from self-healing materials like muscles and skin to the artificial intelligence of the adaptive immune system [80, 109]. In order to fully appreciate the remarkable properties of these naturally occurring systems, and perhaps reproduce them in engineered systems, we need a rigorous physical understanding of how they convert energy input to function. In this dissertation, I contribute to that understanding by describing how energy consumption controls the properties of two model systems inspired by contemporary experiments.

Two classes of systems that illustrate the desirable features of nonequilibrium systems are active matter and biochemical oscillators. Active matter refers to systems composed of active or driven individual components, so that constant energy input is necessary. Active matter shows up at all scales in biology: flocks of starlings [3], swarms of bacteria [37], and the molecular motors that make up the cell cytoskeleton [45] are popular examples. These systems are *self-organized* and *adaptive*—they can respond to changes in their environments to either maintain a steady state in the presence of perturbations or reconfigure [4]. Biochemical oscillators are built-in biological clocks that allow organisms to precisely time development and metabolic changes in order to optimize fitness [151]. Underlying these clocks are series of stochastically timed processes, mainly chemical reactions, yet they maintain precise timing under many conditions [63]: biochemical oscillators can *perform stochastic tasks in a highly reproducible manner*.

Many other examples in biology and, now, experiments, have similar properties. For instance, experimentalists can now design colloidal particles that phase separate, assemble, and reconfigure when exposed to different stimuli [99, 130], and DNA copying has built-in error correction to ensure fast and precise replication [57, 94, 88]. How adaptation and precision are achieved depends on the details of the system in question. What they all require, however, is dissipation: the process of constantly consuming energy via currents of work and heat. Because it is so general, dissipation seems to be a good starting point to develop general theories for nonequilibrium systems ranging from active and driven liquids to circadian oscillators. Moreover, dissipation has historically been a central concept in established branches of nonequilibrium physics that have proven successful in describing macroscopic and microscopic systems.

At a macroscopic scale, dissipation shows up in a framework known as linear irreversible thermodynamics, which provides the theoretical basis for the linear constitutive equations, an essential ingredient of hydrodynamic theories. We begin with the balance equation for the entropy, which expresses that the entropy of a volume element can change by flowing into or out of the volume element, or via *dissipative* processes occurring inside it [61]. The entropy produced per unit time per unit volume, σ, by these dissipative processes is always a sum of thermodynamic fluxes $\mathbf{J_i}$ (such as a flow of mass) and conjugate thermodynamic forces $\mathbf{X_i}$ (such as a pressure gradient) [25]:

$$\sigma = \sum_i \mathbf{J}_i \cdot \mathbf{X}_i. \tag{1.1}$$

An important postulate is then that the forces and fluxes are linearly related [61]:

$$\mathbf{J}_i = \sum_j L_{ij} \mathbf{X}_i. \tag{1.2}$$

The L_{ij} objects are transport coefficients such as the diffusion constant. When combined with the appropriate conservation equations for energy, mass, momentum, and angular mo-

mentum, these linear constitutive relations give the Navier-Stokes equations [25, 61], a closed set of hydrodynamic equations characterizing the nonequilibrium system at long time and length scales. These descriptions have proven remarkably successful at characterizing not only relatively "simple" liquids such as water [61] but also more complex systems. For instance, increased interest and experimental studies of the cell cytoskeleton have led to efforts to theoretically model systems of filamentous proteins and motors [78, 66], which are anisotropic and dissipate energy on the single-particle level. Linear irreversible thermodynamics has allowed hydrodynamic theories that successfully describe the large scale flows in these "active nematic gels" [78, 66].

At the microscopic scale, where thermal noise is important, stochastic thermodynamics has used master equation descriptions of Markovian processes to show how dissipation encodes the irreversibility of a process. A simple and powerful result due to Crooks [23] relates the relative probabilities of a forward and a reverse trajectory of a stochastic driven system to the entropy production along that trajectory,

$$\frac{P_F(+\sigma)}{P_R(-\sigma)} = e^{\sigma}, \tag{1.3}$$

where σ is the entropy production of the system over some time interval, $P_F(+\sigma)$ is the probability of observing entropy production σ, and $P_R(-\sigma)$ is the probability of observing entropy production $-\sigma$ with the dynamics reversed in time. One important implication of this fluctuation theorem is the Jarzynski equality [62],

$$\langle \exp(-\beta W) \rangle = \exp(-\beta \Delta F), \tag{1.4}$$

where $\Delta F = F_B - F_A$ is the free-energy difference between equilibrated states of a system with parameter values A and B (such as the volume or strength of an external electric field), W is the work done along a trajectory going from state A to state B, and angle brackets denote an average over an ensemble of trajectories. Equation 1.4 shows that equilibrium free-

energy differences can be calculated from nonequilibrium trajectories. Practically, among many other applications and extensions, the Jarzynski equality gives a route to experimental measurement of free-energy profiles of protein folding [60].

Motivated by and drawing on these approaches, this dissertation explores how energy dissipation and other closely related quantities such as work, entropy production, and driving forces control the properties of models of a driven liquid and biochemical oscillator.

Chapter 2 describes my research on the driven liquid. I present a model of a system of particles inspired by recent quasi-2D experiments in which colloids are controlled by a rotating magnetic field that causes them to orbit in the plane [49]. In equilibrium, these particles act as a fluid of hard spheres, a well-characterized system that exists in one state at a fixed density. When exposed to the magnetic field, however, they spontaneously break symmetry and sort themselves according to the chirality of their orbit—a simple example of self-assembly. A whole phase diagram thus emerges from a single point in the equilibrium phase space. If we can understand how driving the system out of equilibrium modifies the collective properties of the particles, this phenomenon could be exploited to, for example, achieve completely reversible self-assembly without having to modify the chemistry of the system.

Chapter 3 describes my research on a model of a biochemical oscillator. A biochemical oscillator is a series of chemical reactions and physical processes that result in cyclical changes in the levels of certain molecules that underlie biological clocks such as circadian rhythms. It can be easily demonstrated that such cyclical processes cannot occur in equilibrium—like most of life, oscillations require energy. Biochemical oscillators are known to be remarkably robust to fluctuations in the chemical counts, changes in the inputs to the system such as light levels and temperatures, and other sources of noise [63]. How does energy dissipation enable this robustness? In the past decade, experiments have been developed that allow measurement of the response of the KaiC oscillator—the circadian clock of the photosynthetic cyanobacterium *Synechococcus elongatus*—to changes in ATP levels, light cues, gene

knockdowns, and other inputs, both in vivo at the population and single-cell levels as well as in vitro [89, 138, 117, 118]. These quantitative measurements relating energy consumption and other inputs to the timekeeping abilities of the oscillator allow comparison of physical predictions to experiments.

The unifying theme of the research presented here is the focus on dissipation as both a quantification of the distance of the system from equilibrium and a knob that tunes the properties of interest. In the details, however, the two case studies explored here (a driven liquid and a biochemical oscillator) have little in common: one exists in continuous space, the other in discrete space; one is a many-body problem, the other is a process that is effectively treated as a one-body problem. In order to arrive at connections between dissipation, structure, and dynamics, we have needed to choose different numerical and theoretical tools based the details of each system. The approaches and the results of the work in this dissertation thus illustrate the scope of the challenges posed—and opportunities afforded—by the forefront of biological and chemical experiments, and how they can be addressed using nonequilibrium statistical mechanics. Through a detailed study of these two specific systems, we draw general lessons about the relationship between organization and energy consumption in chemical and biological systems.

Chapter 2

Effect of dissipation on density, force, and interface fluctuations in a driven liquid

The material in this chapter is adapted with permission from the following publications:

[29] del Junco, C.; Tociu, L.; Vaikuntanathan, S. Energy dissipation and fluctuations in a driven liquid. *Proc. Natl. Acad. Sci. U. S. A.*, 115(14):3569–3574, **2018**.

[30] del Junco, C.; Vaikuntanathan, S. Interface height fluctuations and surface tension of driven liquids with time-dependent dynamics. *J. Chem. Phys.*, 150(9):094708, **2019**.

2.1 Introduction

The first system that we study belongs to the category of active or driven matter. Minimal models of active matter have provided an analytically and computationally tractable test bed to study nonequilibrium systems. Inspired by naturally occurring collections of active units that exhibit collective phenomena such as flocks of birds [3] and swarming bacteria [37], physicists have begun to build models to ask what the minimal ingredients for observing these behaviors are and how they can be described theoretically within our existing languages for collective phenomena. Of particular interest are phase transitions and the properties that characterize them, like mechanical equilibria and interfaces. These minimal models can be computational or experimental, with the latter often consisting of colloidal particles (where thermal motion is still important) functionalized in a range of clever ways to self-propel [17] and/or respond to outside stimulus from light [99] or magnetic fields [49, 130]. (A distinction can be made between "active" particles that are self-propelled and "driven" particles that are enslaved to an external driving field; here we will use "active" as a generic term to refer to both of these categories and "driven" to refer to the latter case).

Examples of nonequilibrium phase separation include motility-induced phase separation

(MIPS), undergone by Brownian particles when they are given the ability to self-propel [40, 110, 11, 20, 132, 148], lane or stripe formation of shaken granular matter [87, 106] or of charged particles in an electric field [38, 152, 146, 145, 67], and the separation of particles with rotational dynamics based on phase synchronization [75] or chirality [93, 49, 154]. Some aspects of these phase transitions, especially MIPS, are beginning to be characterized theoretically [133, 131, 134]: recent work has studied nucleation phenomena [114, 111] and obtained expressions for pressure and other mechanical properties of active media [129, 12]. However, in many cases energy consumption causes traditional definitions to break down—for instance, pressure is not generically a state function in active particles and depends on the shape of the particles and the system boundary [129]. In the case of MIPS, both negative and positive surface tensions have been measured in a phase-separated system [12, 55], defying both intuition and internal consistency. Clearly, in spite of recent advances, understanding how energy consumption induces phase separation and modifies the structure of active and driven systems remains a challenging open problem [8].

Another approach is to focus on entropy production. As in discrete systems whose dynamics are described by master equations, the entropy production can be formally defined based on the microscopic dynamics of active particles in terms of the ratio of forward to reverse trajectories [77, 43, 126]. The path probabilities must now be calculated using path integrals, making this a more challenging problem than for master equation dynamics but one that has been successfully addressed in the literature [77, 43, 126], showing that entropy production is of practical use in quantifying the nonequilibrium nature of minimal models of active matter.

The remaining step is to connect entropy production to material properties such as viscosity and surface tension in active matter. An important contribution to the entropy production is the work [126, 91], defined as the system-averaged inner product of the driving force on a particle with the particle displacement. In this chapter, we study the relation between the work and the structure and dynamics of a model nonequilibrium liquid driven by

time-periodic forces. The rotational dynamics that result from the time-periodic forces have similarities with a range of systems, including colloids in a periodically changing magnetic or electric field [153, 49, 152, 145], shaken plastic particles and chiral wires [47, 139], and chemical and biological microswimmers with active rotational degrees of freedom [69, 103]. Despite their relevance to a wide range of experimental and biological systems, model systems with rotational dynamics have only recently begun to be studied [144, 93, 24].

First, in Section 2.2 we introduce the model in detail. It consists of particles with diffusive dynamics and purely repulsive interactions, a system that is well understood at equilibrium and does not exhibit any kind of phase separation. To half of the particles, we apply a rotating force characterized by its amplitude and frequency. Holding the density fixed, we explore the phase space of the system along the dimensions of amplitude and frequency. Initially mixed, driven and undriven particles phase separate as the driving is increased and then remix with very strong driving. In the phase-separated state, particle currents that flow tangential to the interface decay rapidly into the bulk, and the statistics of interface height fluctuations disagree with expectations for equilibrium interfaces. An intuitive picture of the phase separation is that it occurs because driving forces induce collisions between unlike particles, which effectively increases the diffusion coefficient in regions that are mixed compared to regions that are pure. This imbalance causes particles to diffuse from mixed regions to pure regions, resulting in phase separation. Motivated by this rough understanding, we sought to thoroughly characterize how the driving forces increase diffusion, causing phase separation, and how they determine the properties of the resulting interfaces.

In Section 2.3 we study the region of the phase diagram up to and including the phase transition from a mixed state to an unmixed state. We develop a series of theoretical descriptions for the energy dissipation and diffusion in this system that rely on the observation that in this region, even for values of energy dissipation that are many k_BT per cycle of the driving, the system remains in many ways near equilibrium in terms of its theoretical

description. We are thus able to understand the location of the phase boundary in the space of the driving force parameters.

In Section 2.4 we study the interfaces in the phase-separated region. We introduce a variation on the driven liquid model in which some particles have attractive interactions that does display phase separation at equilibrium. This provides a reference state that allows us to better understand how the interfaces are modified by the driving forces. We define the surface tension of the interface using capillary wave theory, which does not depend on definitions of pressure but rather uses the spectrum of interface fluctuations, which can be unambiguously measured regardless of the underlying dynamics. We find that the surface tension can be dramatically increased by turning on driving forces, demonstrating the possibility of using external driving to stabilize self-assembled structures.

In this chapter we take several important steps toward understanding chiral driven systems. Yet despite the rather general conclusion that energy dissipation renormalizes static and dynamic properties of driven particle systems in a way that can be quantitatively understood, it remains unclear how our specific understanding of this system connects to the proliferating body of research about other minimal active and driven matter systems. Luckily, as the field of active matter research reaches 25 years of age, general principles are beginning to emerge that seem poised to encapsulate many of these discoveries. In Sections 2.3.7 and 2.4.6, we discuss future directions and recent theoretical advances that tie our work to other systems of chiral and nonchiral active and driven systems. These advances validate the generality of some aspects of the work in this chapter and show the insufficiency of others to capture the full nonequilibrium nature of our model. In particular, it has been found that dissipation is generically connected to changes in diffusion and effective interparticle potentials [137]. The authors of Ref. 137 also show that the driven system studied here can be mapped to an active system, so that this connection also holds in active particle systems. More broadly, the mapping suggests that the distinction often made in the literature between active and driven particles may not be that important for many purposes. In

the case of interfaces, a recently developed hydrodynamic theory for chiral liquids [130] may provide a framework for explaining the currents, increases in surface tension, and anomalous interface height statistics that we observed.

2.2 The model

2.2.1 Equations of motion and simulation parameters

Our model system is composed of 2D disks whose positions $\dot{\mathbf{r}}_\mathbf{i}(\mathbf{t})$ evolve in time according to driven Brownian dynamics due to

$$\dot{\mathbf{r}}_\mathbf{i}(t) = D_0\beta\left(\mathbf{F}_{\mathrm{c,i}}(t) + \mathbf{F}_{\mathrm{d}}(t)\right) + \boldsymbol{\eta}_i(t), \tag{2.1}$$

where D_0 is the bare, single-particle diffusion constant and $\boldsymbol{\eta}_i(t) = (\eta_{i,x}(t), \eta_{i,y}(t))$ are Gaussian-distributed random variables with $\langle\boldsymbol{\eta}_i(t)\rangle = 0$ and $\left\langle\eta_{i,\mu}(t)\eta_{j,\nu}(t')\right\rangle = 2D_0\delta_{i,j}\delta_{\mu,\nu}\delta(t-t')$. In all of our simulations and calculations, we set $\beta = 1/k_BT = 1$. $\mathbf{F}_{\mathrm{c,i}}$ is the conservative force on particle i. We begin, in Section 2.3, by considering a conservative force that is purely repulsive, the Weeks-Chandler-Andersen interaction potential [147],

$$u(r_{ij}) = \begin{cases} 4\epsilon\left[\left(\frac{r_0}{r_{ij}}\right)^{12} - \left(\frac{r_0}{r_{ij}}\right)^{6}\right] + \epsilon, & r \le 2^{1/6}r_0 \\ 0, & r > 2^{1/6}r_0 \end{cases}, \tag{2.2}$$

where r_0 is the particle size and ϵ is the interaction strength. In Section 2.4 we additionally use an attractive Lennard-Jones potential in some simulations [65]:

$$u(r_{ij}) = \begin{cases} 4\epsilon_{\mathrm{LJ}}\left[\left(\frac{r_0}{r_{ij}}\right)^{12} - \left(\frac{r_0}{r_{ij}}\right)^{6}\right], & r \le 2.5r_0 \\ 0, & r > 2.5r_0 \end{cases}, \tag{2.3}$$

with $\epsilon_{\mathrm{LJ}} = 2.25$.

The time scale is set by $t_0 = r_0^2/D_0$. The friction coefficient (γ), D_0, and r_0 are all set to

1 in our simulations. LAMMPS [105] was used to integrate the equations of motion. Unless otherwise indicated, results are reported for a number density $\rho = N/L^2 = 0.45$, where N is the number of particles in the simulation box of dimensions $L \times L$. In addition to the conservative forces, a fraction f (typically 0.5) of the particles are driven by an external force acting on the center of mass of the particle whose direction changes periodically in time according to

$$\mathbf{F}_{\mathrm{d}} = A(\sin\theta\hat{e}_x + \cos\theta\hat{e}_y) \tag{2.4}$$

$$\theta = 2\pi t/\tau, \tag{2.5}$$

where A is an amplitude with units of force and τ is the period. For the other $N(1-f)$ particles, $\mathbf{F}_{\mathrm{d}} = 0$. Thus, in the zero-temperature limit, a single driven particle will trace a circle in the plane. $\mathbf{F}_{\mathrm{d}}$ is the same for all driven particles, so that if we move to a frame of reference that is rotating with $\mathbf{F}_{\mathrm{d}}$, a pure system of driven particles will look the same as the equilibrium system. This model was motivated in part by a recent experimental active matter system developed by Han, Yan, Granick, and Luijten [49]. To verify our results, we also ran some simulations where the dissipative forces acting on the active particles were not in phase (Section 2.3); for these simulations, the angle of the dissipative force was updated using

$$\theta = 2\pi t/\tau + \theta_0, \tag{2.6}$$

where θ_0 was a random number uniformly distributed between 0 and 2π.

2.2.2 Phase diagrams

The amplitude of the driving force in Eq. 2.4 is quantified by the Péclet number, a dimensionless measure of the ratio of advective to diffusive velocity in the system. Here we define it as $\mathrm{Pe} = \frac{A/\gamma}{D_0/r_0}$. We constructed the phase diagram of the system as a function of Pe and τ at number densities $\rho = N/L^2 = 0.45$ and $\rho = 0.5$. For $\rho = 0.45$ ($\rho = 0.5$) we filled square

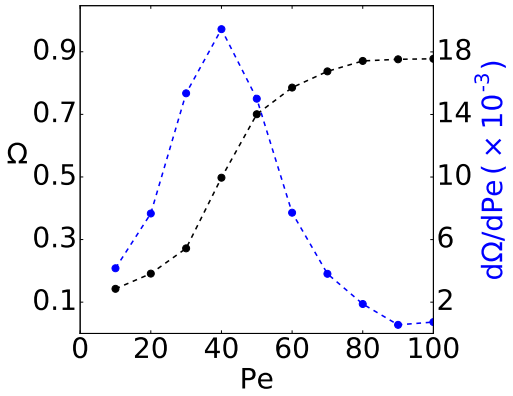

Figure 2.1: A representative plot of Ω and $\partial\Omega/\partial\mathrm{Pe}$ near the location of the lower phase transition in a system with $\rho = 0.45$, taken at a cross-section of the phase diagram where $\tau = 0.1$ with a probe volume with $r = 1.75r_0$. The value of Ω changes rapidly near the location of the transition, resulting in a sharp peak in $\partial\Omega/\partial\mathrm{Pe}$. Finite-size scaling analysis would be required to determine whether the value of Ω changes smoothly or jumps in the limit of a large simulation size. Dashed lines are guides for the eye.

simulation boxes of size $50r_0 \times 50r_0$ with periodic boundary conditions with 1,125 (1,250) particles with random initial positions. We scanned values of Pe from 10 to 160 and τ from $0.05t_0$ to $0.3t_0$. Simulations were run with timestep $\Delta t = 10^{-6}t_0$ up to $t = 1,000t_0$. In Section 2.3 all results are for systems with $\rho = 0.45$ unless otherwise indicated; in Section 2.4 all results are for systems with $\rho = 0.5$ unless otherwise indicated.

To identify different phases in the system, we defined an order parameter Ω that measures the degree of segregation of driven and passive particles. To compute Ω, we randomly selected a number of small probe areas with radius $1.75r_0$ in the steady-state system. In each probe volume, we measured $|N_R - N_B|/N$, where N_R and N_B are the number of red and blue particles, respectively, and N is the total number of particles, to give a value between 0 and 1. We then averaged over probe areas and many frames. For a completely mixed system Ω is 0; for a completely separated system Ω is slightly lower than 1 due to the presence of interfaces. We chose a probe volume of radius $1.75r_0$, which is large enough for Ω to take on a range of values, but small enough that inhomogeneities are not all washed out. Since the value of Ω is sensitive to the size of the probe volume, we defined the location of the transition to be where $\partial\Omega/\partial\mathrm{Pe}$ at constant τ peaks (Fig. 2.1).

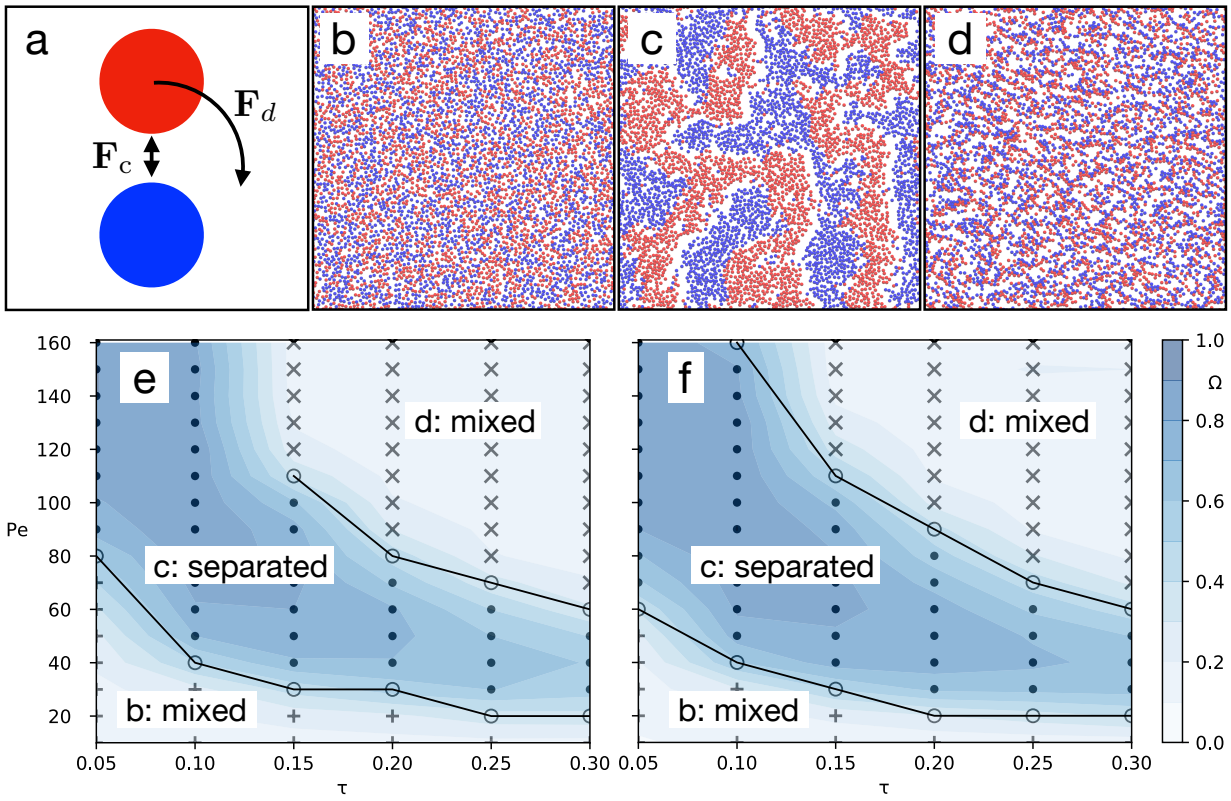

Figure 2.2: (a) Schematic of driven and undriven particles in the model. The particles interact via a repulsive Weeks-Chandler-Andersen potential (except in some cases in Section 2.4). Driven particles (red) additionally feel an external driving force that causes them to orbit in phase. (b–d) Snapshots of the final frame of a simulation in different regions of the phase diagram at $\rho = 0.45$ and (b) Pe $= 15$, $\tau = 0.1$; (c) Pe $= 70$, $\tau = 0.15$; and (d) Pe $= 150$, $\tau = 0.2$. (e–f) Phase diagrams of the system described by Eq. 2.1–2.5 at (e) $\rho = 0.45$ and (f) $\rho = 0.5$. At low Pe, the system is mixed (region *b*; plus signs). As Pe is increased, the system undergoes a transition to a phase-separated state (region *c*; points). As Pe is increased further, there is a transition to a mixed state characterized by large variations in local density (region *d*; crosses). Letters refer to representative snapshots in panels (b–d). The locations of the transitions are defined as the maxima of $\partial\Omega/\partial\mathrm{Pe}$ (black lines).

We found 3 distinct regimes in the part of Pe, τ space that we studied here (Fig. 2.2). At low Pe, driven and passive particles remain mixed and the system is homogeneous. As Pe is increased, they segregate into regions of purely driven or passive particles; the change is characterized by a very steep increase in Ω (Fig. 2.1). Similarly to other strongly damped active systems with rotating dynamics, the interfaces in the phase-separated system have no particular orientation, and there is a particle current along the interface that decays rapidly into the bulk [119, 130]; the interfaces in this system and a closely related one are the focus of Section 2.4. The steady state is time periodic with a period τ. As Pe is increased further, the system undergoes a transition to a mixed phase characterized by large variations in the local particle number density. As τ is increased, the segregated state persists over a smaller range of Pe.

We did not determine the order of this phase transition, but we note that interfaces in the phase-separated system (pictured in Fig. 2.2c) seem to possess a finite surface tension and merge to form a single stable system-spanning interface in the steady state. This result, together with the behavior of the order parameter shown in Fig. 2.1, suggests a first-order phase transition separating regions a and b. In Ref. 49 the authors describe a phase transition from a mixed state to an unmixed state in an equivalent system when the value of τ is decreased while the driving force on the particles is held constant, corresponding to passing from region c to region b in our phase diagram. They demonstrate that it is a bona fide first-order phase transition. The system in Ref. 49 has no random noise and so would not mix again at finite Pe; here, as a result of the finite temperature, we observe the second change from region b to a.

2.3 Dissipation, diffusion, and phase separation

2.3.1 Introduction

In this section, we investigate how the nonequilibrium forces modify the structural and transport properties of the liquid leading up to the lower transition from region a to b. Specifically, we are interested in the connection between the amount of energy the system receives as an input and the resultant steady state. As a first step, in Section 2.3.2 we show that the density fluctuations in our nonequilibrium system are surprisingly well described by Gaussian statistics [21]. Within this effective description, in Section 2.3.3 we are able to write down simple scaling relations for the amount of work performed on the system due to the nonequilibrium driving forces. These analytical predictions are validated by simulation data from many-particle systems. Then, in Section 2.3.4 we derive a relation that shows how the rate of work done on the system changes the fluctuations in the conservative forces experienced by the particles. In other words, our relation describes how energy dissipation changes the structural properties of the nonequilibrium material. This relation between work and force fluctuations can be viewed as an instantiation of the Harada-Sasa relation that connects work performed in a nonequilibrium system to a breakdown of the fluctuation-dissipation relation [52, 53]. We demonstrate this relation numerically for a variety of driven systems to firmly establish its general nature. In Section 2.3.5 we use a minimal model to demonstrate how a breakdown of the fluctuation-dissipation relation can change the diffusion constant of a system. While our driven liquid is substantially more complex than the minimal model, the model provides intuition for the interplay between dissipation and transport. In particular, it shows how a violation of the fluctuation-dissipation relation can lead to an increase in the diffusion constant. Finally, in Section 2.3.6 we show that such an enhancement of the diffusion constant can drive phase transitions in the liquid. Taken together, these results elucidate how a violation of time-reversal symmetry can be used to alter the structural, transport, and phase transition properties of a liquid.

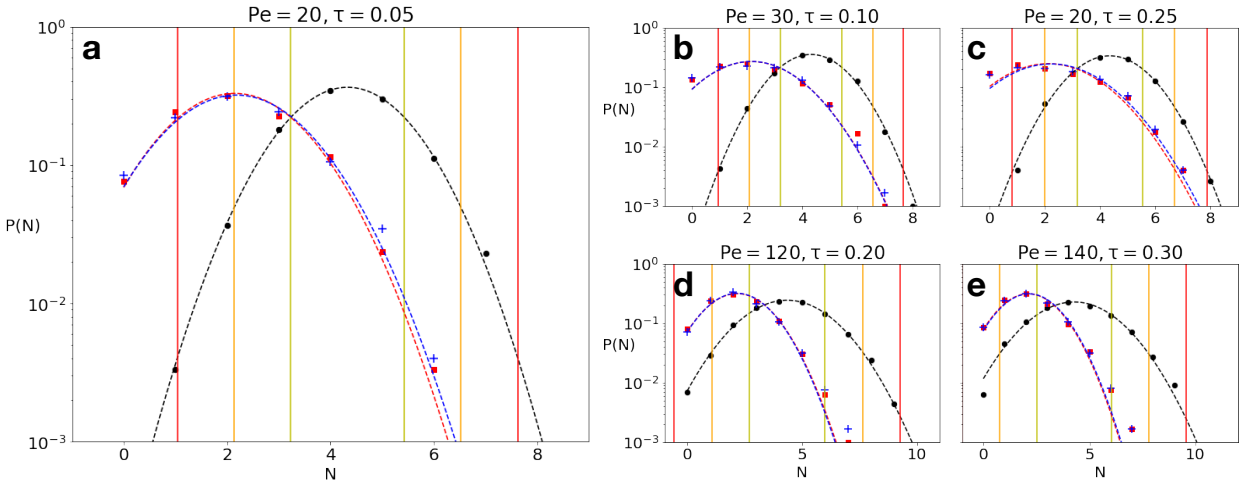

Figure 2.3: (a) Number density statistics for a system with Pe = 20, $\tau = 0.05$, where the order parameter Ω is close to zero. Points are the measured probability of finding N particles in a randomly selected probe volume of radius $1.75r_0$. Black points are the total number of particles, red squares are the number of driven particles, and blue plus signs are the number of inactive particles. Curves are Gaussian fits to data of the corresponding color. Yellow, orange, and red vertical lines are located at $\pm 1, 2, 3$ standard deviations, respectively, of the Gaussian fit from the mean. Error bars are smaller than the symbols. The density statistics are Gaussian to approximately $\pm 3\sigma$ from the mean. (b–c) Number density statistics for points near the top of the lower mixed region (region a in Fig. 2.2) and (d–e) in the high-drive mixed region (region c). Panels (b–c) demonstrate that the number density statistics remain Gaussian for values of Pe and τ that are closer to the transition from mixed to separated than the values of Pe and τ at which the work, force correlations, and diffusion are computed in this section.

2.3.2 Number density fluctuations

In many equilibrium liquids ranging from simple hard spheres to water, the statistics of fluctuations in the number of particles inside a small probe volume are surprisingly Gaussian [21, 59]. This property has enabled the development of quantitatively accurate theories for certain thermodynamic properties such as solvation energies [140, 142, 59]. A Gaussian description for density fluctuations also implies that changes in density due to external forces can be effectively captured within a linear response theory. In our context, linear response theory could help obtain relations between the driving forces and the energy supplied to the system.

To determine whether a Gaussian theory can describe the fluctuations out of equilibrium,

we measured the statistics of number density fluctuations in the driven liquid in a small probe volume [21, 59]. The number of particles N in a randomly selected probe volume of radius $1.75r_0$ was measured in 20 probe volumes per frame in the last 200 frames of each simulation, after the system had reached a steady state. The 4,000 resulting data points were binned to construct a histogram from which probabilities were computed.

We find that the probabilities are indeed Gaussian in the mixed regime below the line where the system first phase separates. Example histograms are shown in Fig. 2.3, demonstrating that the statistics remain Gaussian even for points that come close to the phase transition line and for points above the second phase transition. This finding is unexpected, since intuition and experience give us little reason to expect that the statistics would remain Gaussian out of equilibrium—for example, "giant" (i.e., non-Gaussian) number fluctuations have been observed in some active matter systems [90, 81, 99]. Yet we find Gaussian fluctuations for systems where on the order of $4kT$ of work is done per particle per cycle.

2.3.3 Definition and scaling of the work

The Gaussian nature of density fluctuations allows us to predict how the work performed on the nonequilibrium liquid scales with Pe and τ. Here, and in the rest of Section 2, we use the term *work* to denote the change in the energy of the system due to the action of nonconservative forces. This definition of work differs from commonly used conventions [52]. Specifically, we define the rate at which work is done on the system by the nonconservative forces as

$$\langle \dot{w} \rangle = -\frac{1}{N} \sum_{i=1}^{N} \frac{1}{\tau} \int \frac{\langle \mathbf{F}_{\mathrm{c},i}(t) \rangle \cdot \mathbf{F}_{\mathrm{d},i}(t)}{\gamma}. \tag{2.7}$$

As we will show in the subsequent sections, this definition of work is convenient to quantify the influence of the driving forces on the structural and transport properties of the system. We calculated the work from the same simulations used to construct the phase diagram by measuring $\langle \dot{w} \rangle = -\left\langle \mathbf{F}_{\mathrm{c,i}} \cdot \dot{\mathbf{r}}_{d,i} \right\rangle$, where $\dot{\mathbf{r}}_{d,i}$ is the rate of displacement of particle i due only

to the nonconservative forces in one timestep $\Delta t = 10^{-5} t_0$ and $\mathbf{F}_{\mathrm{c,i}}$ is the conservative force. The average is over particles. The values of $\langle \dot{w} \rangle$ reported below are means of the integral of $-\left\langle \mathbf{F}_{\mathrm{c,i}} \cdot \dot{\mathbf{r}}_{d,i} \right\rangle$ over a cycle divided by τ, giving an average rate. After the system reached its steady state, error bars were estimated using the standard deviation of the work values obtained over 100τ.

Given the Gaussian nature of density fluctuations, it is reasonable to speculate that the average restoring force, $\langle \mathbf{F}_{\mathrm{c,i}}(t) \rangle$ in Eq. 2.7 above, exerted by the system in response to the driving forces is a linear function of Pe. In the context of equilibrium liquids, Gaussian density fluctuations imply, within certain approximations [116, 27, 21, 68], that the coarse-grained field $\delta\rho(\mathbf{r}, t) = \rho(\mathbf{r}, t) - \bar{\rho}$, where $\bar{\rho}$ is the bulk density of the liquid, satisfies the following Gaussian equation of motion:

$$\dot{\delta\rho}(\mathbf{r}, t) = -\frac{K_G}{\gamma_G} \delta\rho(\mathbf{r}, t) + \eta_G(\mathbf{r}, t). \tag{2.8}$$

Here K_G is an effective spring constant, γ_G is an effective friction, and η_G is an effective noise with statistics $\langle \eta_G(t) \rangle = 0$ and $\left\langle \eta_G(t) \eta_G(t') \right\rangle = 2\delta(t - t')\delta(\mathbf{r} - \mathbf{r}')D_G$, with D_G an effective diffusion. Note that Eq. 2.8 does not conserve the density as it strictly should. The equivalent density-conserving equations of motion are available elsewhere [68]; as we will demonstrate, Eq. 2.8 is adequate for our purposes. Eq. 2.8 can be driven out of equilibrium by adding an extra driving term $\mathrm{Pe} F_{G,\mathrm{d}}(t)$ to it as follows:

$$\dot{\delta\rho}(\mathbf{r}, t) = -\frac{K_G}{\gamma_G} \delta\rho(\mathbf{r}, t) + \frac{\mathrm{Pe} F_{G,\mathrm{d}}(t)}{\gamma_G} + \eta_G(\mathbf{r}, t)\,. \tag{2.9}$$

Such a driving force has the effect of changing the local density and can mimic events where an active particle is driven into surrounding passive particles. The response of the system to this driving, $\langle \delta\rho \rangle$, scales linearly with Pe [58]. In this way, due to the Gaussian density fluctuations, we anticipate that the work performed on the system will be a quadratic function of Pe.

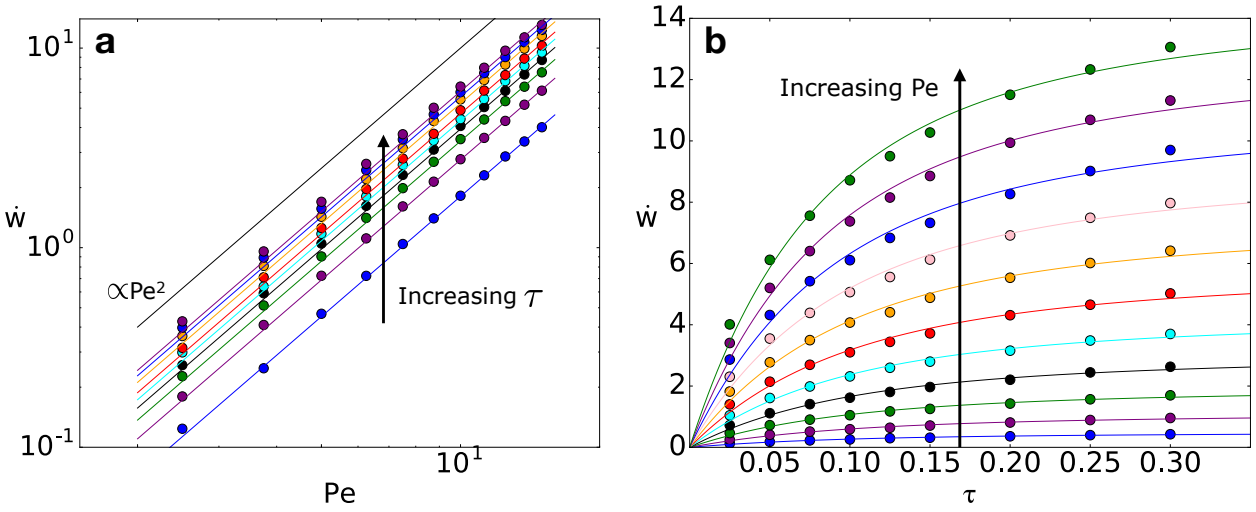

Figure 2.4: Rate of work done per particle as a function of (a) Pe and (b) τ by the driving forces in the full many-particle simulation, for values of Pe ranging from 2.5 to 15 and τ ranging from 0.025 to 0.3. Lines are fits to Eq. 2.10. Colors of points and lines serve only to allow easier differentiation between them. The parameter τ_G was fit separately to each line; there is a 5% variation in its value between fits. Error bars are smaller than the points.

The scaling of $\langle \dot{w} \rangle$ with τ can be similarly inferred by assuming that collision events are exponentially decorrelated with a characteristic time scale. Specifically, for values of τ much larger than the decorrelation time for fluctuations in the system, we simply anticipate that the work performed per cycle grows linearly with τ. For values of τ much smaller than the correlation time, the work done per cycle can be a nonlinear function of τ.

These scaling trends can be combined into an expression for $\langle \dot{w} \rangle$ in terms of Pe and τ.

$$\langle \dot{w} \rangle \propto \mathrm{Pe}^2 \left[1 - \frac{\tau_G}{\tau} \left[1 - e^{-\tau/\tau_G} \right] \right]. \tag{2.10}$$

The scaling of the work performed in Eq. 2.10 with Pe and τ follows the expected trends outlined above, with $\gamma_G/K_G \equiv \tau_G$ acting as a correlation time. In Fig. 2.4, we show that $\langle \dot{w} \rangle$ in the atomistic simulations does indeed scale as predicted in Eq. 2.10, with τ_G as a fitting parameter. We checked that the scaling also holds for different driving protocols, including cases where the particles are not phase locked or have random phases, and in systems with unequal number fractions of driven and undriven particles.

2.3.3.1 Expression for the effective spring constant K_G

We posited Eq. 2.8, but we note that the constants therein are formally related to properties of the system. For instance, using the Gaussian number density approximation, we can show how the effective spring constant K_G is a function of the two-point correlation functions and particle potentials. We begin by writing down a Hamiltonian appropriate for Gaussian density fluctuations in a liquid [21]:

$$\beta H = \frac{\beta}{2} \int d\mathbf{r} \int d\mathbf{r}' \delta\rho(\mathbf{r}) \chi^{-1}(\mathbf{r}, \mathbf{r}') \delta\rho(\mathbf{r}'). \tag{2.11}$$

χ^{-1} is the inverse of the variance, given by

$$\chi(|\mathbf{r} - \mathbf{r}'|) = \left\langle \delta\rho(\mathbf{r}) \delta\rho(\mathbf{r}') \right\rangle = \bar{\rho}\delta(\mathbf{r} - \mathbf{r}') + \bar{\rho}^2[g(|\mathbf{r} - \mathbf{r}'|) - 1], \tag{2.12}$$

where $g(r)$ is the pair correlation function and $\bar{\rho}$ is the density of the fluid. We approximate the inverse as follows [140, 21]:

$$\int \int \chi^{-1} \approx \frac{1}{\int \int \chi}\,. \tag{2.13}$$

To do so, we need to compute

$$\int d\mathbf{r} \int d\mathbf{r}' \chi(|\mathbf{r} - \mathbf{r}'|) = \int d\mathbf{r} \int d\mathbf{r}' (\bar{\rho}\delta(\mathbf{r} - \mathbf{r}') + \bar{\rho}^2[g(|\mathbf{r} - \mathbf{r}'|) - 1]). \tag{2.14}$$

The first term is

$$\int d\mathbf{r} \int d\mathbf{r}' \bar{\rho}\delta(\mathbf{r} - \mathbf{r}') = \int d\mathbf{r} \bar{\rho} = V\bar{\rho}, \tag{2.15}$$

where V is the system volume. To find the second term, we first perform a change of variable. The correlation depends only on the magnitude $|\mathbf{r}-\mathbf{r}'|$. Let $\mathbf{r}''=\mathbf{r}-\mathbf{r}'$, then:

$$\int d\mathbf{r}\int d\mathbf{r}'\bar{\rho}^2[g(|\mathbf{r}-\mathbf{r}'|)-1]=\int d\mathbf{r}'\int d\mathbf{r}''\bar{\rho}^2[g(r'')-1] \tag{2.16}$$

$$=V\rho\int d\mathbf{r}\bar{\rho}[g(r)-1]. \tag{2.17}$$

From the zero frequency limit of the Ornstein-Zernicke equation [82], we have that

$$1+\bar{\rho}\int d\mathbf{r}[g(r)-1]=\frac{1}{1-\bar{\rho}\int d\mathbf{r}c(r)}, \tag{2.18}$$

where $c(r)$ is the direct pair correlation function. Using this, Eq. 2.18 becomes:

$$\int d\mathbf{r}\int d\mathbf{r}'\chi(|\mathbf{r}-\mathbf{r}'|)=\frac{V\bar{\rho}}{1-\bar{\rho}\int d\mathbf{r}c(r)}\,. \tag{2.19}$$

We can now compute the inverse, $\int\int\chi^{-1}$, as follows:

$$\int\int\chi^{-1}=\frac{1-\bar{\rho}\int d\mathbf{r}c(r)}{V\bar{\rho}} \tag{2.20}$$

$$=\frac{1}{V\bar{\rho}}\int d\mathbf{r}\left[\delta(\mathbf{r}-\mathbf{r}')-\bar{\rho}c(r)\right] \tag{2.21}$$

$$=\int d\mathbf{r}\int d\mathbf{r}'\left[\frac{\delta(\mathbf{r}-\mathbf{r}')}{\bar{\rho}}-c(\mathbf{r},\mathbf{r}')\right]. \tag{2.22}$$

Substituting this back into the Hamiltonian and taking the functional derivative with respect to $\delta\rho(\mathbf{r})$ gives the effective force on $\delta\rho(\mathbf{r})$,

$$\frac{\delta H}{\delta(\delta\rho)}=\beta\left[\frac{\delta\rho(\mathbf{r})}{\bar{\rho}}-\int d\mathbf{r}'c(\mathbf{r},\mathbf{r}')\delta\rho(\mathbf{r}')\right]. \tag{2.23}$$

Assuming that $\delta\rho$ is not spatially dependent, this looks like a linear restoring force,

$$\frac{\delta H}{\beta\delta(\delta\rho)}\approx\delta\rho\left[\frac{1}{\bar{\rho}}-\int d\mathbf{r}c(r)\right]\equiv K_G\delta\rho=F_G, \tag{2.24}$$

where K_G is the effective spring constant of the Gaussian density fluctuations. Further simplification can be achieved by using the Percus-Yevick closure [21] to write down an approximate expression for $c(r)$,

$$K_G = \left[\frac{1}{\bar{\rho}} - \int d\mathbf{r} c(r)\right] = \left[\frac{1}{\bar{\rho}} + \int d\mathbf{r} g(r)(e^{\beta V(r)} - 1)\right], \tag{2.25}$$

where $V(r)$ denotes the pairwise potential between particles. The $1/\bar{\rho}$ term in Eq. 2.25 is an ideal gas contribution.

2.3.4 Force fluctuations

We now demonstrate how the work done on the system by the nonequilibrium forces affects the statistics of the force fluctuations that the particles experience. We begin by noting that according to Floquet theory [51], the nonequilibrium steady state induced by time-periodic driving forces is also time periodic. For the system to achieve such a time-periodic steady state, the increase in the internal energy of the system due to the total work, w, over each cycle has to be dissipated as heat. The average rate of heat emitted by the driven system (per particle) $\langle \dot{q} \rangle$ can be conveniently expressed in terms of the following stochastic integral, interpreted in the Stratonovich sense [125]:

$$\langle \dot{q} \rangle = -\frac{1}{N} \sum_{i=1}^{N} \frac{1}{\tau} \int \langle \mathbf{F}_{\mathrm{c,i}} \cdot \dot{\mathbf{r}}_{\mathrm{c,i}} \rangle, \tag{2.26}$$

where $\mathbf{F}_{\mathrm{c,i}}$ denotes the conservative force vector for particle i, $\dot{\mathbf{r}}_{\mathrm{c,i}}$ is the rate of displacement of particle i due only to the conservative and random forces (in contrast to $\dot{\mathbf{r}}_{\mathrm{d,i}}$), the sum is over all of the particles in the system, and τ is the period of the driving force. $\langle \dot{q} \rangle$ should equal the negative of the average rate at which work is performed on the system, $-\langle \dot{w} \rangle$, given by Eq. 2.7.

Indeed, by adding together Eqs. 2.7 and 2.26, we obtain an energy balance expression,

$$\frac{1}{\tau}\int\left\langle\frac{dU}{dt}\right\rangle=-\frac{1}{N}\sum_{i=1}^{N}\frac{1}{\tau}\int\langle\mathbf{F}_{\mathrm{c,i}}\cdot\dot{\mathbf{r}}_i\rangle=\langle\dot{q}\rangle+\langle\dot{w}\rangle=0, \tag{2.27}$$

where $\dot{\mathbf{r}}_{\mathrm{i}}$ is the total rate of change of the position vector of particle i due to all forces (defined in Eq. 2.1) and U is the internal energy of the system. Expanding this energy balance equation, we find that $\langle\dot{w}\rangle$ can be expressed in terms of the statistics of force fluctuations as

$$\langle\dot{w}\rangle\propto\langle\mathbf{F}^2\rangle-\langle\mathbf{F}^2\rangle_0, \tag{2.28}$$

where

$$\langle\mathbf{F}^2\rangle=\frac{1}{N}\sum_{i=1}^{N}\langle\mathbf{F}_{\mathrm{c,i}}^2\rangle \tag{2.29}$$

and

$$\langle\mathbf{F}^2\rangle_0=-\frac{1}{N}\sum_{i=1}^{N}\lim_{t\to0}\langle\mathbf{F}_{\mathrm{c,i}}(t)\cdot\eta_i(0)\rangle. \tag{2.30}$$

This equation does not depend on which convention (Itô or Stratonovich) is used to interpret the stochastic integral. $\left\langle\mathbf{F}^2\right\rangle_0$ captures the response of the nonequilibrium liquid following a random perturbation, while $\left\langle\mathbf{F}^2\right\rangle$ describes the force fluctuations on a tagged particle in its nonequilibrium steady state. In equilibrium, the two terms in Eq. 2.28 are equal as a consequence of fluctuation-dissipation theorem, as demonstrated in Appendix A1.1. Out of equilibrium, the work performed is positive and the relation between fluctuations and response breaks down. In this case, the difference between fluctuations and response is predicted exactly by flux of heat, or alternately, the rate at which work is performed, as illustrated in Eq. 2.28. We note that this expression is completely insensitive to the choice of nonconservative driving forces in Eq. 2.1. We also note that Eq. 2.28 is an instantiation of

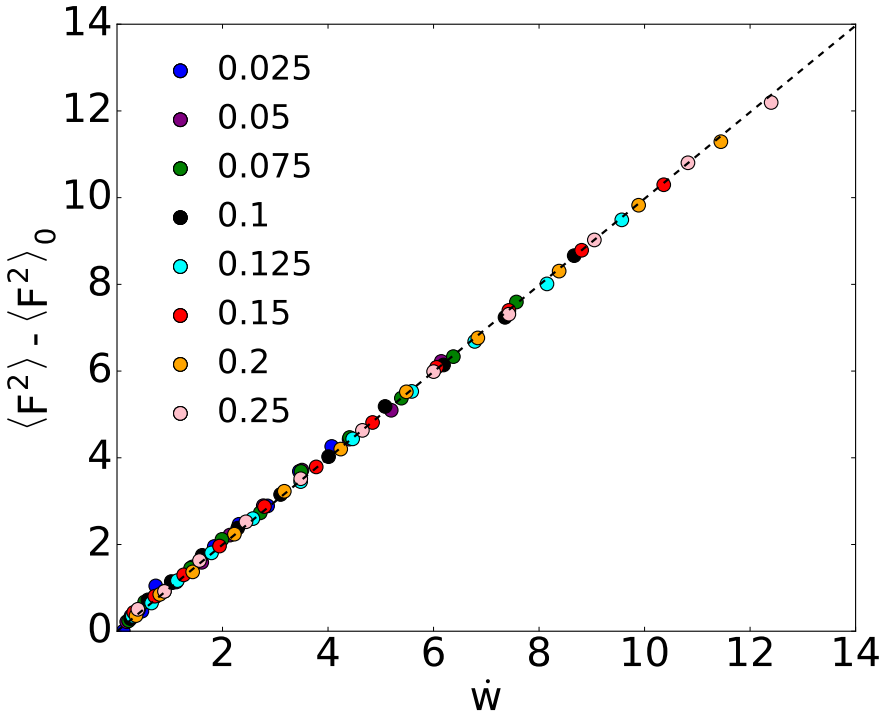

Figure 2.5: Deviation from fluctuation-dissipation theorem as a function of the rate of work done per particle. Colors indicate values of τ. The data collapse onto the line predicted by Eq. 2.28. Error bars are smaller than the points.

the Harada-Sasa relation [52, 53]. Here, we have obtained it for our nonequilibrium system following simple thermodynamic arguments.

We find numerically that the work performed in the many-particle system is indeed related to the breakdown of the equilibrium relation between fluctuations and response (Fig. 2.5). We verified Eq. 2.28 for a wide range of amplitudes and time periods of the driving force in the homogeneous part of the phase diagram. We also verified that this result holds for driving forces in which the particles are not phase locked or have random phases and in systems with unequal number fractions of driven and undriven particles. The relation also holds when applied separately to driven and undriven particles in all of these cases—in other words, the work performed on average due to the driven particles predicts the change in the force fluctuations of the undriven particles. In the following section, we study the implications of this result for the diffusion constant of the nonequilibrium system.

2.3.5 Diffusion

2.3.5.1 Diffusion increases with driving in simulations

In Brownian dynamics, the diffusion can be written in terms of force autocorrelation functions as follows:

$$D - D_0 = \frac{1}{d}\int_0^\infty \left[\left\langle \frac{\mathbf{F}(0)\cdot\mathbf{F}(t)}{\gamma^2}\right\rangle + \left\langle \frac{\boldsymbol{\eta}(0)\cdot\mathbf{F}(t)}{\gamma}\right\rangle\right] dt\,, \tag{2.31}$$

where d denotes the dimensionality of the system. It is reasonable to expect that the change in the force correlations that accompanies a breakdown of the fluctuation-dissipation relation, Eq. 2.28, affects the diffusion coefficient of the driven liquid.

To check this expectation, we measured the diffusion in simulations. Square simulation boxes of size $200r_0 \times 200r_0$ with periodic boundary conditions (PBC) were filled with 18,000 particles. Trajectories were run for at least $1{,}000\tau$ with a timestep of $\Delta t = 10^{-5}t_0$. The mean squared displacement (MSD) $\left\langle \mathbf{x}^2(t)\right\rangle$ of each particle in the simulations was measured at intervals of τ, so that there was no net displacement due to the driving forces. The diffusion coefficient was extracted by fitting the linear part of the MSD as a function of time according to $\left\langle \mathbf{x}^2(t)\right\rangle = 4Dt$.

We confirmed that the diffusion constant gets renormalized due to the driving forces and increases with the amplitude of the driving force after a transient region. In Fig. 2.6 we show that the renormalization of the diffusion constant is very well described by the functional form

$$D - D_{eq} = -a(\tau)\mathrm{Pe} + b(\tau)\mathrm{Pe}^2, \tag{2.32}$$

where D_{eq} is the density-dependent equilibrium diffusion coefficient of particles in the system (not to be confused with D_0, which is the diffusion of a single particle). Understanding the basis for the renormalization of D due to the nonconservative forces is important [16, 50]—as we will show, in the present context it can help explain how the energy input due to the nonconservative forces can drive phase separation.

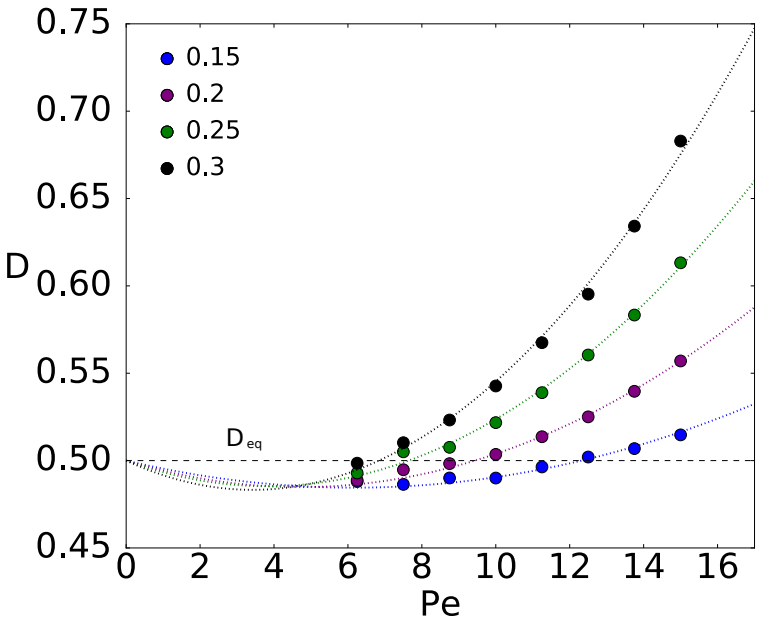

Figure 2.6: Scaling of the diffusion coefficient of a tagged particle in the liquid, D, with the amplitude of the driving force, Pe. The fit is to Eq 2.32. The intersection of the fits with the dotted line indicating D_{eq} shifts to the left with increasing τ, indicating that as τ increases, D is a quadratic function of Pe over a larger range. Colors indicate values of τ. Error bars are smaller than the points.

2.3.5.2 A minimal model predicts scaling of diffusion with Pe

In order to qualitatively understand the observed dependence of D on the nonconservative forces, we consider a minimal model of a tracer particle diffusing in a fluid according to the equation of motion

$$\dot{\mathbf{r}} = h\tilde{\mathbf{F}}(\mathbf{r}) + \tilde{\boldsymbol{\eta}}(t), \tag{2.33}$$

where $\tilde{\mathbf{F}}(\mathbf{r})$ is a spatially dependent force that can be designed to model the forces acting on a tagged particle in the liquid, h is a parameter that tunes the coupling between the fluid and the tracer particle, and $\tilde{\boldsymbol{\eta}}(t)$ is a Gaussian δ-correlated white noise. In order to ensure no net drift, we constrain $\int \tilde{\mathbf{F}}(\mathbf{r})d\mathbf{r} = 0$. We imagine sampling over many realizations of the force $\tilde{\mathbf{F}}(\mathbf{r})$ from a distribution in order to model the forces exerted by the fluid on a tracer particle. In the liquid considered in the previous sections, the statistics of force fluctuations on a tagged particle satisfy $\langle \mathbf{F}^2 \rangle = \langle \mathbf{F}^2 \rangle_0$ when the system is in equilibrium.

Equilibrium dynamics in Eq. 2.33 are achieved whenever $\tilde{\mathbf{F}}(\mathbf{r})$ can be expressed as a gradient of a potential, $\tilde{\mathbf{F}}(\mathbf{r}) = -\nabla\tilde{U}(\mathbf{r})$. In such cases, it can be demonstrated that the equivalent relation $\langle\tilde{\mathbf{F}}^2\rangle = \langle\tilde{\mathbf{F}}^2\rangle_0$ holds, where the averages $\langle\dots\rangle$ are taken both over the statistics of the random noise $\tilde{\boldsymbol{\eta}}(t)$ and over many realizations of the force. The system can be driven out of equilibrium by ensuring that the force in Eq. 2.33 has a nonconservative component, $\tilde{\mathbf{F}}(\mathbf{r}) = \tilde{\mathbf{F}}_{\mathrm{c}}(\mathbf{r}) + \mathrm{Pe}\tilde{\mathbf{F}}_{\mathrm{d}}(\mathbf{r})$, where $\tilde{\mathbf{F}}_{\mathrm{c}}(\mathbf{r}) = -\nabla\tilde{U}(\mathbf{r})$ and $\tilde{\mathbf{F}}_{\mathrm{d}}(\mathbf{r}) = \nabla\times\tilde{\mathbf{A}}(\mathbf{r})$. Like in the previous sections, Pe tunes the magnitude of the nonconservative force.

A rough qualitative mapping between the forces in the minimal model and the forces in the atomistic liquid can be obtained using the following reasoning. The nonequilibrium driving in the atomistic liquid alters the pair correlation function between a driven and an undriven particle in two ways. First, the scaling of $\langle w\rangle$ with Pe^2 reveals that due to the driving forces, the pair correlation function develops an anisotropic, time-dependent component that is also proportional to Pe. The nonconservative force introduced in the minimal model, $\mathrm{Pe}\tilde{\mathbf{F}}_{\mathrm{d}}$, is meant to qualitatively simulate the effect of the anisotropic component of the atomistic pair correlation function. Second, the isotropic component of the pair correlation function can also be affected by the driving forces. The potential $\tilde{U}$ in the minimal model is meant to simulate the effects of the isotropic component of the steady-state pair correlation function.

In the presence of the nonconservative forces in the minimal model, as in the many-particle driven liquid, a breakdown of the fluctuation-dissipation relation is predicted by the total amount of entropy dissipated by the system [53]. Using a perturbation theory [33, 41], we can show (Appendix A1.2) that to $O(h^2)$,

$$\langle\dot{\sigma}\rangle = \langle\tilde{\mathbf{F}}^2\rangle - \langle\tilde{\mathbf{F}}^2\rangle_0 = \frac{\mathrm{Pe}^2h^2}{V}\int\langle\tilde{\mathbf{F}}_{\mathrm{d}}(\mathbf{q})\cdot\tilde{\mathbf{F}}_{\mathrm{d}}(-\mathbf{q})\rangle d\mathbf{q}, \tag{2.34}$$

where $\langle\dot{\sigma}\rangle$ denotes the average rate of entropy dissipation, analogous to $\langle\dot{w}\rangle$ in the many-body liquid. On the right-hand side, $\mathbf{q}$ is the Fourier-transformed spatial variable and $\tilde{f}$ indicates

the Fourier transform of a function f.

For this minimal model, Tociu (Appendix A1.2) also obtained an expression for the diffusion constant in Eq. 2.33 that is to quadratic order in the parameters h and hPe,

$$D - D_0 = \alpha \frac{h^2}{V} \left(\mathrm{Pe}^2 \int \frac{\langle \tilde{\mathbf{F}}_d(\mathbf{q}) \cdot \tilde{\mathbf{F}}_d(-\mathbf{q}) \rangle}{|\mathbf{q}|^2} d\mathbf{q} - \int \langle \tilde{U}^2(\mathbf{r}) \rangle d\mathbf{r} \right), \tag{2.35}$$

where $\alpha = D_0/(d(k_B T)^2)$, d is the dimension, and we set $\langle \tilde{U} \rangle = 0$ without loss of generality so that $\langle \tilde{U}^2 \rangle$ is simply the variance of energy fluctuations.

To test our expression for the diffusion, we simulated a particle in a 2D periodic force landscape with a nonconservative component. The conservative force felt by the particle is $\mathbf{F}_c = -h\cos(x)\vec{e}_x - h\cos(y)\vec{e}_y$, and the nonconservative force is $\mathbf{F}_d = h\mathrm{Pe}\cos(y)\vec{e}_x - h\mathrm{Pe}\cos(x)\vec{e}_y$. We estimated D_{eq} in such a system by running five simulations with $\mathrm{Pe} = 0$ and averaging the resulting diffusion constants. Then we varied Pe between 0.2 and 0.45 and computed the diffusion constant and the error in each case by averaging over five simulations. Here, we report how the deviation of the diffusion constant from D_{eq} in our simulations compares to the expected correction due to Pe, which is $h^2\mathrm{Pe}^2/2$ (Fig. 2.7). We see a clear quadratic increase in diffusion with Pe and reasonable quantitative agreement.

We note that in these simulations, we had to use a value of h that is on the same order of magnitude as Pe. Running the simulations at a small value of h yields very small corrections to the bare diffusion that are hard to resolve due to errors. Our perturbation theory is therefore not expected to hold perfectly, as there will be higher order terms that scale like $h^3\mathrm{Pe}$ that are important when h is large but that we do not include in our perturbation theory (see Section A1.2.2). Despite these shortcomings, we see reasonable agreement at $h = 0.45$ and small deviations at $h = 0.5$, suggesting the quadratic term is the major contribution.

In instances where the spectrum of force fluctuations is strongly peaked at a particular wave vector $\mathbf{q}^*$, the diffusion constant can be simply related to the average entropy dissipation

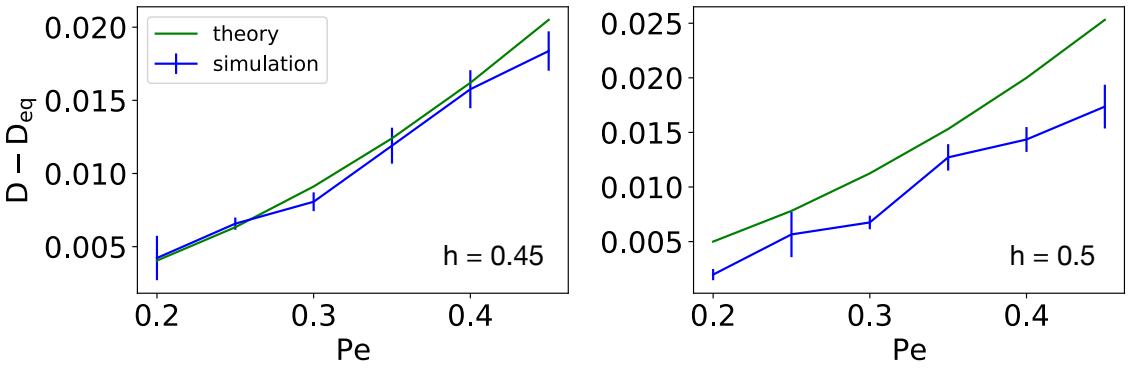

Figure 2.7: The correction to the diffusion constant due to the nonconservative force as a function of Pe for a single particle in a periodic force landscape. D_{eq} is the average diffusion constant for the system with Pe = 0. Error bars represent ± one standard deviation over 5 simulations. The data points are reasonably within error bars for $h = 0.45$ (left), while there is some systematic deviation at $h = 0.5$ (right).

rate as follows:

$$D - D_0 = \alpha \frac{\langle \dot{\sigma} \rangle}{|\mathbf{q}^*|^2} - \alpha h^2 \langle \tilde{U}^2 \rangle. \tag{2.36}$$

The dynamics of our driven liquid, specified by Eq. 2.1, are substantially more complicated than the minimal model considered. Nonetheless, the expressions in Eq. 2.35 and 2.36 provide useful insight. By using the variance $\langle \tilde{U}^2 \rangle$ as a measure of the microscopic environment around a tagged particle in the many-body driven liquid, and by associating the average dissipation rate $\langle \dot{\sigma} \rangle$ with the rate of work performed $\langle \dot{w} \rangle$ in the many-body liquid, Eq. 2.36 demonstrates how the nonconservative forces can modify the diffusion properties of a particle in the fluid. In particular, the minimal model predicts that the diffusion constant can increase as Pe^2 due to the energy dissipation from nonconservative forces.

2.3.6 Phase separation

Finally, we show that the increase of the diffusion constant due to the nonconservative forces renders the diffusion constant composition dependent. Specifically, unmixed regions, in which particles are either all driven or all undriven, effectively have equilibrium dynamics

and diffusion properties since the nonconservative forces do not induce any collisions in such regions. The diffusion constant in regions with mixed compositions can be enhanced (as described above) due to collisions induced by the nonconservative forces. As demonstrated in Appendix A2, such a composition-dependent diffusion constant can drive a transition from the low-drive mixed phase (region b in Fig. 2.2) to the phase-separated region (region c in Fig. 2.2) when

$$\lambda = \frac{b(\tau)\mathrm{Pe}^2}{D_{eq} + b(\tau)\mathrm{Pe}^2}\,, \tag{2.37}$$

where $b(\tau)$ is defined in Eq. 2.32 and λ is a constant defined in Appendix A2. Eq. 2.37 provides us with a lower bound on the value of Pe where phase separation first occurs.

In Fig. 2.8 we replot the phase diagram in Fig. 2.2e with lines representing our theoretical predictions for the location of the phase transition. We find that the phase transition curve is well described by $b(\tau)\mathrm{Pe}^2 = c \approx D_{\mathrm{eq}}$, where c is a constant, in accordance with Eq. 2.37 (green line in Fig. 2.8). Our numerical simulations show that $b(\tau)\mathrm{Pe}^2 \propto \langle w \rangle$ to a very good approximation (Fig. 2.9), and we also find that the shape of the phase transition curve is well described by $\langle w \rangle \propto c$ (purple line in Fig. 2.8). The results in Eqs. 2.35, 2.36, and 2.37 show how the increase in diffusion due to energy dissipation can control the phase properties of our nonequilibrium liquid. The phase transition properties of our driven liquid are effectively controlled by $\langle w \rangle$, the energy injected into it per cycle by the nonequilibrium driving forces.

2.3.7 Conclusions and future directions

From the rich physics of nonequilibrium materials, and in particular of active particles with rotating dynamics, it is clear that dissipation plays an important role in modifying the structural and dynamical properties of the steady states of these systems. Here, in the context of a class of systems with rotating dynamics, we have identified how the rate of work done by the external forces renormalizes force fluctuations. Using simplified descriptions of density fluctuations based on our observation of Gaussian density statistics, we were also able

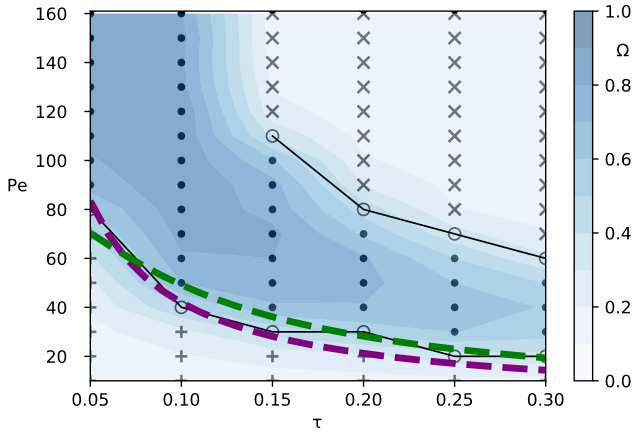

Figure 2.8: Phase diagram of the driven system at $\rho = 0.45$ shown in Fig. 2.2e with theoretical predictions for the location of the phase transition. The green line is proportional to $\mathrm{Pe}^2 b(\tau)$ ($b(\tau)$ is defined in Eq. 2.32). The purple line is proportional to the work done per cycle given by Eq. 2.10 using the fitting parameter τ_G extracted from the fits in Fig. 2.4.

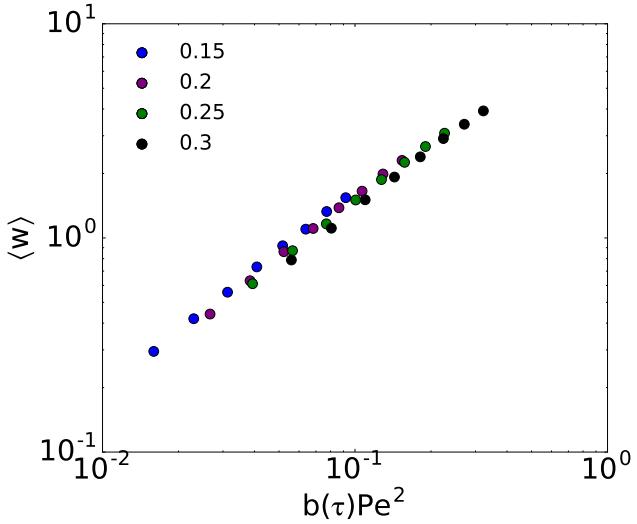

Figure 2.9: The last term in $D = D_{eq} - a(\tau)\mathrm{Pe} + b(\tau)\mathrm{Pe}^2$ is approximately proportional to the average amount of work done per cycle on the system. Colors indicate values of τ. Data points are for the same values of Pe and τ included in Fig. 2.6. Error bars are smaller than the points.

to model how the work performed in this many-body system depends on the nonequilibrium forces. Finally, using a minimal model, we explained the observed enhancement of the diffusion due to the nonequilibrium driving forces and proposed a relation between diffusion and dissipation. The renormalization of the diffusion due to dissipation also helped explain the observed dependence of the phase behavior on the magnitude of the driving force, Pe. Our results demonstrate how the material properties of nonequilibrium liquids can be tuned simply by violating time-reversal symmetry and controlling the amount of energy put into the system.

2.3.7.1 Tuning the structure of active and driven particle systems using dissipation

Current and future avenues of investigation involve building on the work in this chapter to establish and exploit the general nature of the relations between work, diffusion, and force fluctuations. Tociu et al. [137] have derived several relations between the dynamics and structure of driven liquids and the rate of work done. Specifically, without resorting to minimal models as we have done in this section, they derived an expression for the diffusion of a driven tracer as a function of the rate of work done within a Gaussian density approximation. They also obtained expressions that relate the two- and three-point correlation functions of driven liquids to the rate of work, which are valid beyond the Gaussian regime but in practice do require either a small fraction of driven tracers in a bath or a system of all active particles to be useful. Moreover, by explicitly showing the connection between systems of active particles with random internal driving and driven particles subject to a deterministic external driving force, they demonstrate that their relations are valid for both classes of systems. The authors then use these relations to motivate biasing functions that are used to generate ensembles of trajectories from equilibrium dynamics that exchange a nonzero amount of energy with the bath on average. These biased ensembles are shown to be equivalent to systems with a renormalized interparticle potential. They thus show analytically

and using simulations how injecting energy into a system of particles can be used to tune the effective interactions or any other observable that depends on the particle separation. In a related study, Nemoto et al. [91] showed that trajectories of a liquid of active Brownian disks biased toward low work always form clusters with dynamically arrested particles, while trajectories with high work exhibit flocking, with all particles aligned.

These results can also be used to solve the inverse problem, that is, to deduce the rate of work done based on static snapshots of an active matter system. Seif et al. [123] have demonstrated that a convolutional neural network (CNN) can deduce the arrow of time in a simple Ising model with time-dependent interaction energies. This is possible because the CNN is set up in such a way that it has access to the correlations in time and space that allow it to learn the path probabilities associated with average positive (forward in time) or negative (back in time) trajectories. Motivated by their work and by the results in this section and in Ref. 137 indicating that dissipation is in fact related to *static* structural properties of nonequilibrium systems, it is natural to ask whether the rate of work done can be learned by CNNs from static snapshots of nonequilibrium liquids. This is akin to asking whether a machine-learning algorithm can learn the empirical relations presented in this thesis, or the analytical results of Ref. 137—or potentially suggest other relations not yet discovered.

2.4 Interfaces

2.4.1 Introduction

In Section 2.3 we characterized and sought to explain theoretically how dissipation modifies the material properties of the liquid up to and near the phase transition. In this section we turn to the properties of the interfaces of the phase-separated liquid. Understanding how nonequilibrium driving modifies interfacial fluctuations in these cases is an important and open question. For instance, surface fluctuations play a central role in microscale ap-

plications [120], and understanding how to control them can contribute to our ability to exploit the engineering promise of nonequilibrium particle systems [149, 47, 48]. Here, we combine simulations with an analysis based on capillary wave theory (CWT) [9] to study the effect of the time-dependent forces on the interfacial properties of (1) the liquid with repulsive interactions studied in Section 2.3 and (2) a closely related liquid with attractive interactions between the driven particles and repulsive passive-passive and driven-passive interactions. To distinguish these systems, we will refer to the purely repulsive model as the Weeks-Chandler-Andersen (WCA) model, and to the new, partly attractive, model as the Lennard-Jones (LJ) model.

The main result of CWT predicts that the power spectrum of height fluctuations of an interface parallel to a prescribed horizontal axis satisfies $\langle |h(k)|^2 \rangle \propto 1/(\sigma k^2)$, where k denotes the wavevector, $h(k)$ denotes the Fourier transform of height fluctuations, and σ is the surface tension. This $1/k^2$ scaling—also known as capillary scaling—is found in systems ranging from the 2D Ising model to water [42, 127, 122]. CWT has also been used to study interfaces in nonequilibrium liquids and extract effective surface tensions [12, 100, 34, 102, 71].

It has been shown that phase separation in the WCA model belongs to the Ising universality class [49], which would lead us to expect capillary scaling of the interface modes [42]. Our first finding is that the time-dependent driving forces result in persistent particle currents along the interface of the WCA model. This brings the expectation of capillary scaling into question, because currents can affect the statistics of interface fluctuations. For instance, the currents present in a nonequilibrium Ising model with an applied electric field can cause the scaling to decrease to $1/k^{0.67}$ [73].

The fluctuations of active interfaces have recently been studied in systems of the MIPS type [12, 100, 71, 102], where there can be local tangential flows [102] but not system-spanning currents at the interface. In our system, and in others with rotational dynamics, we observe system-spanning currents qualitatively similar to those in the nonequilibrium driven Ising model [73]. The presence of these currents makes it important to examine the

full spectrum of capillary fluctuations. This examination will allow us to assess whether the system obeys capillary scaling and for what range of wavenumbers, to check the convergence of interface statistics, and to accurately measure the surface tension.

In the WCA model, we find that the scaling of interface fluctuations depends on the amplitude of the driving forces. For one amplitude that we studied, we find close to $1/k^2$ scaling, while for all others we find that $\langle |h(k)|^2 \rangle$ is inversely correlated with k but decreases less rapidly than predicted by CWT (Fig. 2.12). The effect of the driving forces on the stability of interfaces in the WCA model is nonmonotonic, because the forces cause the system to phase separate at low amplitudes but to become mixed again at large amplitudes [29]. Moreover, since the system is mixed at equilibrium, there is no reference value for the surface tension in the absence of driving. For these reasons, the WCA model is not ideal for systematically investigating the effect of driving forces on surface tension.

For this purpose, we introduce the LJ model, which is phase separated with a well-defined surface tension at equilibrium [100]. We find that the LJ model exhibits capillary fluctuations over a wide range of k even in the presence of driving. Over an order of magnitude in the driving forces, the effect of driving in the LJ model is a linear increase in σ. We discuss two ways that the driving forces can increase the force imbalance at the interface, thereby causing the observed increase in σ: first, by inducing a restoring force on the interface that is proportional to the curvature, and second, by changing the density of the liquid and gas phases of LJ particles. We show that both of these effects can contribute to the increase in the surface tension, but we leave a full account of the linear trend to future work.

2.4.2 Simulations

In this section we present simulations of two types of binary driven liquids, both with equations of motion given by Eq. 2.1. In the first, which was studied in Section 2.3, all particles have repulsive WCA interactions (Eq. 2.2) and they do not phase separate at equilibrium. In the second, there is an attractive Lennard-Jones potential (Eq. 2.3) between driven particles

and repulsive WCA interactions between undriven particles and driven/undriven particle pairs, causing phase separation and stable interfaces at equilibrium.

Molecular dynamics simulations of both models were performed using a custom Brownian dynamics integrator in LAMMPS [105]. Results reported here are for square simulation boxes with sides of length $L = 100r_0$ and number density $\rho = 0.5$, unless otherwise indicated, and periodic boundary conditions. We initiated the simulations by placing a slab $50r_0$ wide of driven particles in the middle of the box, spanning the system in the y-direction, so that there were two interfaces of length L along the y-direction.

For the WCA model, we chose parameters of the driving force in the phase-separated region of the phase diagram at $\rho = 0.5$ (Fig. 2.2e). At $\tau = 0.1$, the system phase separates into regions of driven and undriven particles when Pe ≈ 50 and becomes mixed again at large values of Pe (Pe > 150). To ensure that we were looking at systems that were in the bulk of the phase-separated region of the phase diagram, where interfaces would be stable, we chose to simulate interfaces at $\tau = 0.1, \rho = 0.5$, and Pe $= 60, 80, 100$ and 120. In Fig. 2.10 we show a snapshot of the slab geometry system with Pe $= 100$ in the steady state.

For the LJ model, the initial density of the slab of LJ particles, $\rho_{\mathrm{LJ}} = 0.85$, was chosen such that the particles would exhibit liquid-vapor coexistence in the absence of driving forces [128]. We then chose the density of passive WCA particles that would bring the total density of the system to 0.5. At equilibrium, this results in a liquid phase of LJ particles with a density of $\sim$0.72 in coexistence with a gas of driven and undriven particles (Fig. 2.10). We fixed $\tau = 0.1$ and varied Pe from 0 to 80. Examples of steady-state configurations of both models are shown in Fig. 2.10.

The expected relaxation time of the longest-wavelength interface mode was approximated as $\tau_r = L^2/D$, where D is the diffusion constant of the WCA model in the absence of driving [29]. In the WCA system, we ran each simulation for $10\tau_r$, discarded the first τ_r of the trajectory, and performed the CWT analysis on the remaining $9\tau_r$. In the LJ system, we ran each simulation for $20\tau_r$, discarded the first $10\tau_r$ of the trajectory, and performed the

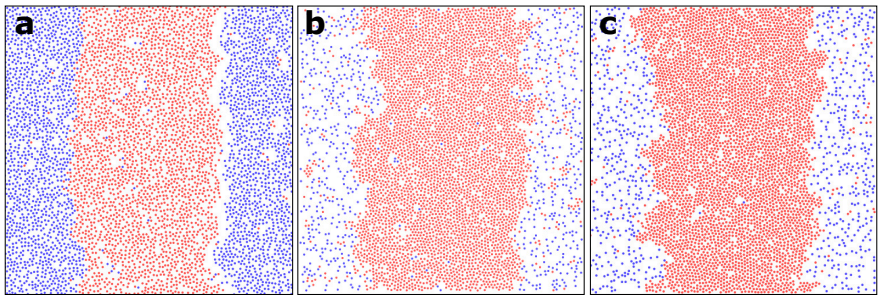

Figure 2.10: Two models of driven liquids exhibit stable, system-spanning interfaces. (a) Snapshot of the WCA model with Pe = 100. (b,c) Snapshots of the LJ model (b) at equilibrium and (c) with Pe = 40. These snapshots show the slab geometry used in our simulations. Active particles are colored red, and passive particles are colored blue. In the driven cases (a,c), a gap is visible at the right interface, which is particularly noticeable in the WCA system (a). The gap switches from one interface to the other with a period τ.

CWT analysis on the remaining $10\tau_r$. The center of mass was adjusted in the simulation at intervals of t_0 to compensate for drift, and as an extra precaution we also subtracted any center-of-mass motion before analyzing the trajectories. The box dimension perpendicular to the interfaces, L_x, was wide enough that the interfaces were stable along the y-direction, and that the width of the interfaces was unrestricted.

2.4.3 Interface characterization

2.4.3.1 Comments on phase separation

We begin by briefly recapitulating the mechanism of phase separation in the WCA model and how it relates to other studies of nonequilibrium interfaces. In Section 2.3 we found that the driving forces do work on the system by inducing collisions between particles. These collisions result in an increased diffusion coefficient that scales roughly proportionally to w, the amount of work done per period of driving, which in turn scales as Pe^2. Because the driven particles are always in phase, in a region with only driven particles or only undriven particles, the nonequilibrium forces do not induce any collisions. The work done and therefore

the diffusion coefficient thus depend on the local composition, and particles diffuse faster out of regions with mixed configurations than back into them. If the gradient of the diffusion with respect to composition is sufficiently high, this results in phase separation of driven and undriven particles.

This mechanism is similar to what has been proposed for systems that undergo laning (separation of two types of particles moving in opposite directions into lanes parallel to their velocity vectors) [67] and stripe formation (separation into stripes perpendicular to the direction of periodic forcing) [87, 106, 152]. In both cases, the differential mobility of the particles in the presence of the other particle type leads to separation. We note that this mechanism of phase separation depends on a high degree of synchronization between the displacement vectors of the driven particles of each type—in our case, the driving force on all driven particles is the same (Eq. 2.4), so that all the driven particles are in phase. If the directions of the driven particles were not correlated (for instance, if we were to assign random phases to each driven particle as we did to verify the generality of our results in Section 2.3), phase separation of the kind seen here would not occur. Instead, for sufficiently high Pe and slowly changing particle direction, we would expect motility-induced phase separation [75, 20]. Thus, whereas the results of Section 2.3 are generalizable to systems with out-of-phase driving forces such as active Brownian particles and active Ornstein-Uhlenbeck particles, the results of this section are specific to the model with in-phase forces.

Similarly to Refs. 87, 106, 152, and 145, in the WCA system there is a gap at one of the interfaces between the red and blue particles (Fig. 2.10a). The location of the gap switches periodically from one interface to the other. This is because due to their motion, the red (driven) particles effectively occupy a larger volume than the blue particles, such that the red particles are able to push the blue particles out of the way when the driving force pushes the two types of particles into one another. When the force changes directions, the red particles move en masse away from the blue particles, but diffusion is not fast enough for the blue particles to fill the space left by the retreating red particles, so a gap opens up.

2.4.3.2 Interface currents

Driven liquids with rotational dynamics can exhibit currents along boundaries and interfaces [93, 144]. Because of the slab geometry of the present system, any currents would have to be in the y-direction. To calculate the particle current, the simulation box was divided into slices of width r_0. For all particles in a given slice of the box at time $t + t_0$, the displacement $\Delta y = y(t + t_0) - y(t)$ was calculated. Although there is no velocity in Brownian equations of motion, we report $v_y = \Delta y/t_0$ as an analog of the velocity. The average v_y as a function of x was then calculated by averaging over all of the particles in the slice between x and $x + r_0$ over an interval $\tau_r = 20,000t_0$, after the system has reached a steady state. The average v_y in the bulk phase of driven particles was subtracted to obtain the interface v_y reported in Fig. 2.11.

In the WCA model, we find particle currents along the interface. In Fig. 2.11 we show that the direction of the flow is chiral, by which we mean that it moves in only one direction along the interface as determined by the direction of orbit of the driven particles, and that its maximum value is roughly linear in Pe. This feature has often been seen in chiral liquids [130, 93, 49, 154], and distinguishes interfaces in this and other chiral systems from ones previously studied in MIPS-type systems with WCA [12, 71, 102] or LJ [100] interactions, in which no flows exist in the steady state due to the random orientation of the active forces.

2.4.4 Capillary wave theory and analysis of height spectra

Our analysis of interfacial fluctuations is motivated by CWT [9]. For a flat, system-spanning interface of length L, CWT posits that fluctuations in the height of the interface are described by the effective Hamiltonian,

$$H = \frac{\sigma}{2} \int_L dx \left| \frac{dh}{dx} \right|^2 , \tag{2.38}$$

where $h(x)$ is the height of a 1D interface. Using Parseval's identity to take the Fourier transform yields a quadratic Hamiltonian in Fourier space, so we can apply the equipartition

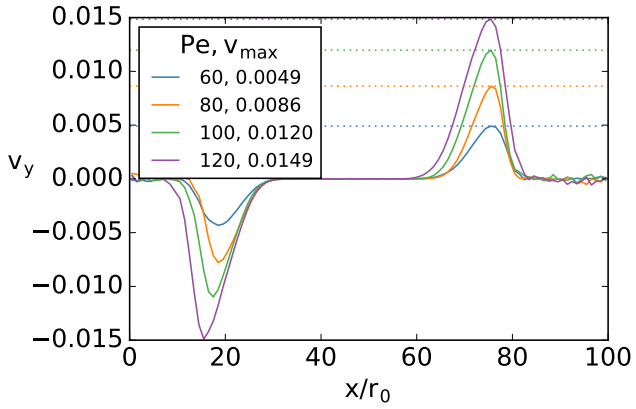

Figure 2.11: There is a net particle current along the interface in the driven WCA system. v_y quantifies the current along the interface in the y-direction. The maximum value of v_y scales roughly linearly with Pe. Dashed lines indicate the peak values of v_y for each simulation. Since the average position of the interface varies between simulations, the curves have been shifted in the x-direction to facilitate comparison.

theorem and obtain an expression for the average height fluctuations of the interface [9],

$$\langle |h(k)|^2 \rangle = \frac{k_B T}{L\sigma k^2}. \tag{2.39}$$

Here k is a scalar since we are considering straight, 1D interfaces in this work, but Eqs. 2.38 and 2.39 are easily generalized to higher dimensions [9]. In equilibrium, the σ appearing in Eq. 2.39 should match the surface tension obtained by any other means [116]. Out of equilibrium that may or may not be the case [12, 102]—nonetheless, if we find that the height fluctuations of the interface scale as $1/k^2$, we can use Eq. 2.39 to extract σ, which we may call an effective surface tension [12, 100, 34]. We note that in systems where capillary scaling is not obeyed, deviations from $1/k^2$ scaling have been connected to the violation of fluctuation-dissipation theorem—in other words, height fluctuations can still provide insight into how energy input affects correlations in the system [157].

To clearly define the location of the interface, we performed a coarse-graining of snapshots of the system at intervals of t_0 by dividing the simulation box up into a grid with cells $2r_0 \times 2r_0$ in dimension, yielding a lattice of dimensions $n \times n$ with $n = L/2$. We assigned a value of 1 to a grid site if it contained at least one driven particle, and a value of 0

otherwise. For the subsequent analysis, we only considered one of the two interfaces. We used an image processing algorithm on each frame to extract two contiguous clusters of grid sites, one with value 1 and the other with value 0, separated by an interface. The interface height at $j = y/2$ is the number of sites with value 1 in column j. To obtain $|h(k)|^2$, we took the discrete Fourier transform of $h'(j) = h(j) - \langle h(j) \rangle$. We averaged over all of the snapshots in an interval τ_r to obtain $\langle |h(k)|^2 \rangle$, and checked that the statistics did not change systematically between segments of τ_r. We took the segments to be statistically independent, and we averaged over them to get a second average $\langle \langle |h(k)|^2 \rangle \rangle$—this double average is the value reported in Figs. 2.12 and 2.13. The error was estimated as the standard deviation of $\langle |h(k)|^2 \rangle$ between the analyzed segments. The code used for the analysis is available upon request.

In the WCA system, where the scaling of $\langle |h(k)|^2 \rangle$ was not $1/k^2$, we extracted the scaling exponent by fitting the linear part of a log-log plot of $\langle |h(k)|^2 \rangle L$ versus $1/k^2$ (which part was linear was judged by eye from the data in Fig. 2.12). Where applicable, the surface tension was extracted by fitting $\langle |h(k)|^2 \rangle$ according to Eq. 2.39 over a range from $k_{\min}$ to $k_{\max}$, where $k_{\max}$ was defined as the largest value of k for which $\langle |h(k)|^2 \rangle$ was greater than the coarse-graining length of the system and $k_{\min}$ was defined as the smallest value of k for which $1/k^2$ was a good fit to $\langle |h(k)|^2 \rangle$, judged by eye from the data in Fig. 2.13.

2.4.4.1 Scaling of interface fluctuations and surface tension

Based on studies of driven lattice gases [72, 73], we might expect currents parallel to the interface in the WCA model to cause deviations of the interface height fluctuations from capillary scaling. Indeed, most of the parameters that we studied do not exhibit capillary scaling. However, for Pe = 120, the spectrum of interface fluctuations has an exponent close to -2, as expected from capillary scaling per Eq. 2.39, but only over roughly an order of magnitude of wavenumbers (Fig. 2.12). For this value of Pe, we calculated an effective surface tension of $\sigma/k_B T = 0.9$. For lower values of Pe, $\langle |h(k)|^2 \rangle$ decreases less rapidly with k than

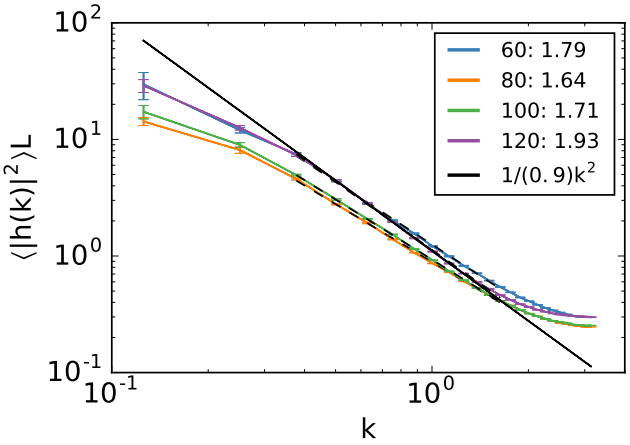

Figure 2.12: The WCA model exhibits capillary scaling for Pe = 120. Scaling of interface modes ($\langle|h(k)|^2\rangle$) multiplied by interface length (L) in the WCA model as a function of k, for interfaces of length $100r_0$ (solid colored lines). The legend indicates values of Pe and of the scaling exponent α, as in $\langle|h(k)|^2\rangle \propto k^{-\alpha}$, obtained by fitting over the region indicated by dashed black lines (directly on top of the colored lines), in the format (Pe : α). The fluctuations for Pe = 60 and 120 are larger than for Pe = 80 and 100. In this system, Pe = 60 is close to the point where the system first phase separates, while Pe = 120 is close to the point where the system becomes mixed again. Pe = 80 and 100 are further inside the bulk of the phase-separated region of the phase diagram. For Pe = 120, the scaling of fluctuations is close to the $1/k^2$ signature of capillary wave theory over roughly an order of magnitude in k, so for this case we also fit a line (solid black line) $\propto 1/k^2$ to calculate an effective surface tension $\sigma/k_BT = 0.9$. The error bars are negligibly small except for at $k < 0.3$.

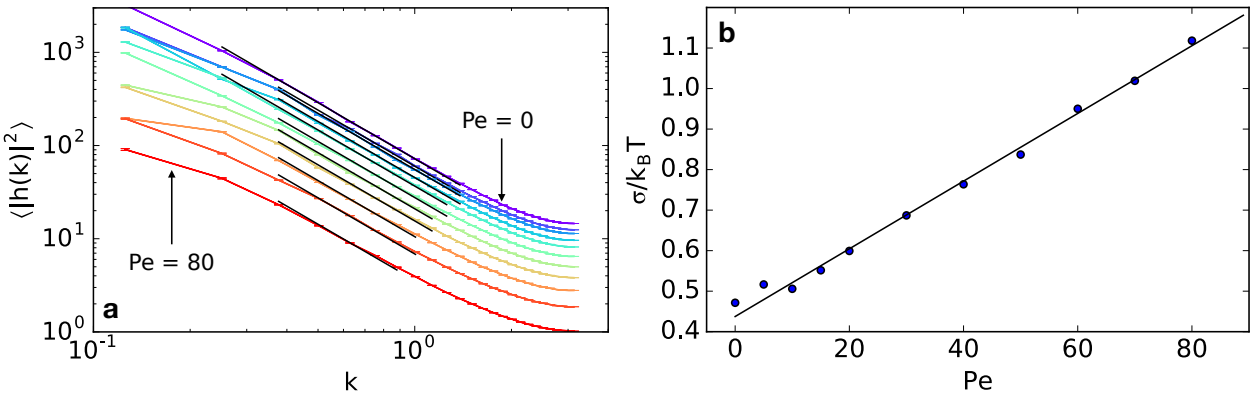

Figure 2.13: Driving increases the surface tension linearly and modifies the scaling of interface fluctuations of LJ particles. (a) Scaling of interface modes ($\langle|h(k)|^2\rangle$) in the LJ model as a function of k, for interfaces of length $100r_0$. The curves for Pe = 0–70 have been offset to make it easier to see that the range of k for which $\langle|h(k)|^2\rangle$ scales as $1/k^2$ is largest close to equilibrium and becomes smaller as Pe increases; the Pe = 80 curve is not offset to show that the magnitude of fluctuations is comparable to the WCA system. Black lines are $\propto 1/k^2$ and show the range of the fits used to extract σ; in this range, the error bars are very small. (b) Surface tension (measured from the fits of $\langle|h(k)|^2\rangle$) as a function of Pe, with a fit showing the linear correlation between σ and Pe.

predicted by CWT. The scaling exponents extracted from fits are shown in Fig. 2.12; however, we emphasize that these should not be interpreted as analytical exponents resulting from some underlying physics. We note that the system undergoes a reentrant mixing transition as the value of Pe is increased [29]. In particular, the point Pe = 120 is close to the reentrant transition. Due to this, we were unable to systematically probe the effects of increasing the driving force amplitude on the interfacial fluctuations.

At all values of Pe, fluctuations for the smallest ($k < 0.4$ in Fig. 2.12) and largest ($k > 2$) wavevectors do not follow the same trend as the rest of the data. At large wavevectors, $\langle|h(k)|^2\rangle$ flattens out as a result of the lower limit on fluctuations set by our coarse-graining of the system. To test whether the flattening at small wavevectors was a real feature or an artefact of the finite simulation time, we simulated a trajectory with Pe = 120 and $L = 200r_0$ for 8× longer than the $L = 100r_0$ simulations. There, $1/k^2$ scaling persists to longer wavelengths, suggesting that the falloff is indeed due to the simulation time.

The results in Fig. 2.12, as well as previous results on interfaces in active systems [100],

suggest that driving can change the effective surface tension and modify the statistics of interfaces in nonequilibrium liquids. Studying these effects in a systematic way is complicated in the WCA model by the fact that the driving has a nonmonotonic effect on the interface statistics over a relatively narrow range of values of Pe but a linear effect on the magnitude of the particle flow along the interface. In addition, since this system cannot phase separate in the absence of driving, there is no reference equilibrium interface to compare the driven interfaces to. To address this issue, we use the LJ model, which exhibits liquid-vapor coexistence at equilibrium. Interfaces in LJ liquids have been well studied and are known to exhibit capillary scaling [127, 116], so the LJ model provides a clear reference point that is lacking in the WCA model, and moreover, we can study the effect of driving forces starting well below $\mathrm{Pe} = 60$.

We first verified that the LJ model produced the expected behavior at equilibrium. We show in Fig. 2.13 that at $\mathrm{Pe} = 0$, the LJ system exhibits capillary fluctuations with a value of the surface tension that is in reasonable agreement with literature values [121]. The range of capillary scaling in k is again limited from above by the coarse-graining length and from below by the simulation time. We then measured the effect of driving the system with values of Pe ranging from 5 to 80. We find that the surface tension increases linearly over the whole range of Pe (Fig. 2.13). Based on both the results of Section 2.3 showing that driving can stabilize interfaces in this system and other studies of surface tension in driven systems [100], we expected an increase in surface tension. However, neither our results nor Ref. 100 indicates that the increase should be linear and persist over the entire range of Pe investigated here, which is an order of magnitude larger than that investigated in Ref. 100. In the following section, we present phenomenological arguments and simulation data that partially account for this observation.

2.4.5 Understanding nonequilibrium contributions to the surface tension

Despite our heuristic understanding (summarized at the beginning of Section 2.4.3) of how the driving forces in our model cause phase separation and therefore can create interfaces (in the WCA model) or stabilize them (in the LJ model) by increasing the surface tension, it is not clear why that increase should be linear in Pe. Surface tension arises due to an imbalance in the forces on particles near the interface. We now consider two ways that time-dependent driving forces of the kind studied here can magnify this force imbalance, and whether these magnifications can explain the observed increase in the surface tension (Fig. 2.13).

2.4.5.1 Work

First, we propose that the driving forces can cause the undriven WCA particles to exert a restoring force on regions of the interface with high curvature. To see why, consider a section of the interface like the one shown in Fig. 2.14. All LJ particles at the interface experience a force $\mathbf{F}_d \propto \mathrm{Pe}$ that pushes them into undriven WCA particles. In the linear response regime, WCA particles will push back with a conservative force also proportional to Pe [29]. A driven particle at the interface will therefore feel a downward force proportional to Pe and to the number of undriven particles in its neighborhood.[1] As we illustrate in Fig. 2.14, if the driven particle is at a point with negative curvature, it is surrounded by more undriven particles than if it were at a point with positive curvature. Thus, the excess downward force on the interface is proportional to the curvature: $\langle F_c \rangle_{int} \propto \mathrm{Pe}\nabla^2 h$. Combining this argument with the CWT Hamiltonian in Eq. 2.38, we can write down a phenomenological

1. Although the force exerted by the driven particle is not always pointed straight in to the undriven phase as illustrated in Fig. 2.14—it rotates according to Eq. 2.4—when the driven particles are moving away from the undriven particles they exert no force on the latter, since the driven-undriven particle interactions are purely repulsive. This results in the gaps that we observe at the interface in the WCA system. To a first approximation, we therefore assume that the most important contribution to $\mathbf{F}_d$ points outward normal to the interface and restoring force $\mathbf{F}_c$ points back down.

equation of motion for $h(x)$,

$$\frac{\delta h}{\delta t} = \frac{\sigma}{2}\nabla^2 h(x) + \mathrm{Pe}\nabla^2 h(x) + \eta(x,t), \tag{2.40}$$

where η is a white noise with statistics $\langle \eta(x,t) \rangle = 0$ and $\left\langle \eta(x,t)\eta(x',t') \right\rangle = 2k_B T\delta(x - x')\delta(t - t')$. We immediately see that this will result in an apparent surface tension $\propto$ Pe.

For this picture to correctly explain our observations, $\langle \mathbf{F}_c \rangle$ must scale with Pe, which implies that the work done on the system at the interface by the driving forces (defined in Eq. 2.7) should scale as Pe^2, since the work is proportional to $\mathbf{F}_c \cdot \mathbf{F}_d$. Motivated by our finding in Section 2.3 that work in a region of mixed driven and undriven particles scales as Pe^2, we hypothesized that this could also be the case at the interface. To check this hypothesis, we measured the work in simulations by summing $\mathbf{F}_{c,i} \cdot \mathbf{F}_d \Delta t/\gamma$ over all driven particles at each timestep. This quantity was summed over intervals of τ and divided by τ to get $\dot{w}$, which is shown as a function of Pe in Fig. 2.15. The averaged $\langle \dot{w} \rangle$ and errors shown in Fig. 2.15 are the average and standard deviation of $\dot{w}$ over 300 periods of τ, starting after the system has reached a steady state.

Work can only be done where there are driven and undriven particles in contact, so although we measured the work in the whole system, the small number of LJ particles in the WCA bulk and vice versa (Fig. 2.10) ensures that the interfacial region provides the important contribution to the total work. Contrary to our hypothesis, we show in Fig. 2.15 that in the LJ system the work is only quadratic in Pe for $\mathrm{Pe} < 15$ and then follows a linear trend up to $\mathrm{Pe} = 80$. This means that $\langle F_c \rangle_{int} \propto \mathrm{Pe}\nabla^2 h$ can only partially explain the linear scaling of σ with Pe.

2.4.5.2 Density profile

Another way that the driving forces can modify the force imbalance is by increasing the density of the LJ liquid phase and thus magnifying the imbalance in attractive forces. We

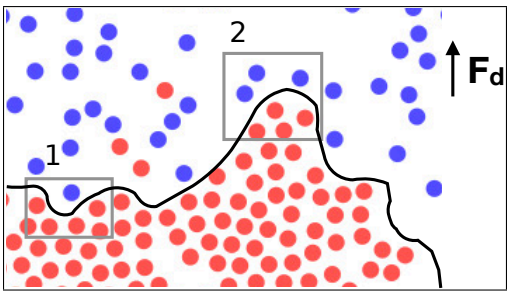

Figure 2.14: WCA particles exert a force proportional to $\mathrm{Pe}\nabla^2\mathbf{h}$ on LJ particles near the interface. At the moment of the snapshot, all red LJ particles are pushing up on the blue WCA particles with a force $\mathbf{F}_d \propto \mathrm{Pe}$. In the box labeled 1, where the curvature is positive, LJ particles experience an opposing conservative force from one WCA particle. In the box labeled 2, where the curvature is positive, LJ particles experience an opposing conservative force from three WCA particles. On average, this leads to a force on the interface $\propto \mathrm{Pe}\nabla^2 h$.

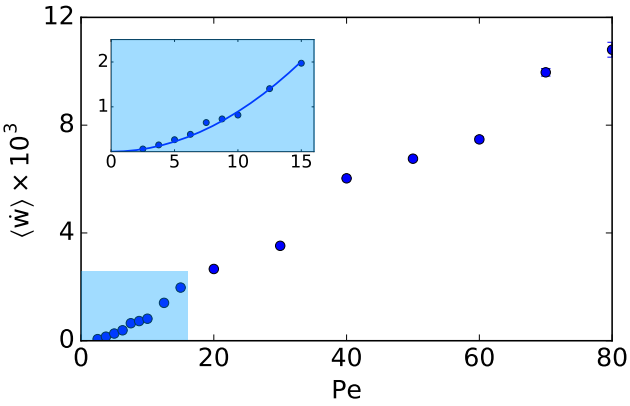

Figure 2.15: The rate of work done on the system by driving forces scales linearly with Pe for $\mathrm{Pe} > 15$. In the inset we show that for values of $\mathrm{Pe} \leq 15$ the work scales as Pe^2, in agreement with the results of Section 2.3. Error bars are smaller than the points except for at $\mathrm{Pe} = 80$.

measured the density of the driven LJ particles as a function of position to see if there was a significant change. The density profile of driven particles was measured by dividing the box into slices of width r_0 and calculating $\rho(x) = N/(L \times r_0)$ in each slice of the box at intervals of t_0, where N is the number of particles located in the slice between x and $x + r_0$. The average density profile was obtained by averaging $\rho(x)$ over an interval $\tau_r = 20,000 t_0$ in the steady state.

Indeed, as Pe is increased, the density of LJ particles in the liquid phase increases, and the density of LJ particles in the gas phase decreases. To quantify the change, we fit the density of the left interface to a hyperbolic tangent function of the form

$$\rho(x) = C \tanh(x - x_0) + b, \tag{2.41}$$

where C, b and x_0 are fitting parameters. When assuming this form for the density, the force imbalance on a particle located at the interface is proportional to C, so C should predict the increase in surface tension due to the change in density. In Fig. 2.16 we show that C increases roughly linearly with Pe. However, the change in C is only on the order of 15% and cannot explain the full increase in the surface tension that we observed.

The driving forces must therefore have further effects on the interface in addition to a force proportional to $\mathrm{Pe}\nabla^2 h$ and an increase in density; what these effects might be remains an open question. Importantly, in both of these arguments we ignored the time dependence of the driving forces. The time dependence is what causes currents at the interface, which are expected to affect fluctuations [73]. We therefore expect that it will be necessary to take into consideration time-dependent effects such as coupling between interface modes to account for our results.

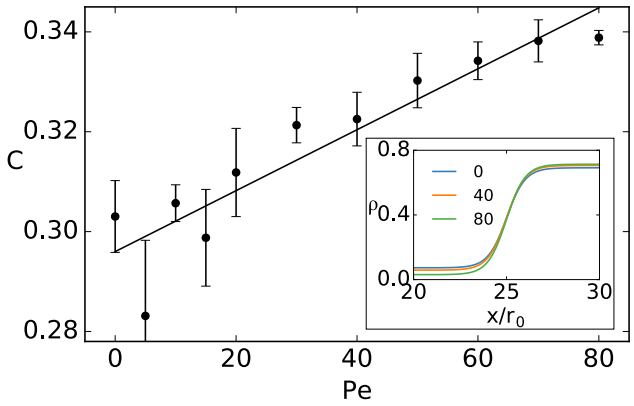

Figure 2.16: The density gradient near the interface scales linearly with Pe. The slope of the density near the interface, given by C as defined in Eq. 2.41, as a function of Pe. Error bars are the standard deviations of the values of C obtained from fitting density profiles of four independent segments of the simulation of length τ_r. Inset: An example of the fits of the density of LJ particles to Eq. 2.41 for Pe = 0, 40, and 80 shows the liquid density increasing and the gas density decreasing with increasing Pe.

2.4.6 Conclusions and future directions

In this simulation study, we presented results regarding the surface tension and the statistics of interfacial fluctuations in two closely related systems of driven particles: one where all particles have repulsive WCA interactions and half are driven, and a second where those driven particles have attractive LJ interactions. The WCA system is phase separated for Pe $\approx$ 50–150. Over this range the interfaces exhibit chiral particle currents parallel to the interface whose velocity is proportional to Pe. At one value of Pe near to the reentrant phase transition, height fluctuations of the interface exhibit the $1/k^2$ scaling that is a signature of capillary wave theory. For other values of Pe, the spectra of height fluctuations are inversely proportional to k but less steep than $1/k^2$. In the system with LJ interactions, stable interfaces with capillary scaling already exist at equilibrium. Upon driving, we found that capillary scaling persists and that surface tension increases linearly over two orders of magnitude in Pe, from small values in the linear response regime to well above the value of Pe required for phase separation in the WCA system.

2.4.6.1 Theories for active interfaces and chiral liquids

The driving force in our system can be reproduced in an experiment using rotating magnetic fields [49]. Our findings therefore suggest a way of controlling the surface tension of assemblies of particles from a distance, without the need to change any properties of the particles. We discussed two possible explanations for the excess force imbalance at the interface that causes the increase in the surface tension with Pe (a force proportional to the curvature of the interface induced by the driving forces, and the increased density gradient of the LJ particles), but neither captures the scaling or extent of the increase in surface tension that we observed. We also do not have an explanation for the way the scaling of $\langle |h(k)|^2 \rangle$ with k in these nonequilibrium systems is modified with respect to capillary wave scaling. However, recent work in the field of active chiral fluids and active interfaces provides several promising avenues to a more rigorous understanding of these phenomena.

First, in a recent paper, Soni and coworkers [130] developed a hydrodynamic theory for chiral fluids in an effort to understand experiments on a liquid of colloidal hematite cubes rotated by an external magnetic field. In addition to the usual hallmarks of surface tension such as droplet coalescence, this liquid exhibits properties not observed in equilibrium liquids, such as localized edge flows similar to those observed in our simulations and an instability that breaks a thin strip of the fluid into droplets. (Despite being visually similar, this is not a Rayleigh-Plateau instability, as the latter only appears in systems with three or more dimensions.) The key to understanding these features is recognizing that the breaking of time-reversal symmetry at the level of the chiral rotation (or, from our perspective, the energy dissipation required to achieve that breaking) means that new terms can show up in the hydrodynamic equations of the fluid that are disallowed by symmetry considerations at equilibrium. Although our simulated system is quite different at the macroscopic scale from the particle system in Ref. 130, it shares the conservation laws and symmetries of that system and the hydrodynamic theory should therefore be applicable. Reanalyzing our simulations with this theory in mind would allow us to rigorously measure the surface tension without

restricting ourselves to regimes where the power spectrum of interface height fluctuations appears to follow capillary wave theory. Specifically, we would first examine which terms in the chiral hydrodynamic equations are important given the details of our simulated system. We would then measure and Fourier transform the interface height as a function of time as well as space (in this work, we averaged over the time dimension, which may be the source of the lack of clear scaling of $\langle |h(k)|^2 \rangle$ in the WCA, and some LJ, simulations). Based on this measurement and others used by the authors of Ref. 130, we could estimate the parameters of the model, including the surface tension.

Further, the theory of active and growing interfaces has received much attention recently both from the perspective of minimal models of active matter [55, 12, 100, 28] and because of the importance of such interfaces in biology [18, 135]—for instance, fluctuations in cell membranes are affected by energy-consuming transport processes through the membrane and inside the cell, and the edge of a growing bacterial colony is an active interface. This growing body of work may shed light on our results and elucidate the connections between the interfaces in the system studied in this chapter and those in closely related active matter models as well as in more complex systems.

Chapter 3

Nonequilibrium driving and robustness in minimal models of biochemical oscillators

The material in this chapter is adapted with permission from the following publications:

[31] del Junco, C.; Vaikuntanathan, S. High chemical affinity increases the robustness of biochemical oscillations. *Phys. Rev. E*, 101:012410, **2020**. Copyright 2020 American Physical Society.

[32] del Junco, C.; Vaikuntanathan, S. Robust oscillations in multi-cyclic Markov state models of biochemical clocks. *J. Chem. Phys.*, 152(5):055101, **2020**.

3.1 Introduction

Many organisms use internal biochemical clocks to synchronize their metabolisms to day-night cycles, a tactic that confers fitness because it allows them to anticipate periodic environmental changes [151]. These clocks are implemented through a combination of chemical reactions, advection, and diffusion—stochastic processes that lead to a stochastic period of oscillations. In addition to this intrinsic noise, the heterogeneous environment inside a cell can increase the uncertainty in the clock's period [104]. How biological organisms can robustly maintain the time scales of their circadian rhythms in the presence of these fluctuations, maintaining consistent periods over different copies of the oscillator (e.g., in different cells) and over time, is hence a central question [7, 6, 5, 46, 86]. In this chapter we address it from the perspective of energy dissipation, asking what the energetic cost of accurate oscillations is.

Our question falls in a long lineage of work, since biological processes are generically noisy, yet typically require high accuracy and reproducibility. This is often achieved by energy-consuming mechanisms, as we know from research on energy cost/function trade-offs

in biology, beginning in the 1970s with Hopfield and Ninio's "kinetic proofreading" model for DNA replication [57, 94]. They showed independently that the expected error rate for DNA copying is alarmingly high if we assume it is an equilibrium process and used a simple model to demonstrate how the error rate can be dramatically reduced by driving the process out of equilibrium. Since then, a range of examples, such as the energetic costs of accurate sensing of ligand concentrations by a cell and other cellular "computations," have been studied [83, 70].

Biochemical clocks are a recent candidate for this area of study, largely thanks to the large body of experimental work that has thoroughly characterized the KaiABC clock, the circadian oscillator of the cyanobacterium *S. elongatus*. The oscillator can be reconstituted in vitro from a mixture of appropriate ratios of just three proteins (KaiA, B, and C) with ATP, which can sustain oscillations in the phosphorylation level of KaiC with a 24-hour period over many days even in constant light or dark conditions (Fig. 3.1a–b) [89, 138, 117]. On one hand, the period of the KaiC oscillator is very robust to changes in ambient conditions, so that it oscillates with an approximately 24-hour period over a wide range of temperatures, light levels, and fuel supply levels (in the form of ATP/ADP ratios) [63]. Yet these oscillators are also very flexible in the sense that they can be phase-entrained to periodic changes in these same variables [118, 155, 74]. It is likely that all of these remarkable properties require some amount of energy consumption [156, 39, 54]; here we focus only on the ability of a stochastic oscillator to maintain a constant period in the presence of fluctuating rates, without considering mechanisms such as entrainment to external cycles.

The models (depicted schematically in Fig. 3.1) that we use to derive our results are motivated by the fact that in a general sense oscillators undergo (noisy) limit cycles. The simplest model consists of N states connected in a ring that represents a projection of an oscillator's average limit cycle. For instance, in the KaiABC oscillator, each of these states would represent a vector of counts of the different phosphorylation states of a population of KaiC proteins [89, 117, 143, 79]. The system can hop between states with rates $k_i^{\pm}$, which

could represent (de)phosphorylation rates. The source of oscillations is that the forward reaction rates in the KaiABC cycle are larger than the reverse rates. The rates in our model reproduce this asymmetry, creating a nonequilibrium steady state with a net clockwise current [124]. The asymmetry cannot be due to a potential difference between the states, because in a closed circuit this would require an energy increase at some point in the cycle. Therefore, the system must consume energy to cycle. The chemical driving force responsible for the current can be quantified by the "affinity" of the network, $\mathcal{A} \equiv \log \prod_{i=1}^{N} k_i^+ / k_i^-$ [124]. In the case of KaiC, which is an ATPase, the affinity is provided by the highly exergonic hydrolysis of ATP [136]. If the system is initialized on a state i_0 in a network with a nonzero affinity, the probability associated with finding the system in any state will exhibit damped oscillations. The period of the oscillations reflects the average time taken by the system to traverse the ring and return to the state i_0. The damping in the oscillations is an unavoidable consequence of the stochastic nature of the transitions. The ratio $\mathcal{R}$ of the damping time to the oscillation time provides a figure of merit for the coherence of oscillations in the network [108, 19, 86, 19, 92], since it is proportional to the number of coherent oscillations that the network can complete before losing memory of its initial state. We refer to $\mathcal{R}$ interchangeably as the "number of coherent oscillations" or "coherence" throughout this chapter.

In principle, $\mathcal{R}$ depends on all the details of the rates $k_i^{\pm}$ in the network. However, in line with work showing that energy dissipation constrains the accuracy of biophysical processes [57, 10, 107, 70, 83, 88], it has been suggested that irrespective of these details the affinity constrains the coherence of biochemical oscillations [19, 6, 150, 92]. In particular, Barato and Seifert recently conjectured an upper bound on $\mathcal{R}$ as a function of the number of states N and the affinity $\mathcal{A}$ of the biochemical network [6]. The bound is saturated when the network is uniform; that is, when all of the counterclockwise (CCW) rates in the network are equal and all of the clockwise (CW) rates are equal. However, the structure of even simple models of biochemical oscillators constrains them to operate far from these

bounds [79], which raises two questions: First, what role does energy dissipation play in cases where it only weakly constrains the accuracy of oscillations? Second, which variables control the time scales of the oscillator in the presence of rate fluctuations? If the time scales depend sensitively on all of the rates in the network, then they will vary dramatically with any fluctuations in the rates. Conversely, if the time scales depend on only a small subset of the variables, then they will be robust to any fluctuations that do not affect this subset.

In this chapter, we probe these questions by obtaining analytical expressions for the time scales of Markov state models with nonuniform rates, for which calculating the period T and coherence $\mathcal{R}$ is an eigenvalue problem. In Section 3.2 we define these models and their dynamics. In Section 3.3 we derive an analytical expression for an eigenvalue of the transition rate matrices of models with a single cycle that gives the period T and number of coherent oscillations $\mathcal{R}$. In general, these quantities depend on the magnitudes and locations of all of the entries in the transition rate matrix, yet our results reveal that they depend only on the single-site distribution of the rates. While the result is formally exact in the limit that the $\exp(-\mathcal{A}/N) \to 0$, in practice our numerical results in Section 3.3.3 show that it works for surprisingly low values of the affinity. In Section 3.4 we extend our results to models with multiple cycles. By mapping cycles in these networks to edges in a single-cycle model, we show that $\mathcal{R}$ and T can also be insensitive to the location of these cycles—that is, dissipation can render the time scales of the networks robust to random fluctuations in the rates and connectivity of the model.

Despite the utility of the minimal models used here and elsewhere in understanding the thermodynamics of oscillating stochastic systems, it remains unclear to what extent these results are relevant to the much more complex networks underlying real circadian oscillators such as KaiC. We conclude the chapter by discussing a possible route to making the connection between the minimal, analytically tractable models used here and a more detailed computational model of the KaiC oscillator [79, 97] that is actually able to reproduce experimental results. Specifically, we introduce a nonequilibrium dimensional reduction al-

gorithm recently described in the literature called generalized Perron cluster-cluster analysis (G-PCCA) [113, 112] and discuss how we can apply it to simulations of KaiC in order to directly extract the reduced Markov state models that underlie them. In doing so we hope to eventually clarify the connection between (1) the large body of experimental and simulation work that has qualitatively and quantitatively described the phenomenology of the KaiC oscillator, including its compensation and plasticity, and (2) the understanding from statistical thermodynamics of the topological and energetic requirements for networks to display these phenomena.

3.2 Markov models of biochemical oscillators

In this chapter we consider Markov models such as the ones in Fig. 3.1d,f as simple models that capture the cycling and stochasticity of biochemical oscillators [6]. In these models, each vertex represents a collective state of the system. For instance, in the KaiABC oscillator, it could be a vector of the counts of KaiC monomers in each phosphorylation state and the concentrations of other species in solution (Fig. 3.1a,b) [117]. The rates along each of the edges represent the rates of elementary processes such as a phosphorylation event. We emphasize that this picture is thus not a representation of the underlying chemical reaction network, which must contain, at a minimum, a negative feedback loop, and may also have other motifs [95]. Rather, it is an emergent picture that captures the oscillations that can arise from such a network, and the feedback as well as the mass action kinetics are encoded in the rates along each edge, which depend on the collective state of the system represented by the connected vertices. It is not expected that a real oscillator will always follow the same path through its state space on each cycle. The single-cycle model in Fig. 3.1d is a caricature that captures the average limit cycle of the oscillator. The multi-cycle model in Fig. 3.1f is a caricature intended to reflect small fluctuations about this average path.

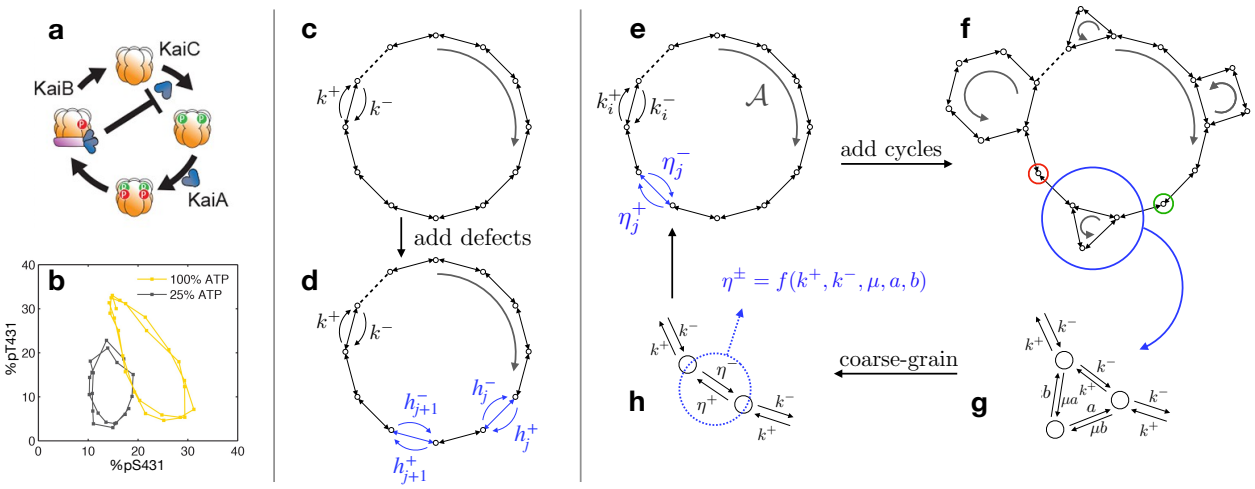

Figure 3.1: Markov models for biochemical oscillators studied in this chapter. (a) Schematic of the phosphorylation cycle of a single KaiC hexamer (reused with permission from Ref. 104). (b) Biochemical oscillators trace a limit cycle in a high-dimensional state space of chemical concentrations. In this example, a population of KaiC hexamers traces a limit cycle in the space of the fraction of monomers phosphorylated at each of two sites, S431 and T431 (reused with permission from Ref. 74). (c) We approximate these limit cycles by projecting them down onto a single cycle of states. Each node represents a state of the system. The system hops between states with rates $k^{\pm}$ and is driven out of equilibrium by an affinity $\mathcal{A}$. This creates a net clockwise current, resulting in damped oscillations in the probability of finding the system in a particular state. To develop our theory, we start with a uniform network where the network is fully translationally symmetric, for which the time scales are known. (d) In Section 3.3 we probe the dependence of the oscillation time scales on the rates of the network by adding "defect rates" $h_j^{\pm}$ to the uniform network and obtaining expressions for the coherence and period of oscillations in the disordered network. Our theory works in disordered networks where no two rates are equal. (e,f) In Section 3.4 we extend our results to networks where the main cycle is decorated with many small cycles. (g) We design these "decorations" so that the rates going into them are modulated by a small parameter μ that governs the probability that the system will enter the decoration. (h) To apply our theory to these multi-cycle networks, we map the multicyclic network onto a unicyclic network by matching moments of the first passage time distribution for a random walk beginning CCW from the decoration (green circle in panel (f)) and ending CW from it (red circle in panel (f)) onto a line of states with two unknown hopping rates. This procedure gives a set of effective hopping rates $\eta_i^{\pm}$. When each of the decorations in the network is coarse-grained in this manner, we obtain a single-cycle network whose period T and coherence $\mathcal{R}$ approximate those of the full, multi-cycle network. The effective hopping rates $\eta_i^{\pm}$ play the role of defect rates.

The dynamics of these models are governed by the master equation

$$\dot{\mathbf{P}}(\mathbf{t}) = \mathbf{W}\mathbf{P}(\mathbf{t}), \tag{3.1}$$

where $\mathbf{W}$ is the matrix of transition rates for hopping between states and $\mathbf{P}$ is the vector of the probabilities P_i of finding the system in a state i. We can define the correlation function $C_{11}(t)$ as the conditional probability of the system being in state 1 at time t given that it began in state 1 at time 0. The correlation function is given by the solution of the master equation

$$\begin{aligned} C_{11}(t) &\equiv [\exp(\mathbf{W}t)\mathbf{P}(0)]_1 && (3.2)\\ &= \sum_{j=0}^{N-1} P_j^{ss} e^{\phi_j t} && (3.3)\\ &= \sum_{j=0}^{N-1} P_j^{ss} e^{\mathrm{Re}[\phi_j]t}(\cos[\mathrm{Im}[\phi_j]t] + i\sin[\mathrm{Im}[\phi_j]t]), && (3.4) \end{aligned}$$

where ϕ_j are the N eigenvalues of the $N \times N$ matrix $\mathbf{W}$, P_j^{ss} is the steady-state ($t \to \infty$) probability of finding the system in state j, and $[...]_1$ is the first element of the vector. $C_{11}(t)$ will be a damped periodic function as illustrated in Fig. 3.2. The two quantities we wish to study are the period of the oscillator, which is the distance between subsequent peaks in $C_{11}(t)$, and the rate at which the oscillations are damped, given by the ratio of the time scale of the exponential decay to the period. From Eq. 3.4, we see that these quantities depend on the full spectrum of eigenvalues of the matrix. However, in this chapter we follow Ref. 6 in approximating the average period of oscillations T and the number of coherent oscillations $\mathcal{R}$ as

$$T = 2\pi/|\,\mathrm{Im}[\phi_1]| \qquad \text{and} \qquad \mathcal{R} = -|\,\mathrm{Im}[\phi_1]|/\,\mathrm{Re}[\phi_1], \tag{3.5}$$

where ϕ_1 is the eigenvalue of the transition rate matrix of the network that yields the largest

value of $\mathcal{R}$. We will drop the subscript for simplicity, so that in the following sections ϕ without a subscript denotes ϕ_1. A higher value of $\mathcal{R}$ corresponds to smaller fluctuations in the period. In Ref. 6 it was postulated that $\mathcal{R}$ is maximized in a uniform oscillator, that is, when all of the CW rates k_i^+ are equal to one another and related to the CCW rates k_i^- by $k^+ = \exp(\mathcal{A}/N)k^-$, as in the model depicted in Fig. 3.1c. However, since the rates along each edge of the network depend on the collective state of the system represented by the connected vertices, a network that sustains oscillations cannot be uniform [79]. Moreover, both the rates and, in the case of the multi-cyclic network depicted in Fig.3.1f, the locations and sizes of the small secondary cycles can fluctuate over time and between copies of the oscillator. Thus, although the value of $\mathcal{R}$ is one measure of the quality of timekeeping and therefore "robustness" in a biochemical clock, the definition of robustness that we consider in this paper is how predictable the period of oscillations T and the coherence $\mathcal{R}$ are with limited knowledge about the specific details of the arrangement of rates and decorations in the network, and by extension, how insensitive these quantities are to fluctuations in these details. In other words, rather than asking how dissipation can maximize the value of $\mathcal{R}$ in a single oscillator, we consider how dissipation can reduce the variance in both T and $\mathcal{R}$ within an ensemble of oscillators characterized by randomness in the rates and topology of the underlying network.

3.2.1 The largest nonzero eigenvalue captures the time scales of disordered oscillators

To see why a single eigenvalue ϕ is sufficient to approximate T and $\mathcal{R}$, we first consider a uniform network in which $k_i^+ = k^+ \forall i, k_i^- = k^- \forall i$. In that case, Eq. 3.3 simplifies to

$$C_{11}(t) = \frac{1}{N} \sum_{j=0}^{N-1} e^{\phi_j t}. \tag{3.6}$$

As illustrated in Fig. 3.2, the transition rate matrix $\mathbf{W}_0$ for this system is a circulant

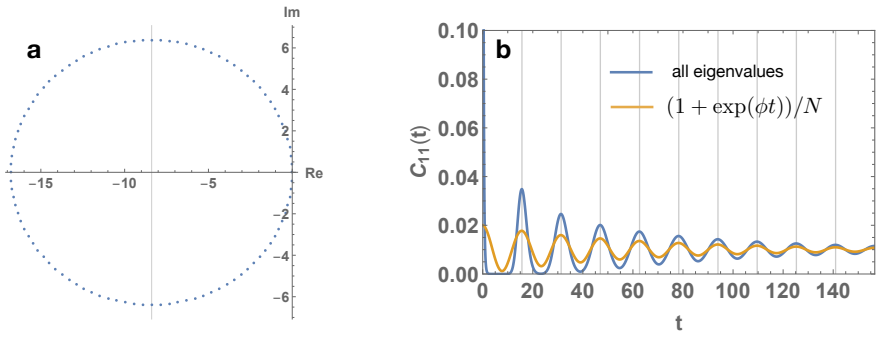

Figure 3.2: (a) Eigenvalues of a circulant matrix representing a network of size $N = 100$ with uniform rates $k^+ = e^2$ and $k^- = 1$. (b) The corresponding correlation function $C_{11}(t)$ (blue) and the contribution from only the zero eigenvalue and the dominant eigenvalue ϕ (yellow). Vertical grid lines are at intervals of $2\pi/\operatorname{Im}[\phi]$, showing that the period of a uniform system is very well approximated by ϕ.

matrix whose eigenvalues lie in an ellipse in the complex plane with semimajor axis $a = k^+ + k^-$ and semiminor axis $b = k^+ - k^-$ centered on the point $(-a, 0)$. When the affinity is large and $k^+/k^- \gg 1$, this effectively becomes a circle of radius $r = k^+$ centered at $(-r, 0)$.

The first eigenvalue is $\phi_0 = 0$, so the first term of the sum in Eq. 3.3 gives a constant contribution of $1/N$. The angle from the real axis to the jth eigenvalue ϕ_j is $2\pi j/N$. The imaginary part of ϕ_j is given by $r\sin(2\pi j/N)$, and the period of oscillations of the mth term in Eq. 3.4 is $T_j = 2\pi/(r\sin(2\pi j/N))$. The ratio of T_1 from the first nonzero eigenvalue to T_j from any subsequent eigenvalue is

$$\frac{T_j}{T_1} = \frac{\sin(2\pi/N)}{\sin(2\pi j/N)} \approx \frac{2\pi/N}{2\pi j/N} = \frac{1}{j} \tag{3.7}$$

for $N \gg j$. The total period of the oscillations is therefore always T_1. Since $\operatorname{Re}[\phi_1] < \operatorname{Re}[\phi_j]$ for all $j > 1$, the number of oscillations of the correlation function is given exactly by $|\operatorname{Im}[\phi_1]|/(-2\pi \operatorname{Re}[\phi_1]) = \mathcal{R}/2\pi$.

In the following sections, we will consider networks where the rates are not uniform. In that case, the eigenvalues will no longer lie on a perfect ellipse in the plane, and the arguments above will no longer hold exactly. T_j/T_1 may no longer be an integer, so that the total period of oscillations $T \neq T_1$, and moreover, the period of the oscillations at short times

$T(1)$ and the period of oscillations at long times $T(\tau)$, may not be the same. In Fig. 3.3 we show histograms of the relative difference $(T(1) - T_1)/T(1)$ for different realizations of matrices of size $N = 100$ with reverse rates all equal to 1, random forward rates h_i^+ chosen from a Gaussian distribution with mean $\mu = \exp(\mathcal{A}/N)$ and variance $\sigma^2 = 0.25\exp(\mathcal{A}/N)$, and uniform forward rates k^+ set to maintain a constant $\mathcal{A}$. We find that for small amounts of disorder and high affinity, the first eigenvalue still gives a good approximation of the period of the oscillator.

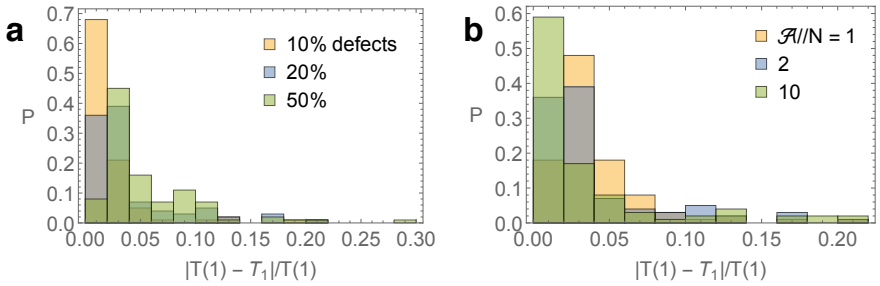

Figure 3.3: Histograms of the relative difference between the first period of oscillations of the correlation function $C_{11}(t)$ ($T(1)$) and the period of oscillations due to the first eigenvalue $T_1 = 2\pi/\,\mathrm{Im}[\phi]$. $T(1)$ is the location of the first peak of $C_{11}(t)$ obtained by exponentiating the full transition rate matrix. T_1 was calculated from the first eigenvalue, which was also obtained numerically. The data for each set of parameters were obtained from 100 randomly generated matrices. (a) At constant $\mathcal{A}/N = 2$, the agreement between $T(1)$ and T_1 gets worse as the percent of defects is increased from 10 to 50%. (b) With the percent of defects held constant at 20%, the agreement between $T(1)$ and T_1 improves with increasing $\mathcal{A}/N$.

3.3 Single-cycle oscillator models

3.3.1 Introduction

We begin by studying Markov models consisting of a single cycle of states, as depicted in Fig. 3.1c,d. In Section 3.3.2 we use a perturbation theory about a model with uniform rates to derive our main result: an analytical expression for the dominant eigenvalue ϕ of the transition rate matrices of models with arbitrary rates. In general, these quantities depend on the magnitudes and locations of all of the entries in the transition rate matrix, yet our result depends only on the single-site distribution of the rates. While the result is formally

exact only in the limit that the $\exp(-\mathcal{A}/N) \to 0$ (or when all of the rates are uniform), in practice our numerical results in Section 3.3.3 show that it works for surprisingly low values of the affinity. First, we demonstrate the success of the theory at predicting ϕ in networks with increasing numbers of rates not equal to the uniform value, which we call "defect rates" by analogy to the solid-state results that our analytical theory is inspired by. Second, we test the theory on networks where all of the rates are drawn from a random distribution. From a technical perspective, our results allow us to analytically compute values of the coherence and period in disordered regimes where $\mathcal{R}$ is significantly smaller than the upper bound. From a biological perspective, our results suggest that as well as minimizing inherent fluctuations arising from the stochasticity of the underlying processes [19, 6, 5, 46] a large energy budget has the additional, as-yet-unexplored advantage of reducing uncertainty in the presence of the additional level of disorder in reaction rates. We finish by summarizing and noting the connections between our results and the literature on random walks in random potentials and Lyapunov exponents of products of random matrices [36, 13, 35].

3.3.2 Perturbation theory

3.3.2.1 Eigenvalues of uniform networks

As in Ref. 6, we compute $\mathcal{R}$ from the ratio of the imaginary to real parts of the first nonzero eigenvalue (ϕ) of the transition rate matrix associated with the Markov state network. We approximate the period of oscillations by $T \approx 2\pi/|\operatorname{Im}[\phi]|$ and the correlation time by $\tau \approx -1/\operatorname{Re}[\phi]$ and $\mathcal{R} = |\operatorname{Im}[\phi]|/-\operatorname{Re}[\phi]$. Formally, T and τ depend on all the eigenvalues of the transition rate matrix, but the following arguments suggest that ϕ captures the important features of T and τ.

Reference 6 states that for a fixed affinity $\mathcal{A}$ and number of states N, $\mathcal{R}$ is bounded by

$$\mathcal{R} \leq \cot(\pi/N)\tanh[\mathcal{A}/(2N)] \equiv \mathcal{R}_0 \tag{3.8}$$

and that the bound is saturated in a uniform network, that is, when $k_i^+ = k^+ = \exp(\mathcal{A}/N)k^-$ and $k_i^- = k^-$ for all i. The transition rate matrix $\mathbf{W}^{(0)}$ for the uniform network is given by

$$\mathbf{W}_{ji}^{(0)} = k^+\delta_{i,j-1} + k^-\delta_{i,j+1} - (k^- + k^+)\delta_{i,j}. \tag{3.9}$$

$\mathbf{W}^{(0)}$ is a circulant matrix whose ith row is the top row shifted to the right by i columns [1]. Its eigenvalues are the discrete Fourier transform of the first row, giving $\phi^{(0)} = -(k^+ + k^-) + k^+e^{2\pi i/N} + k^-e^{-2\pi i/N}$, from which $\mathcal{R}_0$ is immediately recovered. We begin from this known result in order to find how the addition of disorder changes ϕ. We perturb the uniform network by adding some number $m \leq N-1$ of defect rates denoted $h_j^{\pm}$ as illustrated in Fig. 3.1d; these could be due to some inherent asymmetry in the network (i.e., if not all of the reactions making up the cycle are the same), and/or to local fluctuations in variables that affect reaction rates, such as concentration. The essential insight that our derivation provides is as follows: whereas in general the new eigenvalue ϕ, and therefore $\mathcal{R}$ and T, depend on all the details of the perturbed transition rate matrix, when the value of $\exp(-\mathcal{A}/N)$ is large, significant simplifications are possible, leading to expressions that depend only on the *values* of the defect rates and not their *relative locations*.

3.3.2.2 Transfer matrix formulation

Rather than directly perturbing $\mathbf{W}^{(0)}$, which would restrict the defect rates to be close to the uniform rates, we recast the eigenvalue problem in terms of transfer matrices [141]. The transfer matrix formulation is useful for studying the properties of systems with high degrees of translational symmetry and rapidly decaying spatial interactions and has been used to study localization in tight binding models [22] and neural networks [2], as well as dynamic [141] and structural phase transitions [96].

Consider the eigenvalue equation for the circulant matrix $\mathbf{W}^{(0)}$,

$$\mathbf{W}^{(0)}\vec{f} = \phi^{(0)}\vec{f}. \tag{3.10}$$

We can then write

$$-(k^- + k^+)f_1 + k^- f_2 + k^+ f_N = \phi^{(0)} f_1, \tag{3.11}$$

$$-(k^- + k^+)f_2 + k^- f_3 + k^+ f_1 = \phi^{(0)} f_2, \tag{3.12}$$

and so forth. Solving for f_1 in Eq. 3.12 gives

$$f_1 = \frac{\phi^{(0)} + k^- + k^+}{k^+} f_2 - \frac{k^-}{k^+} f_3, \tag{3.13}$$

which we can also write as

$$\begin{bmatrix} f_1 \\ f_2 \end{bmatrix} = \begin{bmatrix} \frac{\phi^{(0)}+k^-+k^+}{k^+} & -\frac{k^-}{k^+} \\ 1 & 0 \end{bmatrix} \begin{bmatrix} f_2 \\ f_3 \end{bmatrix} \equiv \mathbf{B}_0 \begin{bmatrix} f_2 \\ f_3 \end{bmatrix}. \tag{3.14}$$

Thus, $\mathbf{B}_0$ maps the eigenvector magnitudes (f_{i-1}, f_i) to (f_i, f_{i+1}). Because the matrix $\mathbf{B}_0$ is the same for each link in the unicyclic network with uniform rates, we have

$$\begin{bmatrix} f_1 \\ f_2 \end{bmatrix} = \mathbf{B}_0^N \begin{bmatrix} f_1 \\ f_2 \end{bmatrix}, \tag{3.15}$$

so that $\mathbf{B}^N$ must have an eigenvalue of 1. Solving for the eigenvalues of $\mathbf{B}_0^N$ will give a polynomial of order $(\phi^{(0)})^N$, the N roots of which are the N eigenvalues of the transition matrix $\mathbf{W}_0$. This gives us an alternative to Eq. 3.10 for finding $\phi^{(0)}$.

3.3.2.3 One-defect rate

We first consider how adding one set of defect rates $h^{\pm}$ shifts ϕ. To do so, we replace one of the $\mathbf{B}_0$ matrices in the product in Eq. 3.15 by

$$\mathbf{A} \equiv \begin{bmatrix} \frac{\phi+h^-+h^+}{h^+} & -\frac{h^-}{h^+} \\ 1 & 0 \end{bmatrix}, \tag{3.16}$$

which maps the eigenvector elements on either side of the link with the defect rates, so that now the eigenvalue of $\mathbf{AB}^{N-1}$ is equal to 1. Now the $\mathbf{B}$ matrix has changed, because modifying the rates changes the value of ϕ. We write ϕ in the most general way, as

$$\phi = \phi^{(0)} + C\gamma, \tag{3.17}$$

where C is a constant to be determined and γ is an unknown to be calculated. This implies

$$\mathbf{B} = \mathbf{B}_0 + \begin{bmatrix} C\gamma/(k^+) & 0 \\ 0 & 0 \end{bmatrix} \equiv \mathbf{B}_0 + \mathbf{B}_1. \tag{3.18}$$

We now proceed with the matrix perturbation of $\mathbf{B}$. First, we compute the eigenvalues (β_i) and normalized eigenvectors of $\mathbf{B}_0$. Note that since $\mathbf{B}_0$ is non-Hermitian, its right and left eigenvectors ($\langle i|$ and $|i\rangle$) are not the same. We obtain

$$\beta_1^0 = e^{2\pi i/N} \qquad \beta_2^0 = (k^-/k^+)e^{-2\pi i/N} \tag{3.19}$$

$$|1_0\rangle = \frac{1}{c_1}(\beta_1^0, 1) \qquad |2_0\rangle = \frac{1}{c_2}(\beta_2^0, 1) \tag{3.20}$$

$$\langle 1_0| = \frac{1}{c_1}(-1/\beta_2^0, 1) \qquad \langle 2_0| = \frac{1}{c_2}(-1/\beta_1^0, 1) \tag{3.21}$$

$$c_1^2 = 1 - \beta_1^0/\beta_2^0 \qquad c_2^2 = 1 - \beta_2^0/\beta_1^0. \tag{3.22}$$

Now we compute the first-order correction to the eigenvalues,

$$\beta_1^{(1)} = \langle 1_0|\mathbf{B}_1|1_0\rangle = -\frac{e^{4\pi i/N}}{c_1^2}\frac{C\gamma}{k^-}. \tag{3.23}$$

We choose

$$C = -c_1^2 k^- e^{-2\pi i/N} \tag{3.24}$$

so that

$$\beta_1 = e^{2\pi i/N}(1+\gamma). \tag{3.25}$$

Similarly,

$$\beta_2 = \frac{k^-}{k^+}e^{-2\pi i/N}(1+\gamma) = e^{-\mathcal{A}/N}e^{-2\pi i/N}(1+\gamma). \tag{3.26}$$

Since $\mathbf{B}$ is a two-by-two matrix, we can compute its exact eigenvalues and check how the error in our perturbative approximations of β_1 and β_2 scales. The exact eigenvalues of $\mathbf{B}$ are

$$\beta^{\pm}_{\text{exact}} = \frac{e^{-2\pi i/N}}{2}\Big(e^{-\mathcal{A}/N}(1-\gamma) + e^{4\pi i/N}(1+\gamma) \\ \pm \left[-4e^{4\pi i/N}e^{-\mathcal{A}/N} + \left(e^{-\mathcal{A}/N}(1-\gamma) + e^{4\pi i/N}(1+\gamma)\right)^2\right]^{1/2}\Big). \tag{3.27}$$

If we ignore terms of order $e^{-\mathcal{A}/N}$ compared to terms of order 1, the expressions above simplify to

$$\lim_{\exp(-\mathcal{A}/N)\to 0}\beta^{\pm}_{\text{exact}} = \frac{e^{2\pi i/N}}{2}\left((1+\gamma) \pm (1+\gamma)\right), \tag{3.28}$$

giving

$$\lim_{\exp(-\mathcal{A}/N)\to 0}\beta^{+}_{\text{exact}} = \beta_1, \qquad \lim_{\exp(-\mathcal{A}/N)\to 0}\beta^{-}_{\text{exact}} = 0. \tag{3.29}$$

We can now compute $\mathbf{B}^{N-1}$ using

$$\mathbf{B}^{N-1} = \sum_i \beta_i^{N-1} \mathbf{X}_i^0, \tag{3.30}$$

where $\mathbf{X}_i^0 \equiv |i_0\rangle \langle i_0|$.

Since $\beta_2^{(1)} \propto e^{-\mathcal{A}/N} < 1$, if $\mathcal{A}/N$ is sufficiently large, all of the terms containing β_2 will vanish. Then the product $\mathbf{A}\mathbf{B}^{N-1}$ becomes

$$\mathbf{A}\mathbf{B}^{N-1} = \beta_1^{N-1} \mathbf{A}\mathbf{X}_1^{(0)} \equiv \beta_1^{N-1} \mathbf{Z}. \tag{3.31}$$

We now compute this product and set its eigenvalue equal to 1 in order to solve for ϕ. We find

$$\mathbf{Z} = \frac{1}{c_1^2} \begin{bmatrix} da & db \\ a & b \end{bmatrix}, \tag{3.32}$$

where

$$d(h^{\pm}) = \frac{\gamma + e^{-2i\pi/N}(k^- - h^-) + k^+ e^{2i\pi/N} + h^- + h^+ - k^- - k^+}{h^+}, \tag{3.33}$$

$$a = -e^{4\pi i/N} k^+/k^-, \quad \text{and} \tag{3.34}$$

$$b = e^{2\pi i/N}. \tag{3.35}$$

Since the two rows of $\mathbf{Z}$ are related by a constant, $\mathbf{Z}$ has a zero eigenvalue. The nontrivial eigenvalue ζ of $\mathbf{Z}$ is

$$\zeta = \frac{e^{2\pi i/N} \left(k^+ e^{2\pi i/N} (-C\gamma - h^- - h^+ + k^- + k^+) + h^- k^+ + h^+ k^- - k^- k^+ - e^{4\pi i/N} {k^+}^2 \right)}{c_1^2 h^+ k^-}. \tag{3.36}$$

We can now solve for γ using

$$1 = \beta_1^{N-1}\zeta \tag{3.37}$$

$$= e^{-2\pi i/N}(1+\gamma)^{N-1}\zeta. \tag{3.38}$$

For notational simplicity, we absorb the $e^{-2\pi i/N}$ term into ζ, letting

$$\zeta' = e^{-2\pi i/N}\zeta. \tag{3.39}$$

Rearranging, we have

$$(1+\gamma) = \zeta'^{1/(1-N)}. \tag{3.40}$$

We now rewrite $\zeta'^{1/(1-N)}$ as $\exp\Big(\log\Big(\zeta'^{1/(1-N)}\Big)\Big) = \exp\Big(\Big(\frac{1}{1-N}\Big)\log\big(\zeta'\big)\Big)$ and expand to second order, giving

$$\gamma \approx \frac{1}{1-N}\log\big(\zeta'\big) + \frac{1}{2(1-N)^2}(\log\big(\zeta'\big))^2. \tag{3.41}$$

This gives a self-consistent equation for γ (since ζ' is a function of γ). To obtain the numerical results presented in Section 3.3.3 below, we solved Eq. 3.41 numerically by searching for roots of the equation in the neighborhood of an explicit approximation for γ that we obtain by expanding the logarithm in Eq. 3.41 to linear order. We rewrite ζ' (defined in Eq. 3.39) as

$$\zeta' = \zeta'_0 - \gamma\frac{k^+e^{2\pi i/N}C}{c_1^2h^+k^-} = \zeta'_0 - \gamma\frac{k^+}{h^+}, \tag{3.42}$$

where ζ'_0 is independent of γ. We then expand the logarithm as

$$\log\big(\zeta'\big) = \log\left(\zeta'_0 - \gamma\frac{k^+}{h^+}\right) \tag{3.43}$$

$$= \log\left(\zeta'_0\left(1 - \gamma\frac{k^+}{h^+\zeta'_0}\right)\right) \tag{3.44}$$

$$\approx \log\big(\zeta'_0\big) - \gamma\frac{k^+}{h^+\zeta'_0}, \tag{3.45}$$

where in the last line we have used $\log(1+x) \approx x$ for $x \ll 1$. Plugging this back into Eq. 3.41 and keeping only the term linear in $1/(1-N)$ gives

$$\gamma \approx \frac{1}{1-N}\left[\log\left(\zeta_0'\right) - \gamma\frac{k^+}{h^+\zeta_0'}\right]. \tag{3.46}$$

3.3.2.4 Many-defect rates

We can extend Eq. 3.41 to the case where many (m) of the rates are defects. The product of transfer matrices in this case is

$$\begin{bmatrix} f_1 \\ f_2 \end{bmatrix} = \mathbf{A}_1\mathbf{B}^{L_1}\cdots\mathbf{A}_j\mathbf{B}^{L_j}\cdots\mathbf{A}_m\mathbf{B}^{L_m}\begin{bmatrix} f_1 \\ f_2 \end{bmatrix}, \tag{3.47}$$

where L_j is the distance (the number of uniform rates) between neighboring defect rates. Generally, Eq. 3.47 has 2^m terms. However, if $e^{-L_j\mathcal{A}/N}$ is sufficiently large, we can ignore β_2 as we did in the case of one defect above. Then Eq. 3.47 reduces to a single term from which we can factorize β_1, giving

$$\begin{bmatrix} f_1 \\ f_2 \end{bmatrix} = \beta_1^{N-m}\mathbf{A}_1\mathbf{X}_1^{(0)}\cdots\mathbf{A}_j\mathbf{X}_1^{(0)}\cdots\mathbf{A}_m\mathbf{X}_1^{(0)}\begin{bmatrix} f_1 \\ f_2 \end{bmatrix}. \tag{3.48}$$

The affinity thus sets a correlation length for the defects; if the affinity per site ($\mathcal{A}/N$) is sufficiently large, the spacing between them does not matter. In principle, the order of the matrices in the matrix product in Eq. 3.48 is still important, and hence the value of ϕ depends on the order of the defects. However, our calculations are simplified due to the special symmetry of $\mathbf{Z}_j \equiv \mathbf{A}_j\mathbf{X}_1^{(0)}$ (given by Eq. 3.32, with the defect rates $h^\pm$ now indexed $h_j^\pm$, etc.). We find that the nontrivial eigenvalue of the product $\mathbf{Z}_i\mathbf{Z}_j$ is the product of the nontrivial eigenvalues of $\mathbf{Z}_i$ and $\mathbf{Z}_j$. As a result, the expression for ϕ is simply determined by the product of the nontrivial eigenvalues of the $\mathbf{Z}_j$ matrices. Therefore, as long as $L_j \geq 1 \forall j$,

the order in which the defects are placed and the spacing between them becomes irrelevant as far as ϕ is concerned. We can thus simply extend our results for one defect to write

$$\phi = \phi^{(0)} + C\gamma \tag{3.49}$$

$$\gamma \approx \frac{1}{m-N}\sum_{j=1}^{m}\log\left(\zeta_j'\right) + \frac{1}{2(m-N)^2}\left(\sum_{j=1}^{m}\log\left(\zeta_j'\right)\right)^2, \tag{3.50}$$

where ζ_j' is a function of k^+, k^-, h_j^+, h_j^-, and N given by Eq. 3.36 and 3.39 but is independent of any of the other defect rates. The linear expansion about which we search for numerical roots solutions of Eq. 3.50 is

$$\gamma \approx \frac{1}{m-N}\left[\sum_{j=1}^{m}\log\left(\zeta_{0,j}'\right) - \gamma\frac{k^+}{\sum_{j=1}^{m}h_j^+\zeta_{0,j}'}\right]. \tag{3.51}$$

Our derivation of Eq. 3.50 requires $L_j \geq 1$ because the nontrivial eigenvalue of the product $\mathbf{Z}_i\mathbf{Z}_j$, where $\mathbf{Z}_j \equiv \mathbf{A}_j\mathbf{X}_1^{(0)}$, is the product of the nontrivial eigenvalues of $\mathbf{Z}_i$ and $\mathbf{Z}_j$. However, the eigenvalue of the product of $\mathbf{A}_i\mathbf{A}_j$ is *not* the product of their eigenvalues. Therefore, Eq. 3.50 should not be valid if there are defect rates on either side of the same node in the network ($L_j = 0$). Nonetheless, our numerical results in the main text show that these expressions accurately predict the eigenvalues of the oscillator even when $L_j = 0$ for nearly all of the defects. To understand how our theory is able to correctly predict the eigenvalue of systems with adjacent defects, we write the defect transfer matrix $\mathbf{A}_j$ as

$$\mathbf{A}_j = \begin{bmatrix} x_j & -y_j \\ 1 & 0 \end{bmatrix}, \tag{3.52}$$

where

$$x_j = \frac{\phi + h_j^- + h_j^+}{h_j^+} = \frac{h_j^- e^{-2\pi i/N} + h_j^+ e^{-2\pi i/N} + C\gamma/N}{h_j^+} \tag{3.53}$$

$$y_j = \frac{h_j^-}{h_j^+}. \tag{3.54}$$

In the limit of large N, we have

$$\lim_{N\to\infty} x_j = \frac{h_j^- + h_j^+}{h_j^+} = 1 + \frac{h_j^-}{h_j^+} \qquad\qquad y_j = \frac{h_j^-}{h_j^+}. \tag{3.55}$$

The eigenvalues of the product $\mathbf{A}_j\mathbf{A}_i$ are

$$\alpha_\pm^{ij} = \frac{1}{2}\left(\pm\sqrt{(x_i x_j + y_i + y_j)^2 - 4y_i y_j} + x_i x_j + y_i + y_j\right). \tag{3.56}$$

If we can ignore the y terms compared to the x terms, then these reduce to

$$\lim_{y/x\to 0} \alpha_1^{ij} = 0 \tag{3.57}$$

$$\lim_{y/x\to 0} \alpha_2^{ij} = x_i x_j, \tag{3.58}$$

and the eigenvalues of $\mathbf{A}_i$ become $\alpha_1^j = x_j, \alpha_2^j = 0$. Clearly, in this limit the eigenvalue of the product of transfer matrices is equal to the product of eigenvalues, as required, and the order of the defects will no longer matter even if they are adjacent. The limit is fulfilled when the affinity is high not only on average but additionally along every edge in the network, so that $h^-/h^+ \sim \exp(-\mathcal{A}/N)$.

Following the derivation above using x_j as the eigenvalue for the defect transfer matrices, we obtain the same result as in Eqs. 3.50 and 3.51, with ζ replaced by x. Indeed, we see that in the limit that $h^-/h^+ \to 0$ and $k^-/k^+ \to 0$, ζ reduces to x. This explains how our theory can handle many adjacent defects.

While Eqs. 3.49 and 3.50 are only formally correct in the limit of high affinity, in practice, as we show in Figs. 3.4 and 3.6, they predict ϕ well even for rather small values of $\mathcal{A}$. Specifically, $N/\mathcal{A}$ sets a length scale for correlations between defect rates, so that if $N/\mathcal{A} \ll 1$ the relative positions of defect rates do not affect ϕ. Generally, ϕ depends on $\mathcal{O}(N)$ parameters, including the values and locations of the uniform and defect rates in the model. Eqs. 3.49 and 3.50 predict that in the limit $N/\mathcal{A} \ll 1$, ϕ depends only on the values of the rates. As such, changes in the remaining, irrelevant parameters will not affect oscillator time scales—in other words, the oscillator is robust to these changes. As we demonstrate below, this implies that the period and coherence of oscillations can be maintained even in the presence of disorder in the rates.

3.3.3 Comparing to numerical simulations

3.3.3.1 As a function of the number of defect rates

To test the limits of Eq. 3.49, we compared it to the result of numerical diagonalization for networks of size $N = 100$ with up to 99 defect rates placed at random locations in the network. We considered networks with quenched disorder: we set all CCW rates to $k^- = h_j^- = 1$ and randomly selected the CW defect rates h_j^+ from a Gaussian probability distribution $P_G(\tilde{\sigma}, \mathcal{A}_0, N)$ with mean $k^+ = \exp(\mathcal{A}_0/N)$ and standard deviation $\sigma = \tilde{\sigma}\exp(\mathcal{A}_0/N)$ and with a lower cutoff at 0.1 so that we do not select rates that are very close to zero or negative. This prescription naturally allows the affinity to vary between networks. Fig. 3.4 shows the importance of a high affinity ($\mathcal{A}_0/N$, the value of the affinity in the uniform network) for controlling $\mathcal{R}$ and T. Our prediction from Eq. 3.49 improves with increasing $\mathcal{A}_0/N$. For $\mathcal{A}_0/N = 2$, Fig. 3.4 shows that Eq. 3.50 is accurate even when all but one of the rates in the network are random and $\langle\mathcal{R}\rangle$ is 40% less than the bound $\mathcal{R}_0$. (For comparison, the cycle of the KaiC hexamer has $\mathcal{A}/N \gtrsim 10$ [117, 136, 85].) In Fig. 3.5 we show similar results for networks with fixed affinity, which confirm the bound in Eq. 3.8.

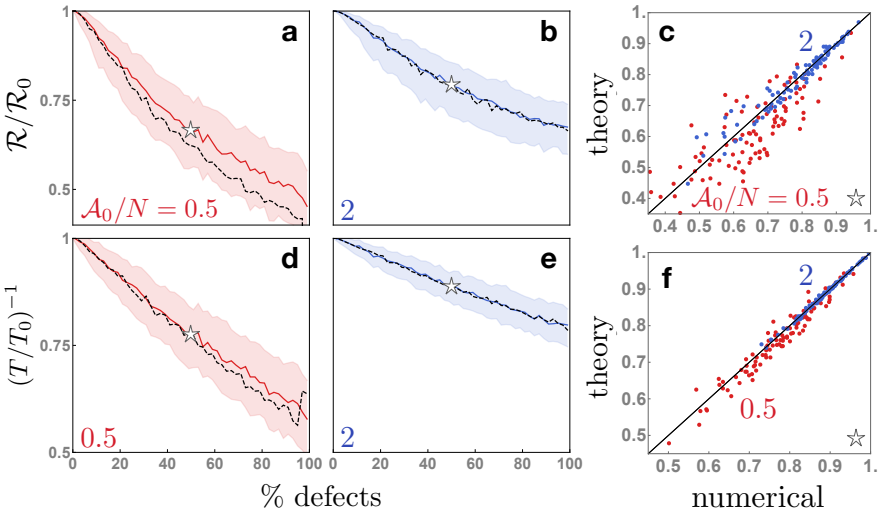

Figure 3.4: Coherence $\mathcal{R}$ (a,b) and period T (d,e) of an oscillator as a function of the percent of defect rates, and scatter plots of numerical and theory results for $\mathcal{R}$ (c) and T (f) in individual networks. The values of $\mathcal{R}$ and T are more robust (spread of values decreases) and predictable at the higher affinity $\mathcal{A}_0/N = 2$ (b,e) than at $\mathcal{A}_0/N = 0.5$ (a,d). Results are for networks with $N = 100$ states. All CCW rates are set to 1. CW defect rates h_j^+ are drawn from a Gaussian distribution with mean $k^+ = \exp(\mathcal{A}_0/N)$ and standard deviation $0.4k^+$. Because the distributions of $\mathcal{R}$ and T are asymmetric, we plot the median (solid line) $\pm$ one quartile (shaded region) of the numerical values for 500 samples of defect rates. The dashed lines are the median theoretical predictions for 500 samples of defect rates. For $\mathcal{A}_0/N = 2$ (blue, panels (b) and (e)), our theory is accurate even when % defects ≈ 100. On the right, we compare the values of (c) $\mathcal{R}/\mathcal{R}_0$ and (f) T_0/T for individual realizations of the random networks with 50% defects (parameters for panel (c) indicated by stars in panels (a,b); for panel (f), in panels (d,e)).

While minimizing phase diffusion and thereby maximizing $\mathcal{R}$ is crucial for a biochemical clock to keep time accurately, it is additionally important that T, the period of oscillations, be robust and tunable (for example, in order to match with an external signal [151]). Our theory (Eq. 3.50) shows that T can be reliably controlled in the high affinity limit even in the presence of substantial disorder, and we also find that the spread of T values decreases significantly with increasing affinity.

3.3.3.2 As a function of the spread of rates

The "number of defect rates" is a convenient measure of disorder to use in the context of our theory, but is not clearly related to a biological scenario. In general, we would expect

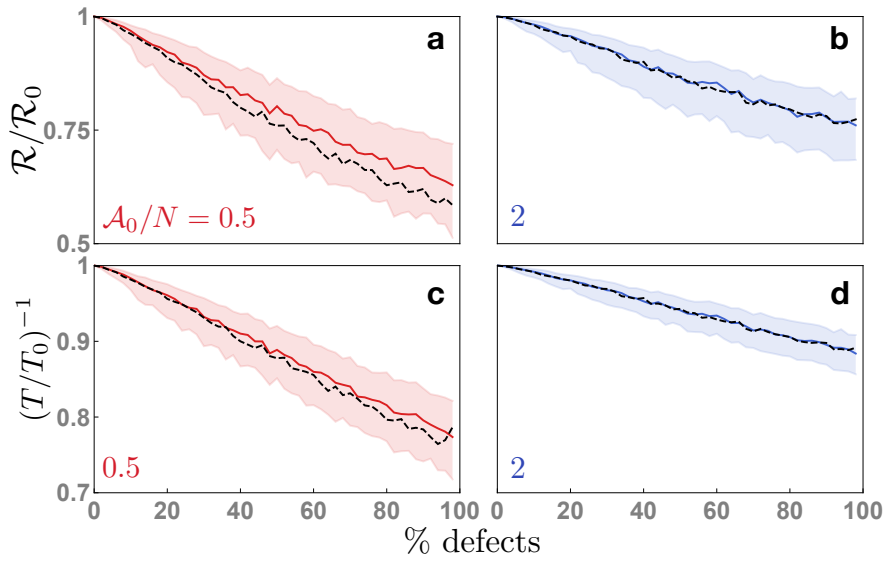

Figure 3.5: Coherence $\mathcal{R}$ (a,b) and period T (c,d) of an oscillator with $N = 100$ states as a function of the percent of defect rates. All counterclockwise rates are set to 1. We restrict ourselves to even numbers of defect rates. Half of the clockwise defect rates $\{h_j^+\}$ are drawn from the same distribution as in Fig. 3.4. We set the other half of the defect rates to $\{\exp(\mathcal{A}_0/N)^2/h_j^+\}$, ensuring that the affinity remains constant and equal to $\mathcal{A}_0$. Colors and lines have the same meaning as in Fig. 3.4.

all rates to be different from one another, even in the case where the underlying reaction network is relatively simple, as in the KaiC oscillator. This is because the rates of the oscillator depend on the collective state of the system, which is always changing [79], and in addition can be affected by local fluctuations in, for instance, the concentration of ATP. In Fig. 3.4 we showed that our perturbation theory can handle networks where no two rates are the same. In Fig. 3.6 we further investigate these fully disordered networks by showing how $\mathcal{R}$ and T vary as a function of the spread of rates σ in a network with all CCW rates set to 1 and all CW rates drawn from the distribution $P_G(\tilde{\sigma}, \mathcal{A}_0, N)$ (defined in the previous section). All of our findings still hold: the prediction becomes more accurate (Fig. 3.6a,b) and the spread of T and $\mathcal{R}$ values decreases (Fig. 3.6d) as the affinity $\mathcal{A}_0$ increases. In these networks the affinity naturally varies, and the average time scales are robust to these small variations. In Fig. 3.7 we show scatter plots comparing numerical values of the period with our analytical guess in specific realizations of the network. This data shows that we are not

restricted to predicting the median values shown in Fig. 3.6. Rather, our accurate prediction of the statistics of $\mathcal{R}$ and T for an ensemble of oscillators is due to the success of our theory at accurately predicting the time scales for individual oscillators.

Finally, we consider changes in the uniform rate, or $\mathcal{A}_0/N$. The bound in Eq. 3.8 implies that in a uniform network, the coherence $\mathcal{R}$ becomes insensitive to changes in the affinity at high $\mathcal{A}_0/N$ (Fig. 3.6c). However, it is not clear whether this will be the case in a disordered network. In Fig. 3.6 we show that even in a disordered network where $\mathcal{R} < \mathcal{R}_0$, the dependence of $\mathcal{R}$ on $\mathcal{A}_0/N$ vanishes smoothly for values of $\mathcal{A}_0/N$ greater than $\sim$5. In this regime, our analytical results demonstrate how—due to nonequilibrium driving—the coherence is insensitive to large global fluctuations in the affinity that change the average rate k^+ as well as to small local fluctuations that cause the rates to fluctuate about k^+.

3.3.4 Conclusions and future directions

Biochemical oscillators, which can function as internal clocks, operate in noisy environments that can affect the ability of the clock to tell time accurately; yet somehow these oscillations continue with a well-defined period over long times. Here, we present analytical calculations supported by numerical results that show how a biochemical oscillator modeled as a Markov jump process on a ring of states (Fig. 3.1) can use high chemical affinity (for instance, in the form of ATP) to robustly maintain and tune its time scales even in the presence of a substantial amount of disorder. While previous work has postulated an upper bound on the number of coherent oscillations that such a model can support in terms of the chemical affinity, the bound can be loose, and does not elucidate the dependence on the details of the rates in the network [6]. We close this gap by showing how affinity can dramatically decrease the number of relevant variables controlling the coherence and period of oscillations.

Specifically, we consider Markov state networks such as those in Fig. 3.1d and sample the rates from a probability distribution in order to mimic disorder in biological systems. We consider networks with quenched disorder in order to probe the synchronization between

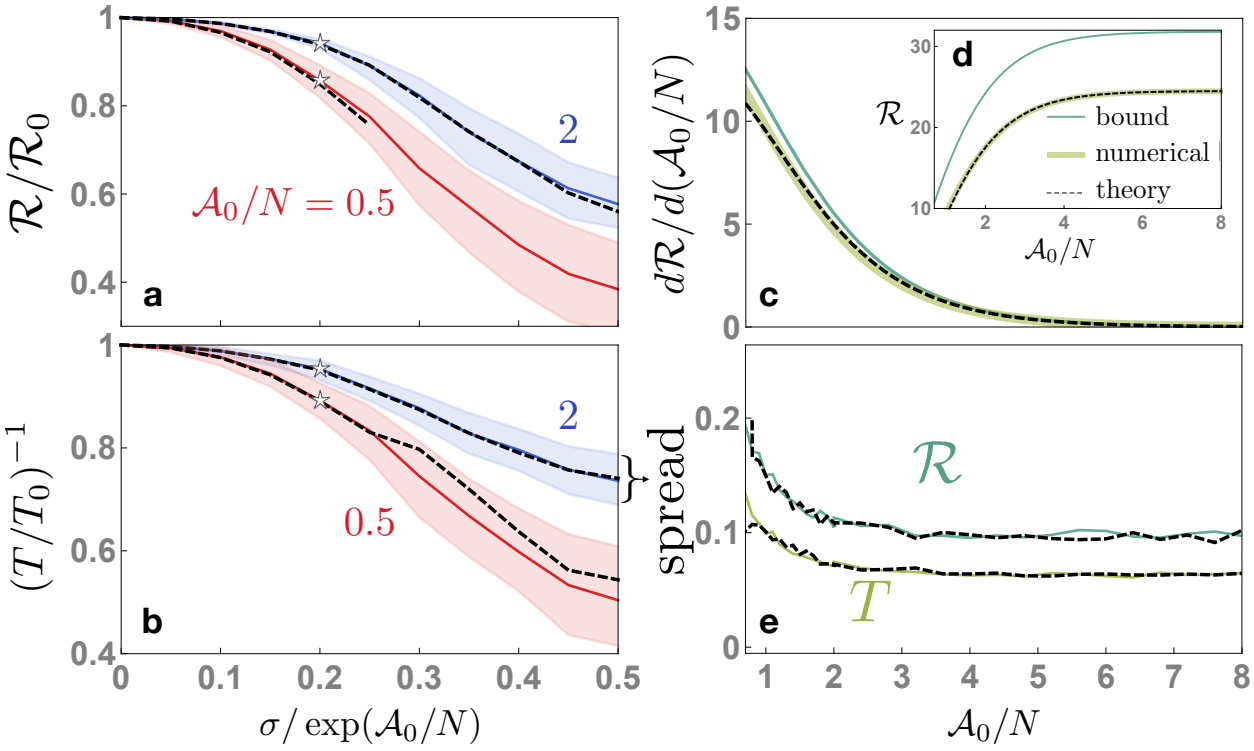

Figure 3.6: (a) $\mathcal{R}$ and (b) T for totally disordered networks of size $N = 100$ as a function of the standard deviation of the distribution of defect rates. All CCW rates are set to 1. CW defect rates h_j^+ are drawn from a Gaussian distribution with mean $k^+ = \exp(\mathcal{A}_0/N)$ and standard deviation $\sigma = \tilde{\sigma}k^+$. Black dashed lines are theoretical predictions. (c,d) The absolute value of $\mathcal{R}$ as a function of $\mathcal{A}_0/N$ (d) plateaus in a totally disordered network (here we show results for $\tilde{\sigma} = 0.3$) as well as in uniform networks (given by the bound in Eq. 3.8). As a result, $d\mathcal{R}/d(\mathcal{A}_0/N)$ (c) goes smoothly to zero in the disordered and uniform networks, even though $\mathcal{R}$ is far from the bound. (e) The "spread", defined as the distance between the median $\pm$ 1 quartile of the data, as a function of the affinity. As predicted, it decreases with increasing affinity.

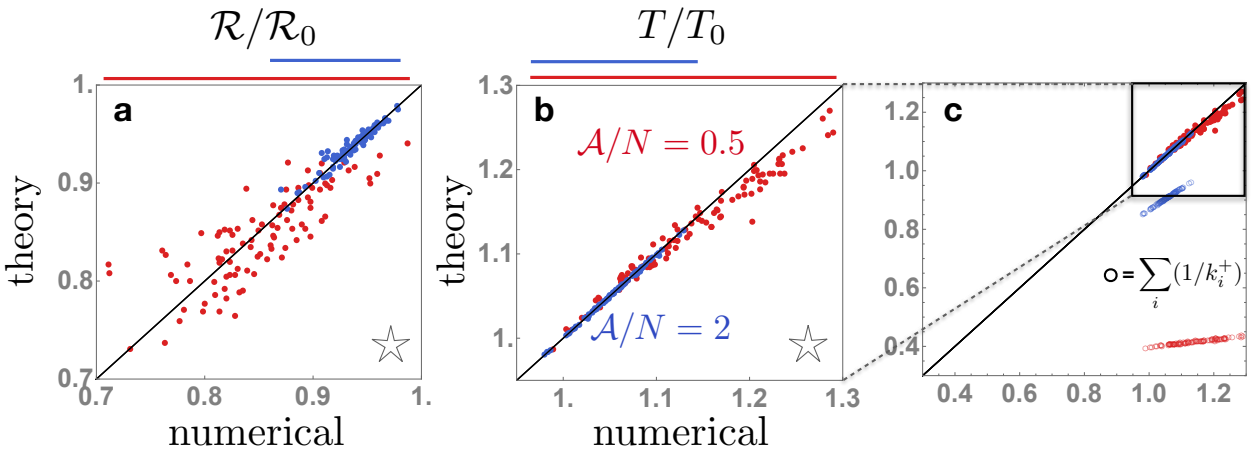

Figure 3.7: Comparing the values of (a) $\mathcal{R}/\mathcal{R}_0$ and (b) T/T_0 for individual realizations of random networks. Each point represents the period of a network with randomly generated rates with parameters indicated by a star in Fig. 3.6a,b. (c) Open circles in the zoomed-out T/T_0 scatter plot represent the approximation in the limit where reverse steps can be neglected ($T = \sum_i 1/k_i^+$). At $\mathcal{A}_0/N = 0.5$, where neglecting reverse steps underestimates the period by more than 50% (open red circles), our theory provides an accurate estimate (filled red circles). Note that in Fig. 3.6 we plotted $(T/T_0)^{-1}$; here we plot (T/T_0) as it results in a more compact plot.

multiple noninteracting oscillators (e.g., in different cells [84]), and as a proxy for the variation in a single oscillator's period when the rates are fluctuating over time. Our analytical theory in Eqs. 3.49 and 3.50 reveals that in the limit of high affinity the arrangement of the rates becomes irrelevant, and the period of oscillations T and the number of coherent oscillations $\mathcal{R}$ depend only on the magnitude of the rates. As a result, in the limit of high affinity, we can accurately predict $\mathcal{R}$ and T for individual realizations of the rate disorder knowing only the values of the rates. We note that while our analytical results are formally valid only when $\exp(-\mathcal{A}/N) \to 0$, they do not completely neglect the possibility of reverse transitions on the network, where the period of the oscillator is simply $T = \sum_i 1/k_i^+$. In Fig. 3.7c we compare our theory to this trivial approximation and show that our prediction is quite accurate at small values of $\mathcal{A}/N$ where the trivial approximation underestimates the period by over 50%.

A consequence of our prediction is that for a given probability distribution of the rates, the possible values of $\mathcal{R}$ and T for different realizations of the rates are more narrowly

distributed about their average values because different arrangements of the rates no longer affect the time scales. Taken together, this means that when the affinity is high $\mathcal{R}$ and T can be well approximated from a small, fixed number of parameters (namely, enough to specify the single-site probability distribution of the rates), a number that does not scale with system size, as opposed to the $\mathcal{O}(N)$ parameters required to specify the values and locations of all the rates that are generally expected to determine $\mathcal{R}$ and T. Our results give further insight into why biochemical oscillators might evolve to consume large amounts of energy in the form of ATP [136]: in addition to the previously known function of suppressing uncertainty in the period of the oscillator for a system with uniform rates [19, 6], this energy consumption also makes the time scales of the oscillator more robust to fluctuations in the rates caused by the noisy environment of the cell by decoupling those rates.

Finally, we note that although we used the example of KaiABC in this work, the Markov cycle representation is not limited to post-translational oscillators with conserved protein copy numbers, and the more common transcription-translation oscillators can also be studied in this paradigm.

3.3.4.1 Connections to localization in random environments

We can contrast our results with expressions for the velocity and diffusion coefficients for periodic, disordered, one-dimensional Markov networks that have been derived previously in the literature [36]. First, the quantity we formally calculate in this chapter is different: it is an eigenvalue, as opposed to a first passage time. Second, the expressions in Ref. 36 include positional correlations between rates, which can modify the transport properties; simplified expressions require an assumption that the rates are uncorrelated. Our work shows how nonequilibrium driving can make these correlations irrelevant.

Despite these distinctions, the body of work on random walks in random environments and the closely related work on electron localization in random potentials suggest several possible connections and interesting directions for our work. Apart from expressions for the

first passage time, much of the work on random walks has focused on anomalous transport in random environments; that is, understanding the scaling of the mean $\langle x \rangle$ and the mean-squared-displacement $\langle x^2 \rangle$ with time. In particular, it is known that "normal" transport, that is, where $\langle x \rangle, \langle x^2 \rangle \propto t$, can break down when there are large fluctuations in the hopping rates [13]. In the context of oscillators, these results imply that there is a transition between a network that supports nonzero current, and therefore oscillations, and one that does not, and that if there is a large variance in the rates a finite affinity is a necessary but not sufficient condition to observe oscillations. Because we study eigenvalues rather than the closely related statistics of displacement, this transition will manifest as the condensation of eigenvalues of the transition rate matrix onto the real line. To study when this happens, we would need a theory in terms of the statistics of the rate matrices instead of the number of defect rates. In order to derive such a theory, we could turn to results that study large products of transfer matrices with random perturbations [35]. Since these results were derived with Andersen localization problems in mind, the transfer matrices are Hamiltonian; in our case, the broken symmetries related to the breaking of detailed balance would be a challenge. If successful, a theory in terms of the statistics of rates would allow us to characterize the dynamics of Markov models that support oscillations both as a function of the affinity and as a function of the disorder in the rates. In contrast, our current theory requires us to specify all of the rates of the model, which is useful in investigating a specific network but only allows us to investigate the effect of disorder indirectly, as rate statistics ($\langle k^{\pm} \rangle, \langle k^{\pm 2} \rangle$, etc.) do not show up explicitly in our theoretical expressions for the eigenvalue.

3.4 Multi-cycle oscillator models

3.4.1 Introduction

In Section 3.3 we explored the connection between dissipation and robustness using single-cycle Markov models of biochemical oscillators such as the one pictured in Fig. 3.1d. By

deriving an analytical expression for the period and coherence of oscillations that reveals their detailed dependence on all of the rates in the network, we showed that nonequilibrium driving allows the period of oscillators to become insensitive to many of the parameters of the models—specifically, the arrangement of the transition rates on the ring. Driving thus allows the period of a wide class of oscillators, even those operating far from the bound, to be robustly maintained in the presence of changes in these parameters. In this section we further explore this role of energy dissipation by extending our results to networks with multiple cycles. We show that, at high driving, the period of the oscillator is more robust to changes in the topology of the network as well as changes in the rates.

Our multi-cycle models are generated by "decorating" a main cycle with N states and affinity $\mathcal{A}$ with small cycles with $n \ll N$ states, as illustrated in Fig. 3.1f. The rates entering these decorations are modulated by a small parameter μ which allows us to tune the probability of leaving the main cycle and ensures that we recover a single-cycle model in the limit $\mu \to 0$.

Our theory for oscillator eigenvalues depends on the single-cycle topology of the networks studied in Section 3.3, so to apply it to these new networks, in Section 3.4.2 we show how to coarse-grain decorations onto single links, yielding an effective single-cycle network whose period and coherence are meant to approximate those of the full multi-cyclic network. Our perturbation theory requires a minor modification to be applied to the resulting coarse-grained networks, which can have very large bottlenecks. We describe the modification in Section 3.4.2.2. In Section 3.4.3 we compare these observables calculated numerically in multi-cycle networks to the corresponding coarse-grained networks and analytical approximations, and show that at high affinity our analytical approximation, which takes as input only a small subset of the parameters required to specify the multi-cycle network, accurately reproduces the period and coherence of these networks. We demonstrate the ability of our theory to predict time scales when the rates and topology in the network are randomly generated. Finally, in Section 3.4.4, we discuss the implications of our results for biochemical

oscillators and show one example of how the multi-cycle networks studied here can be used to achieve input compensation, which is the ability to maintain a constant period when the affinity changes.

3.4.2 Coarse-graining via first passage time statistics

We now wish to apply Eqs. 3.49 and 3.50 to the networks with multiple cycles depicted in Fig. 3.1f in order to understand how our conclusions extend to these higher-dimensional cases. The derivation of Eqs. 3.49 and 3.50 used a transfer matrix technique that depended on the single-ring topology of the network. Rather than trying to extend this approach to networks with decorations of the kind we wish to consider here, we took a different approach and chose instead to map multi-cycle networks onto single-cycle networks so that Eqs. 3.49 and 3.50 can then be applied directly to the mapped network. Because we want a mapping that preserves time scales, our approach is to build a single-cycle network with rates such that the mean and variance of the first passage time from a site upstream (in the sense of the probability current) of a decoration to a site downstream of the decoration is preserved (denoted by the green and red circles in Fig. 3.1f). For each decoration, we replace the rates along the edge shared by the large and small cycles with an effective CW rate η^+ and an effective CCW rate η^-.

3.4.2.1 Calculating the first passage time distribution

In order to do this, we first calculate the first passage time distribution across the decoration (from the green circle to the red circle in Fig. 3.1f) in Laplace space [88, 15]. The method for calculating the first passage time between two states is to sum over all of the paths of all lengths connecting the two states. First, we write down the first passage time distribution between two connected states 1 and 2. If the system enters state 1 at time t_0, the probability that it hops to state j at time $t_1 = t_0 + \mu t$ is

$$Q_{12}(\mu t) = P_{12}(\mu t) \prod_{i \neq 1,2} \left(1 - \int_0^{\mu t} dt P_{1i}(t) \right), \tag{3.59}$$

where $P_{12}(t) = k_{12} \exp(-k_{12} t)$ is the waiting time distribution for hopping from state 1 to 2. The first term is the probability of hopping at exactly time t_1, while the term in parentheses is the probability that the system has not hopped to any other state in the meantime. The net waiting time distribution out of state 1 is just the sum over connected states: $\sum_j Q_{1j}$.

The probability of observing a particular trajectory with transitions $\{1 \to 2, 2 \to 3, \cdots, n-1 \to n\}$ occurring at times $\{t_1, t_2, t_3, \cdots, t_{n-1}\}$ is

$$Q_{12}(t_1) Q_{23}(t_2 - t_1) \cdots Q_{n-1,n}(t_{n-1} - t_{n-2}). \tag{3.60}$$

Note that state 1 is the first state that the system visits; it is not necessarily a state with a fixed label. For example, state 1 and state 3 could both be the same state i, if the system's trajectory is $i \to j \to i$. State n is the only state that can be visited only once, since it is an absorbing state.

To obtain the first passage time distribution $F(n, t_{n-1}|1, 0)$, we sum over all trajectories that start at state 1 at time t_0 and arrive, for the first time, at state n at time t_{n-1}. We integrate over all possible combinations of transition times $\{t_1, \cdots t_{n-2}\}$, constrained such that t_{n-1} is fixed, and sum over all paths that the system can take:

$$\begin{aligned} &F(n, t_{n-1}|1, 0) = \\ &\sum_{paths} \int dt_1 \cdots dt_{n-2} Q_{12}(t_1) \cdots Q_{n-1,n}(t_{n-1} - t_{n-2}). \end{aligned} \tag{3.61}$$

We can turn this convolution into a product by taking the Laplace transform,

$$\hat{Q}_{ij} = \int_0^\infty dt e^{-st} P_{ij}(t) \prod_{k \neq i,j} \left(1 - \int_0^t dt' P_{ik}(t') \right), \tag{3.62}$$

so that we have

$$\hat{F}(n, t_{n-1}|1, 0) = \sum_{paths} \hat{Q}_{12} \times \hat{Q}_{13} \times \cdots \times \hat{Q}_{n-1,n}. \tag{3.63}$$

Since each transition in our Markov model is a Poisson process, we plug in an exponential form for P, giving

$$\hat{Q}_{ij}(s) = \tag{3.64}$$

$$k_{ij} \int_0^\infty dt e^{-st} e^{-k_{ij}t} \prod_{k \neq i,j} \left(1 - k_{ik} \int_0^t dt' e^{-k_{ik}t'}\right) \tag{3.65}$$

$$= \frac{k_{ij}}{s + \sum_{k \neq i} k_{ik}}. \tag{3.66}$$

To sum over paths, we will construct a matrix $\mathbf{K}$ with elements

$$K_{ij} = \begin{cases} \hat{Q}_{ij}(s) & \text{if states } i \text{ and } j \text{ are connected} \\ 0 & \text{otherwise} \end{cases} \tag{3.67}$$

K_{1n} then gives us the waiting time distributions for all paths of length 1 from state 1 to n. $[K^2]_{1n}$ gives us paths of length 2, and $[K^m]_{1n}$ gives all paths of length m. Summing,

$$\hat{F}(n, t_{n-1}|1, 0) = 1 + K_{1n} + [K^2]_{1n} + \cdots \tag{3.68}$$

$$= \sum_{m=0}^{\infty} [K^m]_{1n} \tag{3.69}$$

$$= [(\mathbb{1} - \mathbf{K})^{-1}]_{1n}. \tag{3.70}$$

All elements of the matrix $\mathbf{K}$ are strictly less than 1 since s is always positive, so the Frobenius norm of the matrix $\lim_{m\to\infty} \mathbf{K}^m < 1$ and the series converges. We could then invert the Laplace transform to obtain the first passage time distribution $F(t)$, but since that is often not tractable, here instead we use the fact that $\hat{F}(s)$ is a moment-generating function for

$F(t)$, with the nth moment $\langle \tau^n \rangle$ given by

$$(-1)^n \left(\frac{\partial^n \hat{F}}{\partial s^n} \right)_{s=0} = \langle \tau^n \rangle. \tag{3.71}$$

Moments of the first passage time distribution can thus be computed even when it is not easy to invert $\hat{F}(s)$ to obtain the real-time distribution $F(t)$. For the decoration in Fig. 3.1g, $\hat{F}_{\text{dec}}(s)$ is a function of μ, a, b, k^+, and k^-. For the line of states in Fig. 3.1h, $\hat{F}_{\text{line}}(s)$ is a function of k^+, k^-, and two unknown rates η^+ and η^-. By setting the mean and variance of F_{dec} and F_{line} equal to one another, we obtain analytical expressions for η^+ and η^- in terms of μ, a, b, k^+, and k^-. These expressions are algebraically complicated, so we give just one example of the full rates for the smallest motif considered—a triangle, as depicted in Fig. 3.1g:

$$\lambda\eta^+ = (k^- + k^+)^2 \left(a^2\mu + k^+(a+b) \right)^2 \tag{3.72}$$

$$\begin{aligned}
\lambda\eta^- &= \mu^3 a^3 b {k^+}^2 \\
&\quad + \mu^2 ab \left[ab(k^- + k^+)^2 + ak^+ \left(-{k^-}^2 - 2k^-k^+ + {k^+}^2 \right) + {k^+}^3(b + k^- + k^+) \right] \\
&\quad + \mu \Big[a^3 k^- (k^- + k^+)^2 - a^2 (k^- + k^+)^2 (k^+(k^- + k^+) - bk^-) \\
&\quad + ak^+ \left(b^2(k^- + k^+)^2 - bk^-k^+(k^- + 2k^+) + {k^+}^2(k^- + k^+)^2 \right) \\
&\quad + bk^+ \left(b^2(k^- + k^+)^2 + b{k^+}^3 + {k^+}^3(k^- + k^+) \right) \Big] \\
&\quad + k^-k^+(a+b)^2(k^- + k^+)^2
\end{aligned} \tag{3.73}$$

$$\begin{aligned}
\lambda &= \mu^3 a^3 b k^- \\
&\quad + a\mu^2 \left[a^2(k^- + k^+)^2 + ab \left({k^-}^2 + 4k^-k^+ + {k^+}^2 \right) + bk^+(bk^- - k^+(k^- + k^+)) \right] \\
&\quad + \mu \Big[a^3(k^- + k^+)^2 + a^2(k^- + k^+)^2(b + k^- + 2k^+) \\
&\quad - ak^+ \left(k^+(k^- + k^+)^2 - b(2k^- + k^+)(k^- + 2k^+) \right) + b{k^+}^2(bk^- - k^+(k^- + k^+)) \Big] \\
&\quad + k^+(a+b)^2(k^- + k^+)^2.
\end{aligned} \tag{3.74}$$

By calculating effective rates for all of the decorations in a network, we construct a single-cycle network that we expect to have a similar period T and coherence $\mathcal{R}$ (roughly captured by the first and second moments of the first passage time distribution, respectively) as the decorated network.

We note that this procedure does not always produce reasonable coarse-grained rates. The effective rates diverge at a value of μ that decreases as the size of the decoration increases (Table 3.1). As the size of the decoration becomes larger, it will eventually be able to support coherent oscillations of its own, leading to a system with multiple interacting periods of oscillation; in that case, one cycle is no longer dominant in terms of the dynamics of the system and we do not expect to be able to simply coarse-grain out these competing cycles. The effective rates can also become negative if the rates in the main cycle ($k^{+/-}$) and the decoration (a/b) are very different (as in different by orders of magnitude). We therefore restrict our study to small cycles with six or fewer sides, where the effective rates are positive for values of μ of at least $\mu = 0.05$, and to cases where $a = k^-$ and $b = k^+$, which we call "cis" because the rates in the main cycle and decoration favor current in the same direction through their shared edge, or where $a = k^+$ and $b = k^-$, which we call "trans" because the rates in the main cycle and decoration favor current in opposite directions through their shared edge. The probability of entering the decorations is tuned by changing μ. Compared to the trans configuration, the cis configuration favors cycling in the small decoration, as shown schematically in Fig. 3.8. In Table 3.1 we show the effective rates in the cis configuration in the limit where $k^-/k^+ \to 0$ (for the trans configuration this simple limit gives $\eta^+ = k^+$ and $\eta^- = 0$). In Fig. 3.8 we show $\eta^\pm$ as a function of μ for both configurations. The cis configuration leads to much more dramatic changes in the effective rates than does the trans configuration (Fig. 3.8), and $\mathcal{R}$ and T change by only a small fraction as μ is turned on in networks with trans-configured decorations. For the results in the following sections, we therefore focus on decorations with cis rates.

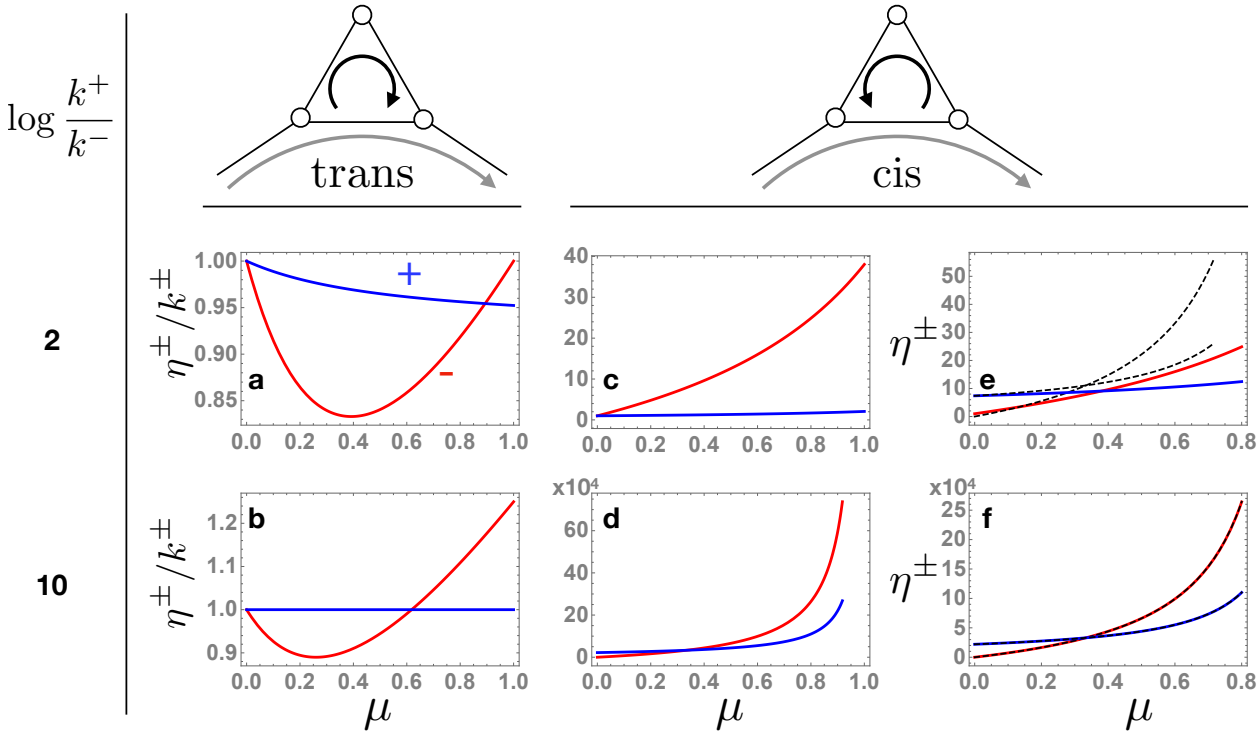

Figure 3.8: Effective rates resulting from the coarse-graining procedure as a function of μ, which controls the probability of entering the triangle. We consider the cases where $a = k^+$ and $b = k^-$ (trans, (a,b)) and where $b = k^+$ and $a = k^-$ (cis, (c–f)), for two values of $log\frac{k^+}{k^-}$, 2 (a,c,e) and 10 (b,d,f). (a–d) Relative values of the effective rates $\eta^{\pm}/k^{\pm}$ compared to the $\mu = 0$ values. The rates change much more dramatically in the cis case, because an extra, likely path for hopping CCW through the decoration is added. (e,f) Absolute values of the effective rates $\eta^{\pm}$ for the cis case. The black dashed lines are from the expressions for $\eta^{\pm}$ in the limit of $k^-/k^+ \to 0$, given in Table 3.1.

Shape	Exclusive Vertices	η^+	η^-
triangle	1	$k^+/(1-\mu)$	$3k^+\mu/(1-\mu)$
square	2	$k^+/(1-3\mu)$	$6k^+\mu/(1-3\mu)$
pentagon	3	$k^+/(1-6\mu)$	$10k^+\mu/(1-6\mu)$
hexagon	4	$k^+/(1-10\mu)$	$15k^+\mu/(1-10\mu)$
general	x	$\frac{2k^+}{2-x(x+1)\mu}$	$\frac{k^+(x+1)(1+x/2)}{2-x(x+1)\mu}$

Table 3.1: Effective rates across decorations with increasing numbers of sides, in the limit of $k^-/k^+ \to 0$. We deduce by inspection that the effective rates for a decoration with x vertices that do not belong to the large cycle are $\eta^+ = k^+/(1-\alpha\mu)$, $\eta^- = (x+1+\alpha)k^+/(1-\alpha\mu)$ where $\alpha = \sum_{i=1}^{x} i = x(x+1)/2$.

3.4.2.2 Extending the perturbation theory

In the coarse-grained networks with cis rate configurations in the decorations, we end up with $\eta^- \gg \eta^+$ along the coarse-grained links. We did not consider such cases in Section 3.3, and we need to modify our perturbation theory to handle them. Specifically, in Section 3.3 we approximated the product of transfer matrices as

$$\mathbf{A}\mathbf{B}^{N-1} \approx \mathbf{A}\left[\left(\beta_1^{(1)}\right)^{N-1}\mathbf{X}_1^{(0)} + \left(\beta_2^{(1)}\right)^{N-1}\mathbf{X}_2^{(0)}\right] \tag{3.75}$$

$$\approx \left(\beta_1^{(1)}\right)^{N-1}\mathbf{A}\mathbf{X}_1^{(0)}, \tag{3.76}$$

where $\beta_1^{(1)} = \exp(2\pi i/N)(1+\gamma) = \beta_1^{(0)}(1+\gamma)$ and $\beta_2^{(1)} = (k^-/k^+)\exp(2\pi i/N)(1+\gamma) = \beta_2^{(0)}(1+\gamma)$ are first-order perturbed eigenvalues of $\mathbf{B}$ and $\mathbf{X}_i^{(0)} = |i^{(0)}\rangle\langle i^{(0)}|$ is the outer product of the ith unperturbed eigenvectors. In the second line, we have assumed high affinity : $k^-/k^+ \ll 1$. The ith left and right eigenvectors of $\mathbf{B}$ are given by

$$\langle i| = \{-1/\beta_j, 1\}/c_i^2 \qquad\qquad |i\rangle = \{\beta_i, 1\}/c_i^2, \tag{3.77}$$

where c_i is a normalization constant. Therefore, by using $\mathbf{X}_1^{(0)}$, our theory ignored important terms containing γ. In cases where $k^-/k^+ \ll 1$ and $h^-/h^+ \ll 1$, we find that these terms cancel and our theory works with $\mathbf{X}_1^{(0)}$, explaining the success of our theory in predicting time scales in Section 3.3. However, in the coarse-grained networks studied in this section (specifically for decorations with the cis configuration), we often have $h^-/h^+ > 1$. We therefore replace

$$\mathbf{X}_1^{(0)} = \frac{1}{c_1^2}\begin{bmatrix} -\beta_1^{(0)}/\beta_2^{(0)} & \beta_1^{(0)} \\ -1/\beta_2^{(0)} & 1 \end{bmatrix} \tag{3.78}$$

with

$$\mathbf{X}_1^{(1)} = \frac{1}{c_1^2}\begin{bmatrix} -\beta_1^{(1)}/\beta_2^{(1)} & \beta_1^{(1)} \\ -1/\beta_2^{(1)} & 1 \end{bmatrix} \tag{3.79}$$

in Eq. 3.76, and proceed with the calculation (as described in Section 3.3.2) to obtain Eqs. 3.49 and 3.50, where

$$\begin{aligned}\zeta_j =& \frac{h_j^- k^+ + h_j^+ k^- - k^- k^+ + 2\gamma h_j^+ k^- + \gamma^2\left(h_j^+ k^- + k^- k^+\right)}{(\gamma+1)h_j^+\left(k^- - k^+ e^{\frac{4i\pi}{N}}\right)} \\ &+ \frac{(\gamma+1)k^+ e^{\frac{2i\pi}{N}}(-h_j^- - h_j^+ + k^- + k^+) - \left((\gamma+1)k^+ e^{\frac{2i\pi}{N}}\right)^2}{(\gamma+1)h_j^+\left(k^- - k^+ e^{\frac{4i\pi}{N}}\right)},\end{aligned} \tag{3.80}$$

$$C = c_1^2 k^- e^{-2\pi i/N}, \quad \text{and} \tag{3.81}$$

$$c_1^2 = 1 - (k^+/k^-)e^{4\pi i/N}. \tag{3.82}$$

To reiterate the conclusions of Section 3.3, the essential feature of these equations is that Eq. 3.50 depends independently on each rate $h_j^{\pm}$ and does not contain any information about the relative positions of the rates in the network. As a result, in the limit of moderately high affinity, spatial correlations vanish and the rates only contribute additively to the time scales, so we find that $\mathcal{R}$ and T are insensitive to the arrangement of the rates in the network. From a biological perspective, this means that the farther an oscillator operates from equilibrium, the more robust it will be to changes in the relative positions of the rates. In a large enough network, these rearrangements are akin to a scenario in which the values of the rates change but the distribution from which they are drawn stays the same (i.e., the rates fluctuate), and hence the oscillator is also more robust to fluctuations in the rates.

Since Eq. 3.50 is a self-consistent equation for γ, as in Section 3.3 the theoretical predictions in Section 3.4.3 are obtained numerically by searching for solutions to Eq. 3.50 near to a linear approximation of Eq. 3.50.

3.4.3 Comparing to numerical results

We can now compare T and $\mathcal{R}$ for our coarse-grained networks to the full networks. We calculate T and $\mathcal{R}$ in three ways: first, by numerically diagonalizing the transition rate matrix of a network with explicit decorations ($\mathcal{R}/T_{\text{exact}}$); second, by numerically diagonalizing the transition rate matrix of the corresponding coarse-grained network ($\mathcal{R}/T_{\text{CG}}$); and third, using the theoretical expressions in Eqs. 3.49 and 3.50 with the rates in the coarse-grained network as input ($\mathcal{R}/T_{\text{th}}$).

In the following sections, we test the ability of our coarse-graining scheme combined with our analytical theory to predict T and $\mathcal{R}$ in networks with increasing amounts of randomness. Since our theory does not contain information about the locations of the effective rates in the network, if we are able to predict these observables it means that they are insensitive to the locations of decorations on the network and will be robust to any changes in the locations of the decorations.

3.4.3.1 Fixed cycles

First, we test the accuracy of the coarse-grained and theoretical approximations for a fixed network topology. In Fig. 3.9 we show results for two types of networks: one with a large cycle of size $N = 100$ with a single triangle decoration, where we calculate $\mathcal{R}$ and T as a function of μ, and a second with μ fixed and m evenly spaced triangle decorations, where we calculate $\mathcal{R}$ and T as a function of m. All of the rates in the large cycle are set to $k^- = 1$ and $k^+ = \exp(\mathcal{A}_0/N)$, where $\mathcal{A}_0$ is the affinity in a network with no decorations, and the rates in the decorations are $a = k^-$ and $b = k^+$. When $m = 1$, $T/\mathcal{R}_{\text{CG}}$ approaches $T/\mathcal{R}_{\text{exact}}$ as the affinity increases, with perfect agreement in the limit of very high affinity ($k^-/k^+ = \exp(-10) \approx 0$). Note that in this limit the effective reverse hopping rates along edges representing coarse-grained decorations are not suppressed; rather, they are enhanced (Fig. 3.8), and $\eta^-/\eta^+ > 1$ (Fig. 3.8f), so that even in the limit $k^-/k^+ \to 0$ it is nontrivial to predict the period. The agreement between $T/\mathcal{R}_{\text{th}}$ and $T/\mathcal{R}_{\text{CG}}$ is also excellent. The

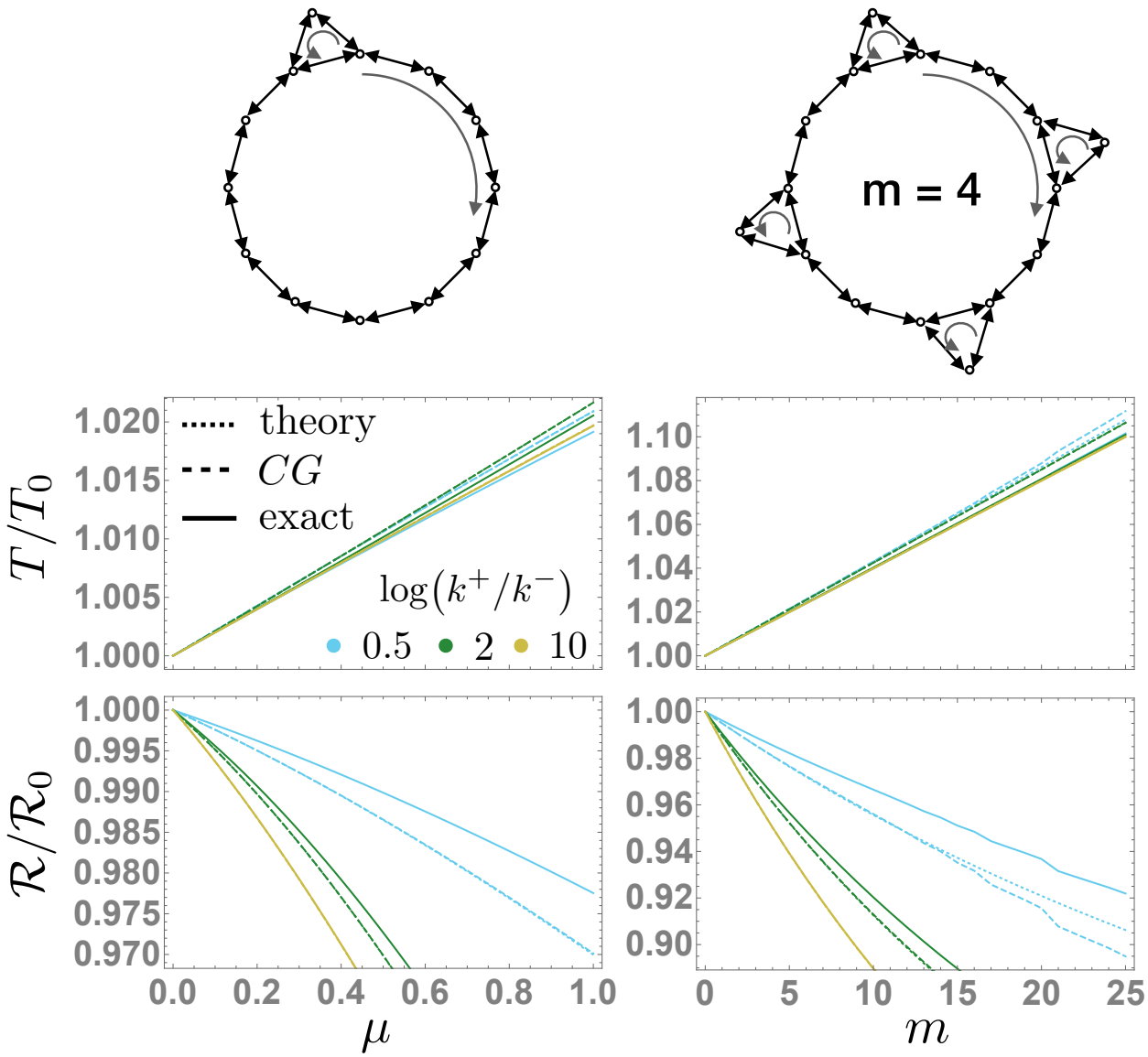

Figure 3.9: Period T and number of coherent oscillations $\mathcal{R}$ in networks with $N = 100$ states in the main cycle and triangle decorations with the cis configuration of rates ($a = k^-, b = k^+$). We set $k^- = 1$ and set $k^+ = \exp(\mathcal{A}_0/N)$. $\mathcal{A}_0$, R_0, and T_0 are the values in a network with no decorations. "Exact" results are calculated from numerical diagonalization of the full network. "CG" results are calculated from numerical diagonalization of a single cycle with $N = 100$ states with effective rates through the links where decorations are located in the full network. "Theory" results are calculated from the theoretical expression in Eqs. 3.49 and 3.82 with the rates $\{h_j^{\pm}\}$ given by the effective rates. Note that as affinity increases, first the theory and CG lines and then all three lines overlap. On the left, we show results for networks with one triangle decoration as a function of μ, which governs the probability of entering the decoration (see Fig. 3.1). On the right, we show results for networks with μ fixed at 0.2 and with m triangle decorations separated by $\lfloor N/m \rfloor$ edges. This value jumps when $N \mod m$ is 0, resulting in the observed discontinuous changes at these values when $\mathcal{A}_0/N = 0.5$.

net effect is convergence between exact values and theoretical predictions for T and $\mathcal{R}$ with increasing affinity.

The distance between decorations is given by $\lfloor N/m \rfloor$. At low affinity, this results in discontinuous jumps in the values of $T/\mathcal{R}_{\text{exact}}$ and $T/\mathcal{R}_{\text{CG}}$ (blue lines in the right column of Fig. 3.9) at values of m where N is an integer multiple of m, because the distance between the decorations is important. At high affinity the distance no longer matters, as predicted by our theory, and the CG and exact lines become smooth and ultimately match the theory prediction.

3.4.3.2 Random decorations

The success of our theory in predicting time scales in Fig. 3.9 suggests that networks with many different arrangements of the same set of decorations (or of similar sets drawn from a common distribution) can have the same values of T and $\mathcal{R}$. We now introduce disorder by fixing the number of decorations m to 25 and the value of μ to 0.05 and selecting the shapes and locations of decorations in the network randomly, with all other parameters the same as in Fig. 3.9. Because our coarse-graining scheme takes into account the edges CW and CCW from the decoration, we do not expect it to work well when two decorations are connected to the same vertex, and we constrain the random locations so that this does not happen (i.e., so that decorations are separated by at least one edge). The decorations have three to six sides. Scatter plots in which each point represents one realization of the quenched shape and location disorder are shown in Fig. 3.10. The results show that in these disordered networks, the exact, CG, and theory results converge at high affinity, confirming that the arrangement of decorations is unimportant at high affinity.

There are two features of Fig. 3.9 that highlight the limitations of our coarse-graining. First, while the spread of T values in the coarse-grained networks and our theoretical approximations decreases with increasing affinity, it increases slightly in the full networks. Second, we note that the coarse-grained networks systematically overestimate the period of the full

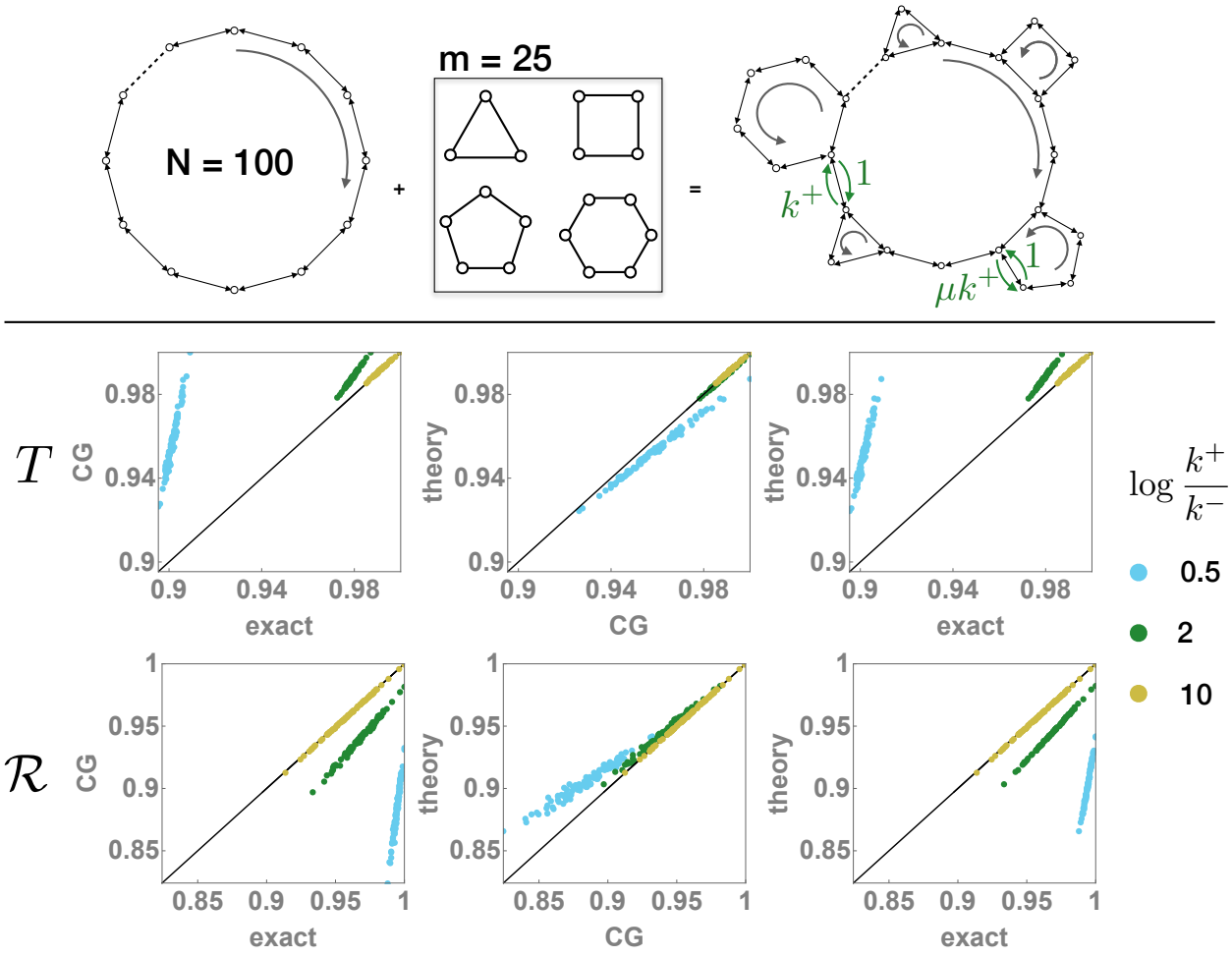

Figure 3.10: Period T and number of coherent oscillations $\mathcal{R}$ in networks with $N = 100$ states in the main cycle and $m = 25$ decorations whose shapes and locations are randomly generated, with the constraint that no vertex is connected to more than three neighbors (i.e., the decorations are separated by at least one edge). The rates are chosen as in Fig. 3.9, except that we chose $\mu = 0.05$ since the effective rates for larger decorations diverge at decreasing values of μ (see Table 3.1). Each point in the scatter plots represents a specific realization of quenched disorder of shapes and locations. As $\mathcal{A}_0/N = \log\left(k^+/k^-\right)$ increases, the exact, coarse-grained, and theory values converge. All values are normalized by the largest value in the data on each scatter plot so that data for different affinities can be shown on the same plot.

networks, with the values converging at high affinity. Both are a consequence of our coarse-graining, which is based on the first passage time from the green node to the red vertex in Fig. 3.1f. Since the red state is an absorbing state, this calculation does not take into account cases where the system arrives at the red vertex and then goes back into the decoration, or reenters the decoration from a state downstream in the large cycle. When the system enters the decoration, if both μ and the affinity are small, it may only explore one or two links of the decoration rather than completing the full cycle. In that case, different decorations will be indistinguishable as far as the dynamics are concerned. In the coarse-grained network, this microscopic detail is ignored; the rates of backward hops in the decorations, if they occur, are always different for different cycle sizes. This explains why networks with different sets of decorations are equivalent at low affinity in the full network but not in the coarse-grained network. At high affinity, these reentry events are very unlikely, so the CG time scales match the full network. Moreover, since any reverse hops across decorations in the CG network correspond to a full cycle, while in the full network the cycle may be only partially explored, the time spent in the decorations is always overestimated by the coarse-graining.

3.4.3.3 Random decorations and random rates

Finally, we test how our theory performs when disorder in the rates, explored in Section 3.3, is combined with random network topology (Fig. 3.11). We now generate networks with large cycles of size $N = 500$ and $m = 50$ decorations with random shapes and random locations. The locations are again constrained so that no two decorations are connected to the same vertex. The CCW rates in the large cycle are set to $k^- = 1$, and the CW rates that are not part of the coarse-grained motif (i.e., are not connected to a vertex that is part of a decoration) are then chosen randomly from a Gaussian distribution with mean $k_0^+ = \mathcal{A}_0/N$, standard deviation $0.4k_0^+$, and a lower cutoff at $0.1k_0^+$. We set the rates in the motifs to the cis configuration ($a = 1, b = k_0^+$), and we introduced disorder in the probability of entering the decorations by choosing μ randomly from a uniform distribution $[0, 0.95\mu_{\max}]$, where

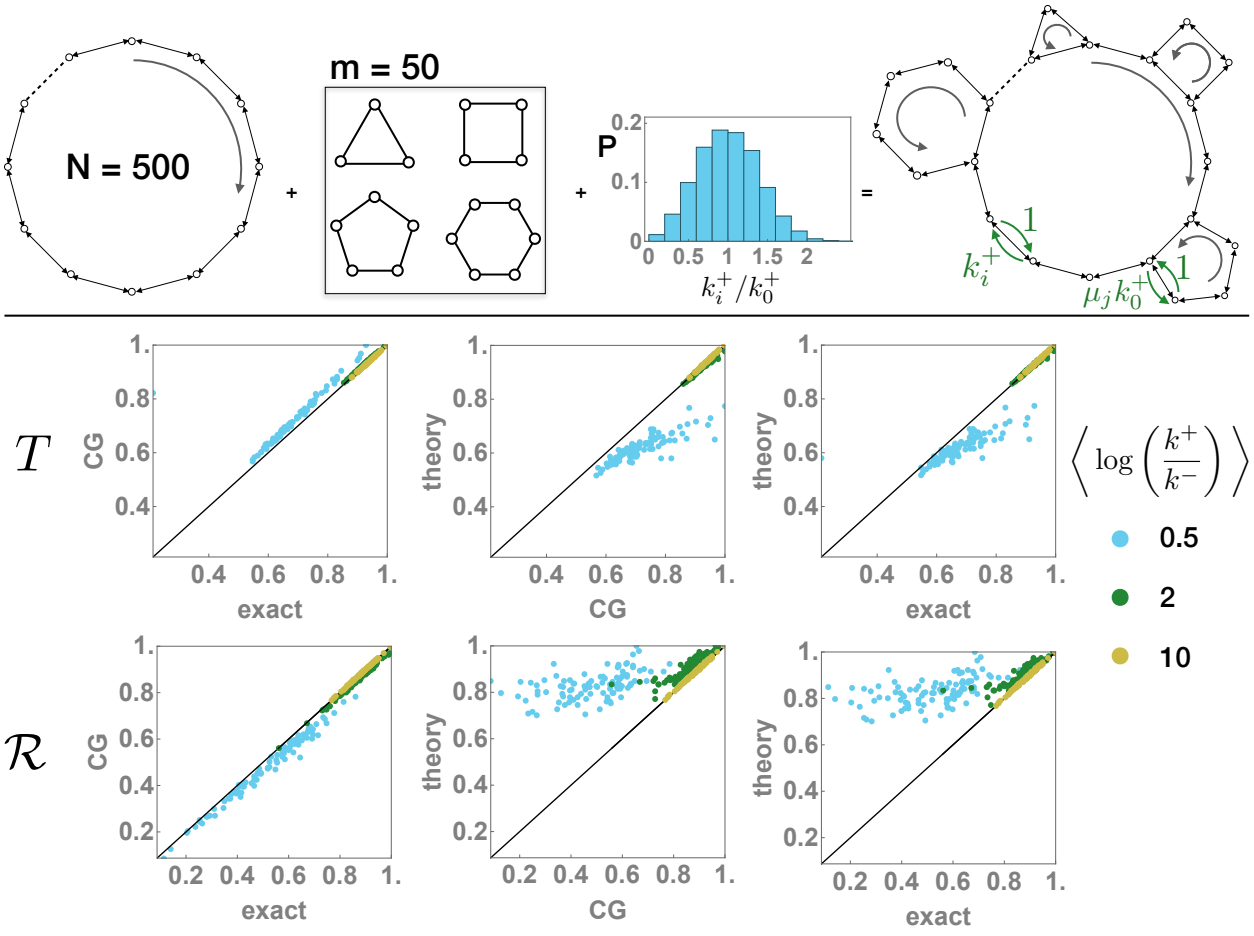

Figure 3.11: Period T and number of coherent oscillations $\mathcal{R}$ in networks with $N = 500$ states in the main cycle and $m = 50$ decorations. Here, disorder in the rates of the main cycle as well as disorder in the topology of the network are considered. The shapes and locations of the decorations as well as many of the rates are randomly generated as described in the text. Each point in the scatter plots represents a specific realization of quenched disorder of shapes, locations, and rates. As $\mathcal{A}_0/N = \langle k^+/k^- \rangle$ increases, the exact, coarse-grained, and theory values converge. All values are normalized by the largest value in the data on each scatter plot so that data for different affinities can be shown on the same plot.

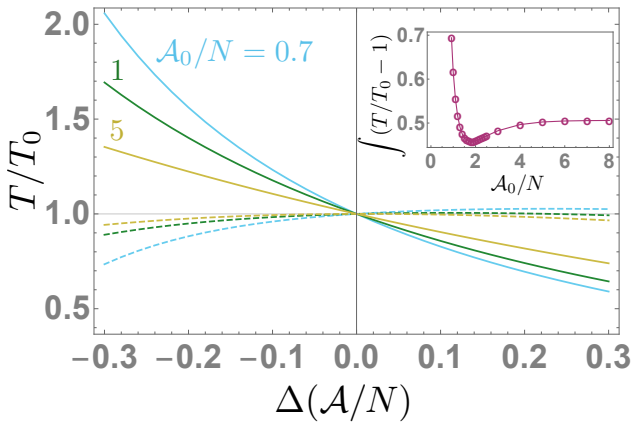

Figure 3.12: Compensating for changes in period by tuning the parameter μ as a function of $\Delta\mathcal{A}$ in a network with a large cycle of $N = 100$ states with $m = 20$ triangle decorations symmetrically distributed on the network, with the cis configuration ($a = k^- = 1, b = k^+ = \exp(\mathcal{A}/N) = \exp((\mathcal{A}_0 + \Delta\mathcal{A})/N)$). T_0 is the period at $\mathcal{A}_0/N$ and $\mu_0 = 0.5$. Solid lines show the period as the affinity is changed with $\mu = \mu_0$; dashed lines show the period when μ is changed as a function of the affinity: $\mu = \mu_0 + \Delta\mu$ with $\Delta\mu = \kappa_{comp}\Delta\mathcal{A}$, as described in the text. This linear compensation mechanism is effective over a wide range of affinities $\mathcal{A}_0$, compensating for changes in the period of ∼50%. Compensation occurs because by increasing (decreasing) μ the system is encouraged to spend more (less) time in the triangle decorations as the affinity is increased (decreased). Inset: The integrated deviation from perfect compensation ($T/T_0 = 1$) over the range $\Delta\mathcal{A} \in [-0.3, 0.3]$ as a function of the affinity in the unperturbed network. The mechanism is most effective when $\mathcal{A}_0/N \approx 2$ or greater.

$\mu_{\max}$ is the value of μ at which the effective rates in Table 3.1 diverge and depends on the size of the decoration. Once again, the agreement between both levels of approximation and exact results for T and $\mathcal{R}$ is excellent in the limit of high affinity ($\mathcal{A}_0/N = \exp(10)$), with very good agreement already at moderate values of the affinity ($\mathcal{A}_0/N = \exp(2)$).

3.4.4 Period compensation

The results of Fig. 3.11 show that the time scales of an oscillator with multiple cycles and randomly distributed rates do not depend on the arrangement of these rates and cycles. As a result, these time scales can be accurately predicted from our theory with information about the probability distributions of the rates and decorations, and, notably, without information about the spatial arrangement of the specific network. This extends the conclusions of

Section 3.3 to the case of network topology. The motivation for studying multiple cycles is that the small cycles can represent deviations from, or noise in, the oscillator's average limit cycle [104, 79]. The quenched disorder in Figs. 3.10 and 3.11 is meant to represent different realizations of the pathways sampled by the oscillator either over time or by multiple copies of the same oscillator (e.g., in different cells). In this context, our results show how an oscillator whose sampled paths and rates are fluctuating over time can use a high chemical affinity to maintain a predictable and robust period.

So far, we have considered disorder that kept the average value of the rates and affinity constant. We now briefly turn our attention to global fluctuations in the rates that result in a change in the affinity; for example, this could be due to a shift in the overall ATP to ADP ratio in a cell caused by a change in light levels or a change in temperature. Biochemical oscillators often have the ability to maintain a constant period in the presence of these changes, a feature known as input compensation [64, 44, 98]. For a given network topology and arrangement of relative rate magnitudes, changing the affinity effectively multiplies all of the rates by a constant, since $k^+/k^- \propto \exp(\mathcal{A}/N) = \exp(\mathcal{A}_0/N)\exp(\Delta\mathcal{A}/N)$, where now $\mathcal{A}_0$ refers to the reference or unperturbed value of the affinity in the main cycle of a decorated network. Any change in the affinity therefore results in a change in the period. However, if the rates or the decorations in the network are allowed to vary in a manner that is coupled to the change in affinity, the oscillator may be able to keep a constant period. Specifically, if the current increases on the network in response to an increase in the affinity, the system can increase the path length by increasing the probability of entering and remaining in decorations. This mechanism for compensation is a stochastic version of one that has previously been explored in deterministic limit cycles by several authors (e.g., [44, 54]): if an input changes the angular velocity of the limit cycle, the radius of the limit cycle must also change in response to the input in order to maintain a constant period.

We illustrate this compensation mechanism in Fig. 3.12. We choose the rates in the network as in Fig. 3.9: $a = k^- = 1$, $b = k^+ = \exp(\mathcal{A}/N)$. First, we hold μ fixed and

vary the affinity so that the rates become $b = k^+ = \exp((\mathcal{A}_0 + \Delta\mathcal{A})/N)$ and show that the period changes significantly with small changes in the affinity (solid lines in Fig. 3.12)—for instance, changing the affinity from $\mathcal{A}_0/N = 5$ to $\mathcal{A}/N = 5.3$ shortens the period by 25%. Then we allow the value of μ to be appropriately coupled to the affinity and show that these changes in the period can be compensated for, reducing the change to less than 5%. The parameter μ controls the probability of accessing the smaller secondary cycles. Hence, it effectively controls the size of sampled orbits in our networks.

In order to choose how μ should depend on the affinity, we consider the Taylor expansion of the period as a function of $\mathcal{A}$ and μ,

$$\begin{aligned} T(\mathcal{A},\mu) =& T(\mathcal{A}_0,\mu_0) \\ &+ \left(\frac{\partial T(\mathcal{A}_0,\mu_0)}{\partial \mu}\right)\Delta\mu + \left(\frac{\partial T(\mathcal{A}_0,\mu_0)}{\partial \mathcal{A}}\right)\Delta\mathcal{A} \\ &+ \mathcal{O}((\Delta\mu)^2, (\Delta\mathcal{A})^2, \Delta\mu\Delta\mathcal{A}) + \cdots . \end{aligned} \tag{3.83}$$

Perfect compensation then requires $T(\mathcal{A},\mu) = T(\mathcal{A}_0,\mu_0)$, or

$$0 = \left(\frac{\partial T(\mathcal{A}_0,\mu_0)}{\partial \mu}\right)\Delta\mu + \left(\frac{\partial T(\mathcal{A}_0,\mu_0)}{\partial \mathcal{A}}\right)\Delta\mathcal{A} + \cdots \tag{3.84}$$

for all $\Delta\mathcal{A}, \Delta\mu$. In general, this leads to a very complicated $\Delta\mu$ that is a function of $\Delta\mathcal{A}$ with as many parameters as the Taylor expansion has terms. However, we find numerically in Fig. 3.12 that over large changes in the period, T is in fact a linear function of $\Delta\mathcal{A}$ and $\Delta\mu$, so that we can achieve compensation just by setting

$$\Delta\mu = -\left[\left(\frac{\partial T(\mathcal{A}_0,\mu_0)}{\partial \mathcal{A}}\right) \Big/ \left(\frac{\partial T(\mathcal{A}_0,\mu_0)}{\partial \mu}\right)\right]\Delta\mathcal{A} \tag{3.85}$$

$$\equiv \kappa_{comp}\Delta\mathcal{A}. \tag{3.86}$$

In the inset in Fig. 3.12, we see that this "linear compensation" mechanism works best

above a minimum value of the affinity around $\mathcal{A}_0/N = 2$, indicating that a high chemical affinity can support simple mechanisms for compensation. Indeed, using a linear approximation of our theory in Eqs. 3.49 and 3.50, we find that as long as the effective rates in the coarse-grained link are proportional to k^+ (as they are in our case; see Table 3.1), all second-order and higher terms in Eq. 3.84 vanish at high affinity and for large main cycle size N. High affinity therefore makes it easy to design (or, in the context of a biochemical oscillator, to evolve) a network of this kind with compensation, since only one parameter needs to be tuned, which is easily computed from the unperturbed $(\mu_0, \mathcal{A}_0)$ network.

Here we have illustrated compensation using μ for simplicity since it is a continuous variable. However, the number and size of the decorations could also be used to adjust the period, since these all affect either the path length of an oscillation or the amount of time the system spends effectuating futile cycles in decorations.

3.4.5 Conclusions and future directions

In this section we presented an analytical theory for computing the period of oscillations in Markov models consisting of one large cycle of size N decorated with smaller secondary cycles that are driven out of equilibrium by an affinity $\mathcal{A}$ (Fig. 3.1). First, we mapped the decorations onto single links that retain the mean and variance of the first passage time across the decoration. Performing this procedure for all of the decorations in the network yields a single-cycle network, for which we have previously derived analytical expressions for the period and coherence of oscillations. Importantly, these analytical expressions take as inputs the rates along each edge in the network but do not know about their relative placement. Numerical calculations of the period at high affinity agree well with this analytical prediction (Figs. 3.9–3.11). Our main result is that the ability of our theory to accurately predict the period and coherence implies that high energy dissipation makes these observables insensitive to many parameters—specifically, the arrangement of the cycles and rates in the network. As a result, oscillators represented by the models studied here can have time scales that are

robust to fluctuations in rates and topology. Finally, we showed how multi-cycle network topologies can also be exploited to achieve compensation to changes in affinity by tuning the amount of time that the system spends in the decorations. It will be interesting to further characterize networks that have compensation. For instance, it is intuitively clear that systems must contain some futile cycles or other alternate pathways to be able to compensate for changes in the current, suggesting that compensation over a broader parameter regime has costs in terms of both energy and network complexity. Understanding this cost-function trade-off of period compensation in biochemical oscillators would add to our understanding of these trade-offs in biology, where they have been studied in the context of many areas, from sensing [83] to DNA copying [57].

3.5 Conclusions and future directions

In this chapter, we explored how the dynamics of minimal cyclic Markov models with disorder in the hopping rates and connectivity can be robust to this disorder. These models are intended to represent biochemical oscillators such as the KaiC oscillator, which underlies the circadian rhythm of the cyanobacterium *S. elongatus*, insofar as the models capture the two basic features of the oscillators: cycling and stochasticity. We derived an analytical expression for the largest nonzero eigenvalues of the transition rate matrices that govern the dynamics of these oscillators. We showed that while in general the eigenvalue depends on all of the rates in the matrices and on their positions and any correlations between them, these correlations vanish in the limit of a large ratio of forward to reverse rates, or high affinity. Our result is in line with results on random walks in disordered environments, but whereas analytical expressions in those cases require the assumption that rates are uncorrelated, here we show how a high affinity can be used to make the rates uncorrelated. Because the eigenvalue that we computed encodes the period of global oscillations and the uncertainty in the period of these models, these results show that the period of a network that has a high chemical affinity is also more robust to fluctuations that affect the rates in the network.

Insofar as our model is a good representation of a biochemical oscillator, this implies that oscillators can consume more ATP in order to achieve more precise timing in fluctuating environments.

However, our results also show that a fairly moderate affinity—$\mathcal{A}/N$ on the order of 1—is sufficient to achieve this benefit. Other results from stochastic thermodynamics also show decreasing returns in terms of precision above a certain rate of energy consumption in simple models of biochemical oscillators [6, 92]. Comparatively, KaiC burns a lot of energy per cycle—on the order of $\mathcal{A}/N = 10$ [136]. There are many functions of KaiC that require energy and that these models leave out or incorporate in an ad hoc manner. For example, other mechanisms for achieving time precision (such as synchronization of a population of KaiC oscillators [156, 56]) that are seen in vitro in reconstituted Kai systems or in vivo functions like communicating temporal information downstream to regulate gene expression. While the results from minimal models are useful insofar as they provide physical, and therefore typically universal, energy-function trade-offs, it would be useful to understand how they are connected to detailed simulation models of KaiC that quantitatively reproduce experimental results [97, 56]. Although these are kinetic Monte Carlo simulations and therefore are themselves Markov models, the number of unique states of the system is in the millions and therefore the transition rate matrices are not easy to interpret or even write down.

3.5.1 Dimensional reduction for generating realistic minimal models of biochemical oscillators

In order to better understand what kinds of network topologies and rates can support the various features such as compensation, synchronization, etc. that we see in KaiC, and therefore what kind of minimal networks we should focus analytical efforts on, we would like to exploit the detailed and realistic numerical models of KaiC that have been developed over the past decade to take a data-centered approach to writing down Markov models that represent the full dynamics of this oscillator. By coming up with a systematic way to do this, we

could understand how different conditions (such as the energy available via ATP consumption [118]) affect the underlying network. Since there are many complex cyclic processes in biology (such as cell cycles) that we might wish to represent as Markov models in order to identify human-interpretable universal features, a framework for mapping high-dimensional continuous or nearly continuous simulations to discrete networks with a relatively small number of states would be broadly useful in biophysics and other areas dealing with complex systems.

One possible approach would be similar in spirit to Markov state modeling (MSM), which is typically used as a dimensional reduction technique for simulations of proteins and other large molecules [101]. It is assumed that proteins exist in some small number of metastable states—for instance, folded and unfolded—with slow transitions between these states, while within the metastable states fluctuations are very fast and are assumed not to be important for the purposes of the study. MSM is a collection of techniques used to exploit this separation of time scales to build coarse-grained models that represent the system as a series of these discrete metastable states, with hopping rates between them that preserve the long-time dynamics of the protein. The basic method is to discretize the high-dimensional space of the simulation (the dimensions are atom coordinates, dihedral angles, etc., not spatial dimensions) build a matrix of transition rates between the N resulting microstates, diagonalize the matrix, and then build a matrix of dimension $n \ll N$ that approximates as closely as possible the top n eigenvalues of the original matrix, which represent the slowest relaxation time scales and therefore the transitions between metastable states.

The popularity of KaiC as an experimental model system has led to the development of a very detailed kinetic Monte Carlo simulation model of the system [97]. This model represents, at a detailed level, the states of each KaiC monomer and hexamer in a population of KaiA, B, and C, and it is able to quantitatively reproduce many of the experimental observations from in vitro studies of the clock. This numerical model of KaiC provides us with the starting material to develop a coarse-grained Markov model representation of the system. While

conceptually similar to MSM for proteins, there are two important differences: first, rather than developing a coarse-grained model of a physical object such as a protein, we would like a model of the collective oscillations of a population of objects, and second, the oscillator is a nonequilibrium system.

Despite the wide popularity of MSM, with very few exceptions MSM techniques are designed for equilibrium systems and specifically take advantage of detailed balance and the real eigenvalues and eigenvectors of the transition rate matrices of these systems. Out of equilibrium, detailed balance is broken, and in systems with oscillations, the eigenvalues are complex. One technique recently proposed in the literature for MSM of nonequilibrium systems is the generalized Perron cluster-cluster algorithm (G-PCCA) [113, 112]. This algorithm uses an alternative matrix decomposition called the real Schur decomposition in place of eigendecomposition, and then uses an algorithm called PCCA+ [14] to perform the coarse-graining. The method has been demonstrated on molecular dynamics simulations of a peptide in an oscillating magnetic field [113] and on simulations of a system of ODEs called the repressilator [112], which is a simple model of protein expression oscillations. In the former case, the system was only sampled stroboscopically, so that there are no global oscillations in the reduced model. In the latter, the system has three fairly distinct macrostates with a high concentration of protein A, B, or C and a low concentration of the two others. Systems such as KaiC present a different challenge, since a population of KaiC oscillators "ticks" between nearly continuous phosphorylation levels. It is therefore unclear whether this system has the separation of time scales and near-block-diagonal form of the transition rate matrix that are the mathematical basis of MSM techniques, including G-PCCA [115]. In these cases the optimal number of macrostates is ambiguous, and the G-PCCA algorithm may not converge to a physically reasonable answer (for instance, the coarse-grained matrix can have negative rates). In order to overcome these challenges, a detailed study of the behavior of the G-PCCA algorithm on several minimal models with these same features is necessary. To this end, we have begun to look at how the algorithm performs as a function

of the separation of time scales in the full dynamics and of the amount of sampling used to build the transition rate matrix between macrostates. Once thoroughly characterized, G-PCCA could provide a framework for creating analytically tractable and interpretable models of cyclic processes in biology and elsewhere.

Appendices

The derivations in this section are adapted from the derivations by Laura Tociu in our coauthored paper, Ref. 29.

A1 Proofs and calculations for analytical results in Section 2.3

A1.1 Proof that $\langle \mathbf{F}^2 \rangle = \langle \mathbf{F}^2 \rangle_0$ for a liquid in equilibrium

Assuming we have fixed a particle with position $\mathbf{r}_1$ at the origin, by Taylor expanding the total force $\mathbf{F}_1$ acting on this particle term-by-term we get the equation below in the x direction and an analogous equation in the other directions:

$$F_{1,x}(t+\Delta t) = F_{1,x}(t) + \sum_{i=1}^{N} \frac{\partial F_{1,x}(t)}{\partial x_i} \dot{x}_i(t)\Delta t + \frac{1}{2}\sum_{i=1}^{N}\sum_{j=1}^{N} \frac{\partial^2 F_{1,x}(t)}{\partial x_i \partial x_j} \dot{x}_i(t)\dot{x}_j(t)(\Delta t)^2 + O(\Delta t^3) \tag{87}$$

Taking the dot product with the noise (in 2D to exemplify, but easily generalizable to other dimensions) we obtain:

$$\lim_{\Delta t \to 0} \langle \boldsymbol{\eta}_1(t) \cdot \mathbf{F}_1(t+\Delta t) \rangle = \lim_{\Delta t \to 0} \big\langle (\eta_{1,x}(t), \eta_{1,y}(t)) \cdot (F_{1,x}(t+\Delta t), F_{1,y}(t+\Delta t)) \big\rangle \tag{88}$$

$$= \lim_{\Delta t \to 0} \Big(\big\langle \eta_{1,x}(t) F_{1,x}(t) + \eta_{1,y}(t) F_{1,y}(t) \big\rangle + \sum_{i=1}^{N} \left\langle \eta_{1,x}(t) \frac{\partial F_{1,x}(t)}{\partial x_i} \dot{x}_i(t) + \eta_{1,y}(t) \frac{\partial F_{1,y}(t)}{\partial y_i} \dot{y}_i(t) \right\rangle \Delta t + O(\Delta t^2) \Big). \tag{89}$$

Terms of order $(\Delta t)^2$ or higher in Eq. 89 vanish as Δt goes to 0. Using the Langevin equation $\dot{x}_i(t) = \frac{1}{\gamma}F_{i,x}(t) + \eta_{i,x}(t)$ and averaging over particles, it follows that:

$$\begin{aligned}
\langle \mathbf{F}^2 \rangle_0 &\equiv -\frac{\gamma}{2}\lim_{\Delta t\to 0}\langle \boldsymbol{\eta}(t)\cdot\mathbf{F}(t+\Delta t)\rangle \\
&= -\frac{\gamma}{2}\lim_{\Delta t\to 0}\left\langle \frac{\partial F_{1,x}(t)}{\partial x_1}\eta_{1,x}^2(t) + \frac{\partial F_{1,y}(t)}{\partial y_1}\eta_{1,y}^2(t)\right\rangle \Delta t \qquad (90)\\
&= \frac{\gamma}{2}\lim_{\Delta t\to 0}\left(\left\langle \frac{\partial^2 U}{\partial x_1^2}\right\rangle \frac{\langle dW_x^2\rangle}{\Delta t} + \left\langle \frac{\partial^2 U}{\partial y_1^2}\right\rangle \frac{\langle dW_y^2\rangle}{\Delta t}\right) \qquad (91)\\
&= K_B T\left\langle \boldsymbol{\nabla}_1^2 U\right\rangle \qquad (92)\\
&= K_B T\rho\int \boldsymbol{\nabla}^2 u(\mathbf{r})g(\mathbf{r})d\mathbf{r} \qquad (93)
\end{aligned}$$

where we have defined $\langle dW_x^2\rangle \equiv \langle(\eta_x\Delta t)^2\rangle = 2D_0\Delta t = \frac{2K_BT}{\gamma}\Delta t$.

Let us now expand the term $\left\langle \mathbf{F}^2\right\rangle$. Again by focusing on a single particle with position $\mathbf{r}_1$ fixed at the origin and doing similar manipulations we obtain:

$$\begin{aligned}
\left\langle \mathbf{F}^2\right\rangle &= \left\langle (\boldsymbol{\nabla}_1 U(\mathbf{r}))^2\right\rangle \\
&= \rho\int (\boldsymbol{\nabla}u(\mathbf{r}))^2 g(\mathbf{r})d\mathbf{r} \\
&\quad + \rho^2\int\int \boldsymbol{\nabla}u(\mathbf{r})\cdot\boldsymbol{\nabla}u(\mathbf{r}')g_3(\mathbf{r},\mathbf{r}')d\mathbf{r}d\mathbf{r}' \qquad (94)
\end{aligned}$$

To aid us in evaluating Eq. 94, we assume the system is in equilibrium with a Boltzmann distributed steady state, and use the Yvon-Born-Green hierarchy [116]:

$$g(\mathbf{r})\boldsymbol{\nabla}u(\mathbf{r}) = -K_BT\boldsymbol{\nabla}g(\mathbf{r}) - \rho\int d\mathbf{r}'\boldsymbol{\nabla}u(\mathbf{r}')g_3(\mathbf{r},\mathbf{r}'). \qquad (95)$$

Plugging this expression into Eq. 94 cancels the term containing the three-point correlation function, yielding:

$$\left\langle \mathbf{F}^2\right\rangle = -K_BT\rho\int \boldsymbol{\nabla}u(\mathbf{r})\cdot\boldsymbol{\nabla}g(\mathbf{r})d\mathbf{r}. \qquad (96)$$

Integrating by parts and setting boundary terms to zero gives the final expression for $\langle \mathbf{F}^2 \rangle$:

$$\left\langle \mathbf{F}^2 \right\rangle = K_B T \rho \int \boldsymbol{\nabla}^2 u(\mathbf{r}) g(\mathbf{r}) d\mathbf{r}. \tag{97}$$

The expression is equal to Eq. 93, proving that $\langle \mathbf{F}^2 \rangle = \langle \mathbf{F}^2 \rangle_0$ at equilibrium.

A1.2 Expression for diffusion from perturbation theory

The diffusion can be expressed in terms of force-force and noise-force correlations as:

$$D - D_0 = \frac{1}{d} \int_0^\infty \left[\left\langle \frac{\mathbf{F}(0) \cdot \mathbf{F}(t)}{\gamma^2} \right\rangle + \left\langle \frac{\boldsymbol{\eta}(0) \cdot \mathbf{F}(t)}{\gamma} \right\rangle \right] dt. \tag{98}$$

In order to compute the integrals over the force-force and noise-force correlations, we will fix the initial positions of the particle at some position $\mathbf{r}$, and consider a trajectory due to one realization of the noise. We will then integrate over all possible initial positions and all possible realizations of the noise. For instance, for the force-force correlation, this is expressed mathematically as:

$$\int_0^\infty \langle \tilde{\mathbf{F}}(0) \cdot \tilde{\mathbf{F}}(t) \rangle dt = h^2 \int_0^\infty \langle \tilde{\mathbf{F}}(0) \cdot \tilde{\mathbf{F}}(t) \rangle dt = h^2 \int_0^\infty dt \int d\mathbf{r} \frac{P(\mathbf{r})}{Z} \int \frac{d\mathbf{q}}{(2\pi)^d} \int \frac{d\mathbf{q}'}{(2\pi)^d}. \tag{99}$$

In order to compute this integral, we need an expression for $P(\mathbf{r})$, the distribution of initial positions. To calculate it, we start from the overdamped Langevin equation:

$$\dot{\mathbf{r}} = \frac{h}{\gamma} \tilde{\mathbf{F}}(\mathbf{r}) + \tilde{\boldsymbol{\eta}}(t) = \frac{h}{\gamma} \left(\tilde{\mathbf{F}}_c(\mathbf{r}) + \mathrm{Pe} \tilde{\mathbf{F}}_d(\mathbf{r}) \right) + \tilde{\boldsymbol{\eta}}(t) \tag{100}$$

where $\tilde{\mathbf{F}}_c(\mathbf{r}) = -\nabla \tilde{U}(\mathbf{r})$ is the conservative force and $\tilde{\mathbf{F}}_d(\mathbf{r}) = \nabla \times \tilde{\mathbf{A}}(\mathbf{r})$ the dissipative force. $\tilde{U}(\mathbf{r})$ obeys $\int \tilde{U}(\mathbf{r}) d\mathbf{r} = 0$, and we also require $\int \tilde{\mathbf{F}}(\mathbf{r}) d\mathbf{r} = 0$. In this section we will consider only averages of the various force correlations over the noise. The final averaging over the distribution from which we sample the forces is implied. We will be working in the limit

$h \ll \mathrm{Pe} \ll 1$ and we will keep only terms of order $\epsilon_1^2, \epsilon_2^2$ and $\epsilon_1\epsilon_2$, where $\epsilon_1 = h$ and $\epsilon_2 = h\mathrm{Pe}$. The probability distribution for this system obeys the following Fokker-Planck equation:

$$\frac{\partial P}{\partial t} = -h\vec{\nabla}\cdot\left[\tilde{\mathbf{F}}_c P\right] + D\nabla^2 P - h\mathrm{Pe}\vec{\nabla}\cdot\left[\tilde{\mathbf{F}}_d P\right] \equiv W_0 P - h\mathrm{Pe}\vec{\nabla}\cdot\left[\tilde{\mathbf{F}}_d P\right] . \tag{101}$$

When $\mathrm{Pe} = 0$, the system is in equilibrium and Eq. 101 is solved by the Boltzmann distribution $P_0 = \dfrac{e^{-\beta h\tilde{U}(\mathbf{r})}}{Z}$, where Z is the partition function. We construct a perturbation theory in Pe by considering the latter term in Eq. 101 as a perturbation to the equilibrium distribution. Following standard perturbation theory, the first correction to the equilibrium distribution is then given by:

$$P_1 = \mathrm{Pe}\sum_i \frac{|u_i\rangle\langle v_i|\tilde{\mathbf{F}}_d\cdot\nabla|P_0\rangle}{\lambda_i} \tag{102}$$

where the vectors $|u_i\rangle$ and $\langle v_i|$ are the right and left eigenvectors of W_0, respectively, and λ_i are the eigenvalues. The total probability for our system is then given by:

$$P(\mathbf{r}) = \frac{e^{-\beta h\tilde{U}(\mathbf{r})}}{Z} + h\mathrm{Pe}\sum_i \frac{|u_i\rangle\langle v_i|\tilde{\mathbf{F}}_d\cdot\nabla|P_0\rangle}{\lambda_i}. \tag{103}$$

To proceed with evaluating the expression for the diffusion coefficient perturbatively, we will consider terms of order up to $\epsilon_{1,2}^2$. We note that the correction to the Boltzmann factor in Eq. 103 scales like $h^2\mathrm{Pe}$, and can hence be ignored in the remainder of our theory since it will only appear in contexts where it is multiplied by a conservative force, leading to $h^3\mathrm{Pe}$ scaling. In other words, we will only need at most the equilibrium term P_0 in the following calculations. We are now in a position to compute Eq. 99:

$$h^2\int_0^\infty \langle\tilde{\mathbf{F}}(0)\cdot\tilde{\mathbf{F}}(t)\rangle dt = h^2\int_0^\infty dt\int d\mathbf{r}\frac{P(\mathbf{r})}{Z}\int\frac{d\mathbf{q}}{(2\pi)^d}\int\frac{d\mathbf{q}'}{(2\pi)^d} \tag{104}$$
$$\left(\tilde{\mathbf{F}}(\mathbf{q})\cdot\tilde{\mathbf{F}}(\mathbf{q}')e^{i(\mathbf{q}+\mathbf{q}')\cdot\mathbf{r}}\langle e^{\int_0^t i\mathbf{q}'\cdot\tilde{\boldsymbol{\eta}}(t')dt' + h/\gamma\int_0^t i\mathbf{q}'\cdot\tilde{\mathbf{F}}(t')dt'}\rangle\right)$$

Keeping terms to order $\epsilon_{1,2}^2$ we have:

$$\begin{aligned}
h^2\int_0^\infty \langle \tilde{\mathbf{F}}(0)\cdot\tilde{\mathbf{F}}(t)\rangle dt &\approx h^2\frac{1}{V}\int\frac{d\mathbf{q}}{(2\pi)^d}\int\frac{d\mathbf{q}'}{(2\pi)^d}\tilde{\mathbf{F}}(\mathbf{q})\cdot\tilde{\mathbf{F}}(\mathbf{q}')\delta(\mathbf{q}+\mathbf{q}')\int_0^\infty \langle e^{\int_0^t i\mathbf{q}'\cdot\tilde{\boldsymbol{\eta}}(t')dt'}\rangle dt \\
&= h^2\frac{1}{V}\int\frac{d\mathbf{q}}{(2\pi)^d}\tilde{\mathbf{F}}(\mathbf{q})\cdot\tilde{\mathbf{F}}(-\mathbf{q})\int_0^\infty e^{-|\mathbf{q}|^2D_0t}dt \\
&= h^2\frac{1}{D_0V}\int\frac{d\mathbf{q}}{(2\pi)^d}\frac{1}{|\mathbf{q}|^2}\tilde{\mathbf{F}}(\mathbf{q})\cdot\tilde{\mathbf{F}}(-\mathbf{q}) \\
&= h^2\frac{1}{D_0V}\int\frac{d\mathbf{q}}{(2\pi)^d}\frac{1}{|\mathbf{q}|^2} \qquad (105)\\
&\qquad \Big(\tilde{\mathbf{F}}_c(\mathbf{q})\cdot\tilde{\mathbf{F}}_c(-\mathbf{q}) + 2\mathrm{Pe}\tilde{\mathbf{F}}_c(\mathbf{q})\cdot\tilde{\mathbf{F}}_d(-\mathbf{q}) + \mathrm{Pe}^2\tilde{\mathbf{F}}_d(\mathbf{q})\cdot\tilde{\mathbf{F}}_d(-\mathbf{q})\Big)
\end{aligned}$$

The noise-force correlation term is given by:

$$\begin{aligned}
h\int_0^\infty dt\langle\tilde{\boldsymbol{\eta}}(0)\cdot\tilde{\mathbf{F}}(t)\rangle &= h\int_0^\infty dt\int d\mathbf{r}\frac{P(\mathbf{r})}{Z}\int\frac{d\mathbf{q}}{(2\pi)^d} \\
&\qquad \Big(\langle\tilde{\boldsymbol{\eta}}(0)\cdot\tilde{\mathbf{F}}(\mathbf{q})e^{i\mathbf{q}\cdot\mathbf{r}}e^{\int_0^t i\mathbf{q}\cdot\tilde{\boldsymbol{\eta}}(t')dt'+h/\gamma\int_0^t i\mathbf{q}\cdot\tilde{\mathbf{F}}(t')dt'}\rangle\Big) \qquad (106)
\end{aligned}$$

The first term of order $\epsilon_{1,2}^2$, which we call T_1, comes from $P(\mathbf{r})$, which we expand in terms of h:

$$\begin{aligned}
T_1 &= \frac{h^2}{V}\int d\mathbf{r}(-\beta\tilde{U}(\mathbf{r}))\int\frac{d\mathbf{q}}{(2\pi)^d}e^{i\mathbf{q}\cdot\mathbf{r}}\int_0^\infty\langle\tilde{\boldsymbol{\eta}}(0)\cdot\tilde{\mathbf{F}}(\mathbf{q})e^{\int_0^t i\mathbf{q}\cdot\tilde{\boldsymbol{\eta}}(t')dt'}\rangle dt \\
&= \frac{-\beta h^2}{V}\int\frac{d\mathbf{q}}{(2\pi)^d}\int\frac{d\mathbf{q}'}{(2\pi)^d}\tilde{U}(\mathbf{q}')\delta(\mathbf{q}+\mathbf{q}')\int_0^\infty\langle\tilde{\boldsymbol{\eta}}(0)\cdot\tilde{\mathbf{F}}(\mathbf{q})e^{\int_0^{\Delta t} i\mathbf{q}\cdot\tilde{\boldsymbol{\eta}}(t')dt'}e^{\int_{\Delta t}^t i\mathbf{q}\cdot\tilde{\boldsymbol{\eta}}(t')dt'}\rangle dt \\
&= \frac{-2D_0\beta h^2}{V}\int\frac{d\mathbf{q}}{(2\pi)^d}\tilde{U}(-\mathbf{q})i\mathbf{q}\cdot\tilde{\mathbf{F}}(\mathbf{q})\int_0^\infty e^{-|\mathbf{q}|^2D_0t}dt \\
&= \frac{-2\beta h}{V}\int\frac{d\mathbf{q}}{(2\pi)^d}\frac{1}{|\mathbf{q}|^2}\tilde{\mathbf{F}}_c(-\mathbf{q})\cdot\tilde{\mathbf{F}}(\mathbf{q}) \\
&= -\frac{2\beta h^2}{V}\int\frac{d\mathbf{q}}{(2\pi)^d}\frac{1}{|\mathbf{q}|^{\mathbf{2}}}\Big(\tilde{\mathbf{F}}_c(-\mathbf{q})\cdot\tilde{\mathbf{F}}_c(\mathbf{q}) + \mathrm{Pe}\tilde{\mathbf{F}}_c(-\mathbf{q})\cdot\tilde{\mathbf{F}}_d(\mathbf{q})\Big) \qquad (107)
\end{aligned}$$

The second term quadratic in $\epsilon_{1,2}$, T_2, comes from the force present in the exponential in Eq. 106. Ignoring constants, this term can be written as:

$$\begin{aligned}
T_2 \propto & h^2 \int d\mathbf{r} \int \frac{d\mathbf{q}}{(2\pi)^d} \int \frac{d\mathbf{q}'}{(2\pi)^d} e^{i(\mathbf{q}+\mathbf{q}')\cdot\mathbf{r}} i\mathbf{q}\cdot\tilde{\mathbf{F}}(\mathbf{q}') \\
& \left(\int_0^\infty dt \int_0^t dt' \langle \tilde{\mathbf{F}}(\mathbf{q})\cdot\tilde{\boldsymbol{\eta}}(0) e^{\int_0^t i\mathbf{q}\cdot\tilde{\boldsymbol{\eta}}(\tau)d\tau} e^{\int_0^{t'} i\mathbf{q}'\cdot\tilde{\boldsymbol{\eta}}(\tau)d\tau} \rangle \right) \\
= & h^2 \int \frac{d\mathbf{q}}{(2\pi)^d} i\mathbf{q}\cdot\tilde{\mathbf{F}}(-\mathbf{q}) \int_0^\infty dt \int_0^t dt' \langle \tilde{\mathbf{F}}(\mathbf{q})\cdot\tilde{\boldsymbol{\eta}}(0) e^{\int_{t'}^t i\mathbf{q}\cdot\tilde{\boldsymbol{\eta}}(\tau)d\tau} \rangle \\
= & h^2 \lim_{\Delta t\to 0} \int \frac{d\mathbf{q}}{(2\pi)^d} i\mathbf{q}\cdot\tilde{\mathbf{F}}(-\mathbf{q}) \int_0^\infty dt \int_0^{\Delta t} dt' \langle \tilde{\mathbf{F}}(\mathbf{q})\cdot\tilde{\boldsymbol{\eta}}(0) e^{\int_{t'}^t i\mathbf{q}\cdot\tilde{\boldsymbol{\eta}}(\tau)d\tau} \rangle \\
= & h^2 \lim_{\Delta t\to 0} \int \frac{d\mathbf{q}}{(2\pi)^d} i\mathbf{q}\cdot\tilde{\mathbf{F}}(-\mathbf{q}) \int_0^\infty dt \langle \tilde{\mathbf{F}}(\mathbf{q})\cdot\tilde{\boldsymbol{\eta}}(0) e^{\int_0^t i\mathbf{q}\cdot\tilde{\boldsymbol{\eta}}(\tau)d\tau} \rangle \Delta t \\
= & 2h^2 \lim_{\Delta t\to 0} \int \frac{d\mathbf{q}}{(2\pi)^d} i\mathbf{q}\cdot\tilde{\mathbf{F}}(-\mathbf{q}) i\mathbf{q}\cdot\tilde{\mathbf{F}}(\mathbf{q}) \frac{1}{|\mathbf{q}|^2} \Delta t \\
= & 0
\end{aligned} \tag{108}$$

The term linear in $\epsilon_{1,2}$, T_3, can be computed in a similar way:

$$\begin{aligned}
T_3 \propto & h \int_0^\infty dt \int d\mathbf{r} \int \frac{d\mathbf{q}}{(2\pi)^d} \langle \tilde{\boldsymbol{\eta}}(0)\cdot\tilde{\mathbf{F}}(\mathbf{q}) e^{i\mathbf{q}\cdot\mathbf{r}} e^{\int_0^t i\mathbf{q}\cdot\tilde{\boldsymbol{\eta}}(t')dt'} \rangle \\
\propto & h \int d\mathbf{r} \int \frac{d\mathbf{q}}{(2\pi)^d} \frac{1}{|\mathbf{q}|^{\mathbf{2}}} e^{i\mathbf{q}\cdot\mathbf{r}} i\mathbf{q}\cdot\left(\tilde{\mathbf{F}}_c(\mathbf{q}) + \mathrm{Pe}\tilde{\mathbf{F}}_{\mathbf{d}}(\mathbf{q}) \right) \\
= & h \left(\int \tilde{U}(\mathbf{r}) d\mathbf{r} + \mathrm{Pe} \int \frac{d\mathbf{q}}{(2\pi)^d} \frac{1}{|\mathbf{q}|^{\mathbf{2}}} i\mathbf{q}\cdot\tilde{\mathbf{F}}_{\mathbf{d}}(\mathbf{q}) \right) \\
= & h \left(\int \tilde{U}(\mathbf{r}) d\mathbf{r} + \mathrm{Pe} \int \frac{d\mathbf{q}}{(2\pi)^d} \frac{1}{|\mathbf{q}|^{\mathbf{2}}} i\mathbf{q}\cdot i\mathbf{q}\times\tilde{\mathbf{A}}(\mathbf{q}) \right) \\
= & h \left(\int \tilde{U}(\mathbf{r}) d\mathbf{r} + \mathrm{Pe} \int \frac{d\mathbf{q}}{(2\pi)^d} \frac{1}{|\mathbf{q}|^{\mathbf{2}}} i\mathbf{q}\times i\mathbf{q}\cdot\tilde{\mathbf{A}}(\mathbf{q}) \right) \\
= & 0
\end{aligned} \tag{109}$$

Plugging Eq. 105 and Eq. 107 into Eq. 98, and using the fact that $\tilde{\mathbf{F}}_c(\mathbf{q}) = -i\mathbf{q}\tilde{U}(\mathbf{q})$ yields the desired the expression for diffusion:

$$D - D_0 = \frac{D_0 h^2}{(K_B T)^2 dV}\left(\mathrm{Pe}^2 \int \frac{\tilde{\mathbf{F}}_d(\mathbf{q})\cdot\tilde{\mathbf{F}}_d(-\mathbf{q})}{|\mathbf{q}|^2} d\mathbf{q} - \int \tilde{U}^2(\mathbf{r}) d\mathbf{r}\right). \tag{110}$$

We can also use this perturbation theory to obtain expressions for the quantities $\langle\tilde{\mathbf{F}}^2\rangle$ and $\langle\tilde{\mathbf{F}}^2\rangle_0$:

$$\begin{aligned}
\langle\tilde{\mathbf{F}}^2\rangle &= \frac{h^2}{V}\int d\mathbf{r}\int\frac{d\mathbf{q}}{(2\pi)^d}\int\frac{d\mathbf{q}'}{(2\pi)^d}\tilde{\mathbf{F}}(\mathbf{q})\cdot\tilde{\mathbf{F}}(\mathbf{q}')e^{i(\mathbf{q}+\mathbf{q}')\cdot\mathbf{r}} \\
&= \frac{h^2}{V}\int\frac{d\mathbf{q}}{(2\pi)^d}\left(\tilde{\mathbf{F}}_c(\mathbf{q})\cdot\tilde{\mathbf{F}}_c(-\mathbf{q}) + 2\mathrm{Pe}\tilde{\mathbf{F}}_d(\mathbf{q})\cdot\tilde{\mathbf{F}}_{\mathbf{c}}(-\mathbf{q}) + \mathrm{Pe}^2\tilde{\mathbf{F}}_d(\mathbf{q})\cdot\tilde{\mathbf{F}}_d(-\mathbf{q})\right) \qquad (111) \\
\langle\tilde{\mathbf{F}}^2\rangle_0 &= \frac{h^2}{V}\frac{\beta\gamma}{2}\int d\mathbf{r}\tilde{U}(\mathbf{r})\int\frac{d\mathbf{q}}{(2\pi)^d}e^{i\mathbf{q}\cdot\mathbf{r}}\langle e^{i\mathbf{q}\cdot\tilde{\boldsymbol{\eta}}(0)\Delta t}\tilde{\boldsymbol{\eta}}(0)\cdot\tilde{\mathbf{F}}(\mathbf{q})\rangle \\
&= \frac{h^2}{V}\beta\gamma D_0\int\frac{d\mathbf{q}}{(2\pi)^d}\int\frac{d\mathbf{q}'}{(2\pi)^d}e^{i(\mathbf{q}+\mathbf{q}')\cdot\mathbf{r}}i\tilde{\mathbf{q}}\cdot\tilde{\mathbf{F}}(\mathbf{q})\tilde{U}(\mathbf{q}') \\
&= \frac{h^2}{V}\int\frac{d\mathbf{q}}{(2\pi)^d}\tilde{\mathbf{F}}(\mathbf{q})\cdot\tilde{\mathbf{F}}_c(-\mathbf{q}) \\
&= \frac{h^2}{V}\int\frac{d\mathbf{q}}{(2\pi)^d}\left(\tilde{\mathbf{F}}_c(\mathbf{q})\cdot\tilde{\mathbf{F}}_c(-\mathbf{q}) + \mathrm{Pe}\tilde{\mathbf{F}}_d(\mathbf{q})\cdot\tilde{\mathbf{F}}_c(-\mathbf{q})\right) \qquad (112)
\end{aligned}$$

Subtracting Eq. 112 from Eq. 111 and using the fact that $\int\frac{d\mathbf{q}}{(2\pi)^d}\tilde{\mathbf{F}}_c(\mathbf{q})\cdot\tilde{\mathbf{F}}_d(-\mathbf{q})$ can be rewritten as $\int d\mathbf{r}\tilde{\mathbf{F}}_c(\mathbf{r})\cdot\boldsymbol{\nabla}\times\tilde{\mathbf{A}}(\mathbf{r}) = -\int\mathbf{dr}\tilde{\mathbf{A}}(\mathbf{r})\cdot\boldsymbol{\nabla}\times\tilde{\mathbf{F}}_{\mathbf{c}}(\mathbf{r}) = \mathbf{0}$ yields the relationship for entropy dissipation:

$$\begin{aligned}
\langle\tilde{\mathbf{F}}^2\rangle - \langle\tilde{\mathbf{F}}^2\rangle_0 &= \frac{h^2}{V}\int\frac{d\mathbf{q}}{(2\pi)^d}\left(\mathrm{Pe}\tilde{\mathbf{F}}_c(\mathbf{q})\cdot\tilde{\mathbf{F}}_d(-\mathbf{q}) + \mathrm{Pe}^2\tilde{\mathbf{F}}_d(\mathbf{q})\cdot\tilde{\mathbf{F}}_d(-\mathbf{q})\right) \qquad (113) \\
&= \frac{h^2}{V}\mathrm{Pe}^2\int\frac{d\mathbf{q}}{(2\pi)^d}\tilde{\mathbf{F}}_d(\mathbf{q})\cdot\tilde{\mathbf{F}}_d(-\mathbf{q}). \qquad (114)
\end{aligned}$$

When $\mathrm{Pe} = 0$, entropy production is zero and $\langle\tilde{\mathbf{F}}^2\rangle = \langle\tilde{\mathbf{F}}^2\rangle_0$.

A1.2.1 Comparing with expressions for the equilibrium diffusion from the literature

At equilibrium, our prediction for the diffusion coefficient is given by:

$$D/D_0 = 1 - \frac{h^2}{(K_B T)^2 dV} \int U^2(\mathbf{r}) d\mathbf{r} \tag{115}$$

where d is the dimension. Here, we compare our prediction to existing ones in the literature. In 1D the analytical expression for the diffusion of a tagged particle in a periodic potential is due to Lifson and Jackson and reads: $D/D_0 = 1/\left(\langle e^{-\beta U}\rangle \langle e^{\beta U}\rangle\right)$, where the expectation value is taken to mean $\langle f(x)\rangle = 1/L \int_0^L f(x)dx$ [76]. In our perturbation theory, this expression becomes, to order h^2:

$$\begin{aligned}
\frac{D}{D_0} &= \frac{1}{\int_0^L e^{-\beta h U(x)} dx \int_0^L e^{\beta h U(x')} dx'} && (116)\\
&= L^2 \times \\
&\left(L - h\beta \int_0^L U(x)dx + (h^2\beta^2/2) \int_0^L U^2(x)dx + \dots \right)^{-1} \\
&\left(L + h\beta \int_0^L U(x')dx' + (h^2\beta^2/2) \int_0^L U^2(x')dx' + \dots \right)^{-1} && (117)\\
&\approx \frac{1}{1 + \frac{h^2\beta^2}{L} \int_0^L U^2(x)dx} && (118)\\
&\approx 1 - \frac{h^2\beta^2}{L} \int_0^L U^2(x)dx && (119)
\end{aligned}$$

which is in agreement with our results. In 2D the corresponding formula $D/D_0 = 1/\langle e^{\beta U}\rangle$ is due to Dean et al. [26]. Expanding this expression to order h^2 and recognizing that

$\int_0^L \int_0^L U(x,y)dxdy = 0$, we have:

$$\frac{D}{D_0} = \frac{L^2}{\int_0^L \int_0^L e^{\beta h U(x,y)} dxdy} \tag{120}$$

$$= \frac{L^2}{\int_0^L \int_0^L \left(1 + h\beta U(x,y) + (h^2\beta^2/2)U^2(x,y) + \dots\right) dxdy} \tag{121}$$

$$\approx \frac{1}{1 + \frac{h^2\beta^2}{2L^2}\int_0^L \int_0^L U^2(x,y)dxdy} \tag{122}$$

$$\approx 1 - \frac{h^2\beta^2}{2L^2}\int_0^L \int_0^L U^2(x,y)dxdy. \tag{123}$$

This result is also in agreement with our prediction.

A1.2.2 Higher Order Terms in Expression for Diffusion

We now show that higher order terms in h do not diverge. Higher order terms of $\int_0^\infty \tilde{\mathbf{F}}(0) \cdot \tilde{\mathbf{F}}(t)dt$ not involving the corrections to the Boltzmann distribution (P_1, P_2, etc) can be expressed generally as:

$$H_{nm} \propto \frac{h^n}{(D_0)^{m-1}(2\pi)^{d(n-1)}} \times \tag{124}$$
$$\int d\mathbf{q}_2 \dots \int d\mathbf{q}_n \tilde{\mathbf{F}}\left(-\sum_{i=2}^{n} \mathbf{q}_i\right) \cdot \tilde{\mathbf{F}}(\mathbf{q}_2) \frac{i\mathbf{q}_2 \cdot \tilde{\mathbf{F}}(\mathbf{q}_3) \dots i\mathbf{q}_{m-1} \cdot \tilde{\mathbf{F}}(\mathbf{q}_m)\tilde{U}(\mathbf{q}_{m+1}) \dots \tilde{U}(\mathbf{q}_n)}{|\mathbf{q}_2|^2(|\mathbf{q}_2|^2 + |\mathbf{q}_3|^2) \dots (|\mathbf{q}_2|^2 + |\mathbf{q}_3|^2 + \dots + |\mathbf{q}_m|^2)}$$

where $n \geq 3$ is the power of h, and for each n terms with m $n \geq m \geq 2$ will show up from different parts of the expansion. This quantity scales with system size as $L^{(1-n)d+(2-m)+2(m-1)}$. The maximum scaling with system size is $L^{(1-n)d+n}$, occurring when $m = n$. For $d = 1$, higher order terms in n can diverge with system size. For $d = 2$, the scaling is L^{2-n}, which can diverge only for terms of order less than or equal to 2. (Therefore, as long as $\langle F \rangle = 0$ holds, then the quadratic terms are well-behaved as described in Sec.A1.2). For d=3, the scaling is L^{3-2n}, which can not diverge since $n \geq 2$.

The higher order terms in $\int_0^\infty \boldsymbol{\eta}(0) \cdot \tilde{\mathbf{F}}(t)dt$ not involving the corrections to the Boltzmann

distribution (P_1, P_2, etc) can also be conveniently expressed as:

$$H_{nm} \propto \frac{2h^n}{(D_0)^{m-1}(2\pi)^{d(n-1)}} \times \int d\mathbf{q}_1 \ldots \int d\mathbf{q}_{n-1} i\mathbf{q}_1 \cdot \tilde{\mathbf{F}}(\mathbf{q}_1) \frac{i\mathbf{q}_1 \cdot \tilde{\mathbf{F}}(\mathbf{q}_2) \ldots i\mathbf{q}_{m-1} \cdot \tilde{\mathbf{F}}(\mathbf{q}_m) \tilde{U}(\mathbf{q}_{m+1}) \ldots \tilde{U}\left(-\sum_{i=1}^{n-1} \mathbf{q}_i\right)}{|\mathbf{q}_1|^2 \left(|\mathbf{q}_1|^2 + |\mathbf{q}_2|^2\right) \ldots \left(|\mathbf{q}_1|^2 + |\mathbf{q}_2|^2 + \ldots + |\mathbf{q}_m|^2\right)} \quad (125)$$

where $n \geq 3$ and $n - 1 \geq m \geq 1$. Terms with $m = n$ in this case are zero.

This quantity scales with system size as $L^{(1-n)d+(-m)+2m}$. When $m = n - 1$, we obtain the maximum scaling with system size as $L^{(1-n)d+n-1}$ and thus the higher order terms cannot diverge.

There are also other higher order terms that are of the form $H_{nm}P_1$, $H_{nm}P_2$ and so on, where $P_{1,2,\ldots}$ are the corrections to the Bolztmann distribution. These terms do not diverge. Since the P_i will not introduce any terms with positive powers of L, these will also not diverge.

A2 Composition-dependent diffusion can lead to phase separation

We will start by showing that a simple coarse-graining of our many body system with 1/2 driven and 1/2 undriven particles can lead to phase separation. Namely, let us track a probe volume V_0 and define an order parameter $f = \frac{N_R - N_B}{N_0}$, where N_R and N_B are the numbers of red and blue particles, respectively, and $N_0 = \rho V_0$ is the average number of particles in the probe volume. We can coarse-grain the system by positing that the particles in this probe volume do not interact with each other in any way, but diffuse with a diffusion constant $D(f)$ which depends on the instantaneous composition f. Since the only time scale relevant to the system is related to this diffusion, we can expect that, for small deviations around

$f = 0$, the composition f obeys an equation of motion of the form:

$$\frac{df}{dt} = -\alpha D(f) f + \sqrt{\beta D(f)}\eta \tag{126}$$

where α and β are phenomenological constants, η is a white noise with unit variance and the expression is interpreted in the Itô sense. First, we will demonstrate how such an equation of motion can lead to instabilities, and second we will provide a framework for predicting the form of the parameters α and β.

By ignoring the linear part of the diffusion coefficient in the many-body system as a function of Pe, we can write $D(f) \equiv D_{eq} + (1 - f^2) b(\tau) \mathrm{Pe}^2$, to second order in the parameter f. This form satisfies the constraints that the diffusion increases quadratically with the driving forces, and decreases as we shift away from a mixed composition to a demixed composition of either just red or just blue particles. Plugging this form of $D(f)$ in Eq. 126 and solving the associated Fokker-Planck equation yields the solution:

$$P(f) = C_0 \frac{e^{-\frac{\alpha}{2\beta} f^2}}{D_{eq} + (1 - f^2) b(\tau) \mathrm{Pe}^2} \tag{127}$$

where C_0 is the normalization constant. Taylor expanding this expression, we obtain that $P(f)$ stops being peaked at $f = 0$ (and hence instabilities appear) whenever

$$\frac{\alpha}{2\beta} < \frac{b(\tau)\mathrm{Pe}^2}{D_{eq} + b(\tau)\mathrm{Pe}^2}. \tag{128}$$

This framework demonstrates that a composition-dependent diffusion can lead to phase separation.

We will now try to find the conditions for phase separation in our system by formally deriving an equation of motion for the variable $f = \dfrac{N_R - N_B}{N_0}$. We will compute the statistics of the variable Δf, the change of the composition in a small amount of time, given that the composition is f at $t = 0$ and the number of particles in the probe volume is fixed at

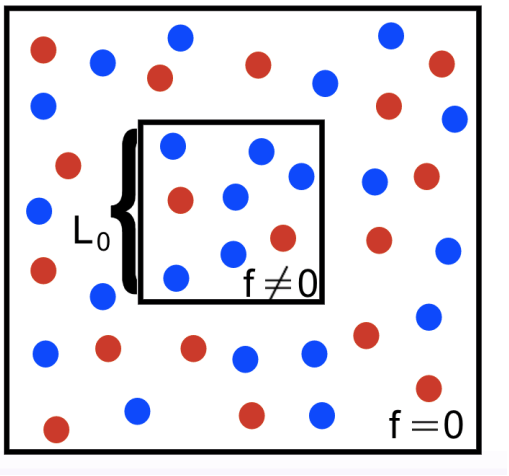

Figure A2.1: The setup of our composition calculations involves a small square probe volume of dimension L_0 with demixed composition ($f \neq 0$) in a mixed particle bath (f=0).

$N_0 = \rho L_0^2$. We imagine the probe volume exchanges particles with a bath that has a mixed composition ($f = 0$) (Fig. A2.1). We first compute Δf by separating it into two parts, a part due to particles diffusing out of the box, Δf_{out} and a part from bath particles diffusing in, Δf_{in}:

$$\langle \Delta f_{\text{out}} \rangle = \frac{\langle -\Delta N_{R,\text{out}} + \Delta N_{B,\text{out}} \rangle}{N_0} \tag{129}$$

$$= \frac{\left\langle -\Delta N_{\text{out}} \frac{1+f}{2} + \Delta N_{\text{out}} \frac{1-f}{2} \right\rangle}{\langle N \rangle} \tag{130}$$

$$= -f \frac{\langle \Delta N_{\text{out}} \rangle}{N_0} \tag{131}$$

$$\langle \Delta f_{\text{in}} \rangle = \frac{\langle \Delta N_{R,\text{in}} - \Delta N_{B,\text{in}} \rangle}{N_0} \tag{132}$$

$$= \frac{\left\langle \Delta N_{\text{in}} \frac{1}{2} - \Delta N_{\text{in}} \frac{1}{2} \right\rangle}{N_0} \tag{133}$$

$$= 0 \tag{134}$$

Putting these two together, we obtain:

$$\langle \Delta f \rangle = -f \frac{\langle \Delta N_{\text{out}} \rangle}{N_0} \tag{135}$$

Similarly, we can compute the variance of Δf as:

$$\langle \Delta f^2 \rangle = \frac{\langle \Delta N_{\text{out}}^2 \rangle}{N_0^2} + \frac{\langle \Delta N_{\text{in}}^2 \rangle}{N_0^2} \tag{136}$$

In the derivations of $\langle \Delta f \rangle$ and $\langle \Delta f^2 \rangle$ we assumed that the timestep is small enough that essentially only on the order of unit changes occur in the number of particles. In this limit the probability that the particles leaving a box with composition f are all red/blue is $\frac{1 \pm f}{2}$.

To compute the quantity $\langle \Delta N_{\text{out}} \rangle$ we imagine a box surrounded by vacuum. At time t=0, the probability for a particle to be located inside the box is uniform, and is equal to $P(\mathbf{x}, 0) = \frac{1}{L_0^2}$. We imagine at the boundaries the probability decays to zero over a distance σ on the order of particle size. The particles can diffuse out of the box with a diffusion coefficient equal to D, the effective diffusion of particles in the many body liquid. After a timestep Δt, the change in the number of particles can be computed as:

$$\begin{aligned}
\langle \Delta N_{\text{out}} \rangle &= N_0 \int_{\text{vol}} \frac{dP(\mathbf{x}, 0)}{dt} dV \Delta t && (137)\\
&= N_0 \int_{\text{vol}} \nabla \cdot D \nabla P(\mathbf{x}, 0) dV \Delta t && (138)\\
&= N_0 \int_{\text{bdd}} D \nabla P(\mathbf{x}, 0) \cdot \vec{n} dS \Delta t && (139)\\
&= N_0 D \Delta t \frac{1}{L_0^2 \sigma} 4 L_0 && (140)\\
&= 4 \sqrt{N_0 \rho} D \Delta t \frac{1}{\sigma} && (141)
\end{aligned}$$

To compute the variance $\langle \Delta N_{\text{out}}^2 \rangle$, we consider flux of particles in and out of the probe

volume and obtain:

$$\langle \Delta N_{\text{out}}^2 \rangle = 2\rho\sqrt{N_0} D \Delta t \tag{142}$$

$$\langle \Delta N_{\text{in}}^2 \rangle = 2\rho\sqrt{N_0} D(f=0) \Delta t \tag{143}$$

Combining Eqs. 135, 136, 141, 142 and 143, and allowing the diffusion of the liquid to change as a function of composition, we write the final equation of motion for the composition as:

$$\frac{df}{dt} = -4\sqrt{\frac{\rho}{N_0}}\frac{fD(f)}{\sigma} + \frac{\sqrt{2\rho(D(f)+D(0))}}{\sqrt{N_0^3}}\eta \tag{144}$$

where η is a Gaussian noise of zero mean and unit variance. The Fokker-Planck equation resulting from Eq. 144, which we interpret in the Itô sense, is:

$$\frac{dP}{dt} = \frac{4}{\sigma}\sqrt{\frac{\rho}{N_0}}\frac{d(D(f)fP)}{df} + \frac{2\rho}{\sqrt{N_0^3}}\frac{d^2((D(f)+D(0))P)}{df^2}. \tag{145}$$

In order to derive the condition for phase separation, we again ignore the linear part of the diffusion coefficient as a function of Pe, and write $D(f) \equiv D_{eq} + (1-f^2)b(\tau)\text{Pe}^2$. Setting $dP/dt = 0$ in Eq. 145, we obtain the solution:

$$P(f) = C_0 \exp\left[-\frac{N_0}{\sqrt{\rho}\sigma}f^2\right]\left(2D(0) - f^2 b(\tau)\text{Pe}^2\right)^{-\gamma} \tag{146}$$

$$= \frac{C_0}{(2D(0))^\beta}\left(1 + \left(\frac{\gamma b(\tau)\text{Pe}^2}{2D(0)} - \frac{N_0}{\sqrt{\rho}\sigma}\right)f^2 + \mathcal{O}(f^4)\right) \tag{147}$$

where C_0 is the normalization, $\gamma = \dfrac{D(0)\frac{N_0}{\sqrt{\rho}\sigma}}{b(\tau)\text{Pe}^2} + 1$, and in going from the first line to the second line we Taylor expanded.

We define $\dfrac{N_0}{\sqrt{\rho}\sigma} = \lambda$, the constant in Eq. 2.37. When $\lambda > \dfrac{b(\tau)\text{Pe}^2}{D_{eq} + b(\tau)\text{Pe}^2}$, the steady state solution is peaked at $f = 0$, meaning the system will be mixed. However, when

$\lambda < \dfrac{b(\tau)\mathrm{Pe}^2}{D_{eq} + b(\tau)\mathrm{Pe}^2}$, the steady state solution has a minimum at $f = 0$, and the system will phase-separate. λ is thus the value of $\alpha/2\beta$ in Eq. 128 for our system.

In our simulations, we obtained that the condition for phase separation is roughly $\dfrac{b(\tau)\mathrm{Pe}^2}{D_{eq} + b(\tau)\mathrm{Pe}^2} > 0.5$. In other words, $\mathrm{Pe}^2 b(\tau) > D_{eq}$ for a phase transition. By comparison, since $\sigma = 1$ and $\rho = 0.45$, by setting $L_0 = \sigma$ our predicted condition for a phase transition is $\dfrac{b(\tau)\mathrm{Pe}^2}{D_{eq} + b(\tau)\mathrm{Pe}^2} > 0.67$. In other words, our simple estimates for the phenomenological constants in the composition fluctuation equation predict a phase transition when $\mathrm{Pe}^2 b(\tau) > 0.67 D_{eq}/0.33$. Given how simplistic our phenomenological composition fluctuation equation is, this prediction is reasonable. For a choice of $L_0 = 0.9\sigma$, the prediction from our theory matches numerical results.

References

[1] Aldrovandi, R. R. *Special matrices of mathematical physics : stochastic, circulant, and Bell matrices*. World Scientific, **2001**.

[2] Amir, A.; Hatano, N.; Nelson, D. R. Non-Hermitian localization in biological networks. *Phys. Rev. E*, 93(4):042310, **2016**.

[3] Ballerini, M.; Cabibbo, N.; Candelier, R.; Cavagna, A.; Cisbani, E.; Giardina, I.; Lecomte, V.; Orlandi, A.; Parisi, G.; Procaccini, A.; et al. Interaction ruling animal collective behavior depends on topological rather than metric distance: Evidence from a field study. *Proc. Natl. Acad. Sci. U. S. A.*, 105(4):1232–1237, **2008**.

[4] Banerjee, S.; Gardel, M. L.; Schwarz, U. S. The actin cytoskeleton as an active adaptive material. *Annu. Rev. Conden. Ma. P.*, 11(1):421–439, **2020**.

[5] Barato, A. C.; Seifert, U. Thermodynamic Uncertainty Relation for Biomolecular Processes. *Phys. Rev. Lett.*, 114(15):158101, **2015**.

[6] Barato, A. C.; Seifert, U. Coherence of biochemical oscillations is bounded by driving force and network topology. *Phys. Rev. E*, 95(6):062409, **2017**.

[7] Barkai, N.; Leibler, S. Biological rhythms: Circadian clocks limited by noise. *Nature*, 403(6767):267–268, **2000**.

[8] Battle, C.; Broedersz, C.; Fakhri, N.; Geyer, V.; Howard, J.; Schmidt, C.; MacKintosh, F. Broken detailed balance at mesoscopic scales in active biological systems. *Science*, 351(6268):604–607, **2016**.

[9] Bedeaux, D.; Weeks, J. D. Correlation functions in the capillary wave model of the liquid-vapor interface. *J. Chem. Phys.*, 82(2):972–979, **1985**.

[10] Bennett, C. H. Dissipation-error tradeoff in proofreading. *Biosystems*, 11(2-3):85–91, **1979**.

[11] Bialké, J.; Löwen, H.; Speck, T. Microscopic theory for the phase separation of self-propelled repulsive disks. *Europhys. Lett.*, 103(3):30008, **2013**.

[12] Bialké, J.; Siebert, J. T.; Lowen, H.; Speck, T. Negative Interfacial Tension in Phase-Separated Active Brownian Particles. *Phys. Rev. Lett.*, 115(9):098301, **2015**.

[13] Bouchaud, J.-P.; Georges, A. Anomalous diffusion in disordered media: Statistical mechanisms, models and physical applications. *Phys. Rep.*, 195(4-5):127–293, **1990**.

[14] Bowman, G. R.; Meng, L.; Huang, X. Quantitative comparison of alternative methods for coarse-graining biological networks. *J. Chem. Phys.*, 139(12):121905, **2013**.

[15] Budnar, S.; Husain, K. B.; Gomez, G. A.; Naghibosadat, M.; Varma, A.; Verma, S.; Hamilton, N. A.; Morris, R. G.; Yap, A. S. Anillin Promotes Cell Contractility by Cyclic Resetting of RhoA Residence Kinetics. *Dev. Cell*, 49(6):894–906.e12, **2019**.

[16] Burkholder, E. W.; Brady, J. F. Tracer diffusion in active suspensions. *Phys. Rev. E*, 95:052605, **2017**.

[17] Buttinoni, I.; Bialké, J.; Kümmel, F.; Löwen, H.; Bechinger, C.; Speck, T. Dynamical Clustering and Phase Separation in Suspensions of Self-Propelled Colloidal Particles. *Phys. Rev. Lett.*, 110(23):238301, **2013**.

[18] Cagnetta, F.; Evans, M. R.; Marenduzzo, D. Kinetic roughening in active interfaces. *EPJ Web Conf.*, 230:00001, **2020**.

[19] Cao, Y.; Wang, H.; Ouyang, Q.; Tu, Y. The free-energy cost of accurate biochemical oscillations. *Nature Phys.*, 11(9):772–778, **2015**.

[20] Cates, M. E.; Tailleur, J. Motility-Induced Phase Separation. *Annu. Rev. Conden. Ma. P.*, 6(1):219–244, **2015**.

[21] Chandler, D. Gaussian field model of fluids with an application to polymeric fluids. *Phys. Rev. E*, 48(4):2898–2905, **1993**.

[22] Crisanti, A.; Paladin, G.; Vulpiani, A. *Products of random matrices in statistical physics*. Springer, **1993**.

[23] Crooks, G. E. Entropy production fluctuation theorem and the nonequilibrium work relation for free energy differences. *Phys. Rev. E*, 60(3):2721–2726, **1999**.

[24] Dasbiswas, K.; Mandadapu, K. K.; Vaikuntanathan, S. Topological localization in out-of-equilibrium dissipative systems. *Proc. Natl. Acad. Sci. U. S. A.*, 115(39):E9031–E9040, **2018**.

[25] De Groot, S. R.; Mazur, P. *Non-Equilibrium Thermodynamics*. North-Holland Publishing Company, Amsterdam, **2016**.

[26] Dean, D. S.; Drummond, I. T.; Horgan, R. R. Effective transport properties for diffusion in random media. *J. Stat. Mech.-Theory E.*, 2007(07):P07013–P07013, **2007**.

[27] Dean, D. S. Langevin equation for the density of a system of interacting Langevin processes. *J. Phys. A.-Math. Gen.*, 29(24):L613–L617, **1996**.

[28] Dean, D. S.; Gersberg, P.; Holdsworth, P. C. W. The effect of driving on model C interfaces. *J. Stat. Mech.-Theory E.*, 2020(3):033206, **2020**.

[29] del Junco, C.; Tociu, L.; Vaikuntanathan, S. Energy dissipation and fluctuations in a driven liquid. *Proc. Natl. Acad. Sci. U. S. A.*, 115(14):3569–3574, **2018**.

[30] del Junco, C.; Vaikuntanathan, S. Interface height fluctuations and surface tension of driven liquids with time-dependent dynamics. *J. Chem. Phys.*, 150(9):094708, **2019**.

[31] del Junco, C.; Vaikuntanathan, S. High chemical affinity increases the robustness of biochemical oscillations. *Phys. Rev. E*, 101:012410, **2020**.

[32] del Junco, C.; Vaikuntanathan, S. Robust oscillations in multi-cyclic markov state models of biochemical clocks. *J. Chem. Phys.*, 152(5):055101, **2020**.

[33] Démery, V.; Bénichou, O.; Jacquin, H. Generalized Langevin equations for a driven tracer in dense soft colloids: construction and applications. *New J. Phys.*, 16(5):053032, **2014**.

[34] Derks, D.; Aarts, D. G. A. L.; Bonn, D.; Lekkerkerker, H. N. W.; Imhof, A. Suppression of Thermally Excited Capillary Waves by Shear Flow. *Phys. Rev. Lett.*, 97(3):038301, **2006**.

[35] Derrida, B.; Mecheri, K.; Pichard, J. L. Lyapunov exponents of products of random matrices: weak disorder expansion. Application to localisation. *J. Phys. France*, 48:733–740, **1987**.

[36] Derrida, B. Velocity and diffusion constant of a periodic one-dimensional hopping model. *J. Stat. Phys.*, 31(3):433–450, **1983**.

[37] Dombrowski, C.; Cisneros, L.; Chatkaew, S.; Goldstein, R. E.; Kessler, J. O. Self-concentration and large-scale coherence in bacterial dynamics. *Phys. Rev. Lett.*, 93:098103, **2004**.

[38] Dzubiella, J.; Hoffmann, G. P.; Löwen, H. Lane formation in colloidal mixtures driven by an external field. *Phys. Rev. E*, 65:021402, **2002**.

[39] Fei, C.; Cao, Y.; Ouyang, Q.; Tu, Y. Design principles for enhancing phase sensitivity and suppressing phase fluctuations simultaneously in biochemical oscillatory systems. *Nat. Commun.*, 9(1):1434, **2018**.

[40] Fily, Y.; Marchetti, M. C. Athermal Phase Separation of Self-Propelled Particles with No Alignment. *Phys. Rev. Lett.*, 108(23):235702, **2012**.

[41] Fisher, D. S. Random walks in random environments. *Phys. Rev. A*, 30:960–964, **1984**.

[42] Fisher, M. P. A.; Fisher, D. S.; Weeks, J. D. Agreement of Capillary-Wave Theory with Exact Results for the Interface Profile of the Two-Dimensional Ising Model. *Phys. Rev. Lett.*, 48(5):368–368, **1982**.

[43] Fodor, É.; Nardini, C.; Cates, M. E.; Tailleur, J.; Visco, P.; van Wijland, F. How Far from Equilibrium Is Active Matter? *Phys. Rev. Lett.*, 117(3):038103, **2016**.

[44] François, P.; Despierre, N.; Siggia, E. D. Adaptive Temperature Compensation in Circadian Oscillations. *PLoS Comput. Biol.*, 8(7):e1002585, **2012**.

[45] Gardel, M. L.; Shin, J. H.; MacKintosh, F. C.; Mahadevan, L.; Matsudaira, P.; Weitz, D. A. Elastic behavior of cross-linked and bundled actin networks. *Science*, 304(5675):1301–1305, **2004**.

[46] Gingrich, T. R.; Horowitz, J. M.; Perunov, N.; England, J. L. Dissipation Bounds All Steady-State Current Fluctuations. *Phys. Rev. Lett.*, 116(12):120601, **2016**.

[47] Grünwald, M.; Tricard, S.; Whitesides, G. M.; Geissler, P. L. Exploiting non-equilibrium phase separation for self-assembly. *Soft Matter*, 12(5):1517–1524, **2016**.

[48] Grzybowski, B. A.; Fitzner, K.; Paczesny, J.; Granick, S. From dynamic self-assembly to networked chemical systems. *Chem. Soc. Rev.*, 46(18):5647–5678, **2017**.

[49] Han, M.; Yan, J.; Granick, S.; Luijten, E. Effective temperature concept evaluated in an active colloid mixture. *Proc. Natl. Acad. Sci. U. S. A.*, 114(29):7513–7518, **2017**.

[50] Hancock, B.; Baskaran, A. Statistical mechanics and hydrodynamics of self-propelled hard spheres. *J. Stat. Mech.-Theory E.*, 2017(3):033205, **2017**.

[51] Hanggi, P. Driven Quantum Systems. In Dittrich, T.; Hanggi, P.; Ingold, G.-L.; Kramer, B.; Schon, G.; Zwerger, W., eds., *Quantum Transp. Dissipation*, chapter 5, pages 249–286. Wiley-VCH, **1998**.

[52] Harada, T.; Sasa, S.-i. Equality connecting energy dissipation with a violation of the fluctuation-response relation. *Phys. Rev. Lett.*, 95:130602, **2005**.

[53] Harada, T.; Sasa, S.-i. Energy dissipation and violation of the fluctuation-response relation in nonequilibrium Langevin systems. *Phys. Rev. E*, 73(2):026131, **2006**.

[54] Hatakeyama, T. S.; Kaneko, K. Reciprocity Between Robustness of Period and Plasticity of Phase in Biological Clocks. *Phys. Rev. Lett.*, 115(21):218101, **2015**.

[55] Hermann, S.; de las Heras, D.; Schmidt, M. Non-negative interfacial tension in phase-separated active brownian particles. *Phys. Rev. Lett.*, 123:268002, **2019**.

[56] Hong, L.; Lavrentovich, D. O.; Chavan, A.; Leypunskiy, E.; Li, E.; Matthews, C.; Li-Wang, A.; Rust, M. J.; Dinner, A. R. Bayesian modeling reveals metabolite-dependent ultrasensitivity in the cyanobacterial circadian clock. *Mol. Syst. Biol.*, 16(6):e9355, **2020**.

[57] Hopfield, J. J. Kinetic Proofreading: A New Mechanism for Reducing Errors in Biosynthetic Processes Requiring High Specificity (protein synthesis/DNA replication/amino-acid recognition). *Proc. Natl. Acad. Sci. U. S. A.*, 71(10):4135–4139, **1974**.

[58] Horowitz, J.; Jarzynski, C. Illustrative example of the relationship between dissipation and relative entropy. *Phys. Rev. E*, 79(2):021106, **2009**.

[59] Hummer, G.; Garde, S.; Garcia, A. E.; Pohorille, A.; Pratt, L. R. An information theory model of hydrophobic interactions. *Proc. Natl. Acad. Sci. U. S. A.*, 93(17):8951–8955, **1996**.

[60] Hummer, G.; Szabo, A. Free energy reconstruction from nonequilibrium single-molecule pulling experiments. *Proc. Natl. Acad. Sci. U. S. A.*, 98(7):3658–3661, **2001**.

[61] J Evans, D.; P Morriss, G. *Statistical mechanics of nonequilbrium liquids*. ANU Press, Canberra, **2007**.

[62] Jarzynski, C. Nonequilibrium equality for free energy differences. *Phys. Rev. Lett.*, 78:2690–2693, **1997**.

[63] Johnson, C. H.; Egli, M. Metabolic compensation and circadian resilience in prokaryotic cyanobacteria. *Annu. Rev. Biochem.*, 83:221–47, **2014**.

[64] Johnson, C. H.; Stewart, P. L.; Egli, M. The cyanobacterial circadian system: from biophysics to bioevolution. *Annu. Rev. Biophys.*, 40:143–67, **2011**.

[65] Jones, J. E. On the Determination of Molecular Fields. II. From the Equation of State of a Gas. *Proc. R. Soc. A-Math. Phy.*, 106(738):463–477, **1924**.

[66] Jülicher, F.; Grill, S. W.; Salbreux, G. Hydrodynamic theory of active matter. *Rep. Prog. Phys.*, 81(7):076601, **2018**.

[67] Klymko, K.; Geissler, P. L.; Whitelam, S. Microscopic origin and macroscopic implications of lane formation in mixtures of oppositely driven particles. *Phys. Rev. E*, 94:022608, **2016**.

[68] Krüger, M.; Dean, D. S. A gaussian theory for fluctuations in simple liquids. *J. Chem. Phys.*, 146(13):134507, **2017**.

[69] Kümmel, F.; ten Hagen, B.; Wittkowski, R.; Buttinoni, I.; Eichhorn, R.; Volpe, G.; Löwen, H.; Bechinger, C. Circular Motion of Asymmetric Self-Propelling Particles. *Phys. Rev. Lett.*, 110(19):198302, **2013**.

[70] Lan, G.; Sartori, P.; Neumann, S.; Sourjik, V.; Tu, Y. The energy-speed-accuracy trade-off in sensory adaptation. *Nature Phys.*, 8(5):422–428, **2012**.

[71] Lee, C. F. Interface stability, interface fluctuations, and the Gibbs-Thomson relationship in motility-induced phase separations. *Soft Matter*, 13(2):376–385, **2017**.

[72] Leung, K.; Mon, K.; Vallés, J.; Zia, R. Suppression of Interface Roughness in Driven Nonequilibrium Systems. *Phys. Rev. Lett.*, 61(15):1744–1747, **1988**.

[73] Leung, K. T.; Zia, R. K. P. Anomalous interfacial correlations in non-equilibrium anisotropic systems. *J. Phys. A-Math. Gen.*, 26(16):L737–L741, **1993**.

[74] Leypunskiy, E.; Lin, J.; Yoo, H.; Lee, U.; Dinner, A. R.; Rust, M. J. The cyanobacterial circadian clock follows midday in vivo and in vitro. *Elife*, 6, **2017**.

[75] Liebchen, B.; Levis, D. Collective Behavior of Chiral Active Matter: Pattern Formation and Enhanced Flocking. *Phys. Rev. Lett.*, 119(5):058002, **2017**.

[76] Lifson, S.; Jackson, J. L. On the self-diffusion of ions in a polyelectrolyte solution. *J. Chem. Phys.*, 36(9):2410–2414, **1962**.

[77] Mandal, D.; Klymko, K.; DeWeese, M. R. Entropy production and fluctuation theorems for active matter. *Phys. Rev. Lett.*, 119:258001, **2017**.

[78] Marchetti, M. C.; Joanny, J. F.; Ramaswamy, S.; Liverpool, T. B.; Prost, J.; Rao, M.; Simha, R. A. Hydrodynamics of soft active matter. *Rev. Mod. Phys.*, 85:1143–1189, **2013**.

[79] Marsland, R.; Cui, W.; Horowitz, J. M. The thermodynamic uncertainty relation in biochemical oscillations. *J. R. Soc. Interface*, 16(154):20190098, **2019**.

[80] Mayer, A.; Mora, T.; Rivoire, O.; Walczak, A. M. Diversity of immune strategies explained by adaptation to pathogen statistics. *Proc. Natl. Acad. Sci. U. S. A.*, 113(31):8630–8635, **2016**.

[81] McCandlish, S. R.; Baskaran, A.; Hagan, M. F. Spontaneous segregation of self-propelled particles with different motilities. *Soft Matter*, 8(8):2527, **2012**.

[82] McQuarrie, D. A. *Statistical Mechanics*. University Science Books, **2000**.

[83] Mehta, P.; Schwab, D. J. Energetic costs of cellular computation. *Proc. Natl. Acad. Sci. U. S. A.*, 109(44):17978–17982, **2012**.

[84] Mihalcescu, I.; Hsing, W.; Leibler, S. Resilient circadian oscillator revealed in individual cyanobacteria. *Nature*, 430(6995):81, **2004**.

[85] Milo, R.; Phillips, R. *Cell biology by the numbers*. Garland Science, **2015**.

[86] Morelli, L. G.; Jülicher, F. Precision of Genetic Oscillators and Clocks. *Phys. Rev. Lett.*, 98(22):228101, **2007**.

[87] Mullin, T. Coarsening of Self-Organized Clusters in Binary Mixtures of Particles. *Phys. Rev. Lett.*, 84(20):4741–4744, **2000**.

[88] Murugan, A.; Huse, D. A.; Leibler, S. Speed, dissipation, and error in kinetic proofreading. *Proc. Natl. Acad. Sci. U. S. A.*, 109(30):12034–9, **2012**.

[89] Nakajima, M.; Imai, K.; Ito, H.; Nishiwaki, T.; Murayama, Y.; Iwasaki, H.; Oyama, T.; Kondo, T. Reconstitution of circadian oscillation of cyanobacterial KaiC phosphorylation in vitro. *Science*, 308(5720):414–415, **2005**.

[90] Narayan, V.; Ramaswamy, S.; Menon, N. Long-lived giant number fluctuations in a swarming granular nematic. *Science*, 317(5834):105–8, **2007**.

[91] Nemoto, T.; Fodor, E.; Cates, M. E.; Jack, R. L.; Tailleur, J. Optimizing active work: Dynamical phase transitions, collective motion, and jamming. *Phys. Rev. E*, 99:022605, **2019**.

[92] Nguyen, B.; Seifert, U.; Barato, A. C. Phase transition in thermodynamically consistent biochemical oscillators. *J. Chem. Phys.*, 149(4):045101, **2018**.

[93] Nguyen, N. H. P.; Klotsa, D.; Engel, M.; Glotzer, S. C. Emergent collective phenomena in a mixture of hard shapes through active rotation. *Phys. Rev. Lett.*, 112:075701, **2014**.

[94] Ninio, J. Kinetic amplification of enzyme discrimination. *Biochimie*, 57(5):587–595, **1975**.

[95] Novák, B.; Tyson, J. J. Design principles of biochemical oscillators. *Nat. Rev. Mol. Cell Bio.*, 9(12):981–991, **2008**.

[96] Onsager, L. Crystal Statistics. I. A Two-Dimensional Model with an Order-Disorder Transition. *Phys. Rev.*, 65(3-4):117–149, **1944**.

[97] Paijmans, J.; Lubensky, D. K.; ten Wolde, P. R. A thermodynamically consistent model of the post-translational Kai circadian clock. *PLOS Comput. Biol.*, 13(3):e1005415, **2017**.

[98] Paijmans, J.; Lubensky, D. K.; ten Wolde, P. R. Period Robustness and Entrainability of the Kai System to Changing Nucleotide Concentrations. *Biophys. J.*, 113(1):157–173, **2017**.

[99] Palacci, J.; Sacanna, S.; Steinberg, A. P.; Pine, D. J.; Chaikin, P. M. Living Crystals of Light-Activated Colloidal Surfers. *Science*, 339(6122):936–940, **2013**.

[100] Paliwal, S.; Prymidis, V.; Filion, L.; Dijkstra, M. Non-equilibrium surface tension of the vapour-liquid interface of active Lennard-Jones particles. *J. Chem. Phys.*, 147(8):084902, **2017**.

[101] Pande, V. S.; Beauchamp, K.; Bowman, G. R. Everything you wanted to know about Markov State Models but were afraid to ask. *Methods*, 52(1):99 – 105, **2010**. Protein Folding.

[102] Patch, A.; Sussman, D. M.; Yllanes, D.; Marchetti, M. C. Curvature-dependent tension and tangential flows at the interface of motility-induced phases. *Soft Matter*, 14(36):7435–7445, **2018**.

[103] Petroff, A. P.; Wu, X.-L.; Libchaber, A. Fast-moving bacteria self-organize into active two-dimensional crystals of rotating cells. *Phys. Rev. Lett.*, 114:158102, **2015**.

[104] Pittayakanchit, W.; Lu, Z.; Chew, J.; Rust, M. J.; Murugan, A. Biophysical clocks face a trade-off between internal and external noise resistance. *Elife*, 7, **2018**.

[105] Plimpton, S. Fast Parallel Algorithms for Short-Range Molecular Dynamics. *J. Comput. Phys.*, 117(1):1–19, **1995**.

[106] Pooley, C. M.; Yeomans, J. M. Stripe Formation in Differentially Forced Binary Systems. *Phys. Rev. Lett.*, 93(11):118001, **2004**.

[107] Qian, H. Reducing Intrinsic Biochemical Noise in Cells and Its Thermodynamic Limit. *J. Mol. Biol.*, 362(3):387–392, **2006**.

[108] Qian, H.; Qian, M. Pumped Biochemical Reactions, Nonequilibrium Circulation, and Stochastic Resonance. *Phys. Rev. Lett.*, 84(10):2271–2274, **2000**.

[109] Rademaker, T. J.; Bengio, E.; François, P. Attack and defense in cellular decision-making: Lessons from machine learning. *Phys. Rev. X*, 9:031012, **2019**.

[110] Redner, G. S.; Hagan, M. F.; Baskaran, A. Structure and dynamics of a phase-separating active colloidal fluid. *Phys. Rev. Lett.*, 110(5):055701, **2013**.

[111] Redner, G. S.; Wagner, C. G.; Baskaran, A.; Hagan, M. F. Classical Nucleation Theory Description of Active Colloid Assembly. *Phys. Rev. Lett.*, 117(14):148002, **2016**.

[112] Reuter, B.; Fackeldey, K.; Weber, M. Generalized Markov modeling of nonreversible molecular kinetics. *J. Chem. Phys.*, 150(17):174103, **2019**.

[113] Reuter, B.; Weber, M.; Fackeldey, K.; Rblitz, S.; Garcia, M. E. Generalized Markov State Modeling Method for Nonequilibrium Biomolecular Dynamics: Exemplified on Amyloid Conformational Dynamics Driven by an Oscillating Electric Field. *J. Chem. Theory Comput.*, 14(7):3579–3594, **2018**.

[114] Richard, D.; Löwen, H.; Speck, T. Nucleation pathway and kinetics of phase-separating active Brownian particles. *Soft Matter*, 12(24):5257–5264, **2016**.

[115] Röblitz, S.; Weber, M. Fuzzy spectral clustering by PCCA+: application to Markov state models and data classification. *Adv. Data. Anal. Classi.*, 7(2):147–179, **2013**.

[116] Rowlinson, J.; Widom, B. *Molecular Theory of Capillarity*. Clarendon Press, Oxford, **1982**.

[117] Rust, M. J.; Markson, J. S.; Lane, W. S.; Fisher, D. S.; O'Shea, E. K. Ordered Phosphorylation Governs Oscillation of a Three-Protein Circadian Clock. *Science*, 318(5851):809–812, **2007**.

[118] Rust, M. J.; Golden, S. S.; O'Shea, E. K. Light-Driven Changes in Energy Metabolism Directly Entrain the Cyanobacterial Circadian Oscillator. *Science*, 331(6014):220 LP – 223, **2011**.

[119] Sabrina, S.; Spellings, M.; Glotzer, S. C.; Bishop, K. J. M. Coarsening dynamics of binary liquids with active rotation. *Soft Matter*, 11(43):8409–8416, **2015**.

[120] Sackmann, E. K.; Fulton, A. L.; Beebe, D. J. The present and future role of microfluidics in biomedical research. *Nature*, 507(7491):181–189, **2014**.

[121] Santra, M.; Bagchi, B. Line tension of a two dimensional gas-liquid interface. *J. Chem. Phys.*, 131(8):84705–234704, **2009**.

[122] Schwartz, D. K.; Schlossman, M. L.; Kawamoto, E. H.; Kellogg, G. J.; Pershan, P. S.; Ocko, B. M. Thermal diffuse x-ray-scattering studies of the water-vapor interface. *Phys. Rev. A*, 41(10):5687–5690, **1990**.

[123] Seif, A.; Hafezi, M.; Jarzynski, C. Machine learning the thermodynamic arrow of time, arXiv:1909.12380v1, **2019**.

[124] Seifert, U. Stochastic thermodynamics, fluctuation theorems and molecular machines. *Rep. Prog. Phys.*, 75(75):126001–58, **2012**.

[125] Sekimoto, K. Kinetic Characterization of Heat Bath and the Energetics of Thermal Ratchet Models. *J. Phys. Soc. Jpn.*, 66(5):1234–1237, **1997**.

[126] Shankar, S.; Marchetti, M. C. Hidden entropy production and work fluctuations in an ideal active gas. *Phys. Rev. E*, 98:020604, **2018**.

[127] Sides, S. W.; Grest, G. S.; Lacasse, M.-D. Capillary waves at liquid-vapor interfaces: A molecular dynamics simulation. *Phys. Rev. E*, 60(6):6708–6713, **1999**.

[128] Smit, B.; Frenkel, D. Vapor-liquid equilibria of the two-dimensional Lennard-Jones fluid(s). *J. Chem. Phys.*, 941(10), **1991**.

[129] Solon, A. P.; Fily, Y.; Baskaran, A.; Cates, M. E.; Kafri, Y.; Kardar, M.; Tailleur, J. Pressure is not a state function for generic active fluids. *Nature Phys.*, 11(8):673–678, **2015**.

[130] Soni, V.; Bililign, E. S.; Magkiriadou, S.; Sacanna, S.; Bartolo, D.; Shelley, M. J.; Irvine, W. T. The odd free surface flows of a colloidal chiral fluid. *Nature Phys.*, 15(11):1188–1194, **2019**.

[131] Speck, T.; Bialké, J.; Menzel, A. M.; Löwen, H. Effective Cahn-Hilliard equation for the phase separation of active brownian particles. *Phys. Rev. Lett.*, 112(21):218304, **2014**.

[132] Stenhammar, J.; Wittkowski, R.; Marenduzzo, D.; Cates, M. E. Activity-Induced Phase Separation and Self-Assembly in Mixtures of Active and Passive Particles. *Phys. Rev. Lett.*, 114(1):018301, **2015**.

[133] Tailleur, J.; Cates, M. E. Statistical mechanics of interacting run-and-tumble bacteria. *Phys. Rev. Lett.*, 100(21):218103, **2008**.

[134] Takatori, S. C.; Brady, J. F. Towards a thermodynamics of active matter. *Phys. Rev. E*, 91(3):032117, **2015**.

[135] Takatori, S. C.; Sahu, A. Active contact forces drive nonequilibrium fluctuations in membrane vesicles. *Physical Review Letters*, 124(15), **2020**.

[136] Terauchi, K.; Kitayama, Y.; Nishiwaki, T.; Miwa, K.; Murayama, Y.; Oyama, T.; Kondo, T. ATPase activity of KaiC determines the basic timing for circadian clock of cyanobacteria. *Proc. Natl. Acad. Sci. U. S. A.*, 104(41):16377–16381, **2007**.

[137] Tociu, L.; Fodor, E.; Nemoto, T.; Vaikuntanathan, S. How dissipation constrains fluctuations in nonequilibrium liquids: Diffusion, structure, and biased interactions. *Phys. Rev. X*, 9:041026, **2019**.

[138] Tomita, J.; Nakajima, M.; Kondo, T.; Iwasaki, H. No Transcription-Translation Feedback in Circadian Rhythm of KaiC Phosphorylation. *Science*, 307(5707):251–254, **2005**.

[139] Tsai, J.-C.; Ye, F.; Rodriguez, J.; Gollub, J. P.; Lubensky, T. C. A chiral granular gas. *Phys. Rev. Lett.*, 94:214301, **2005**.

[140] Vaikuntanathan, S.; Geissler, P. L. Putting Water on a Lattice: The Importance of Long Wavelength Density Fluctuations in Theories of Hydrophobic and Interfacial Phenomena. *Phys. Rev. Lett.*, 112(2):020603, **2014**.

[141] Vaikuntanathan, S.; Gingrich, T. R.; Geissler, P. L. Dynamic phase transitions in simple driven kinetic networks. *Phys. Rev. E*, 89(6):062108, **2014**.

[142] Vaikuntanathan, S.; Rotskoff, G.; Hudson, A.; Geissler, P. L. Necessity of capillary modes in a minimal model of nanoscale hydrophobic solvation. *Proc. Natl. Acad. Sci. U. S. A.*, 113(16):E2224–E2230, **2016**.

[143] van Zon, J. S.; Lubensky, D. K.; Altena, P. R. H.; ten Wolde, P. R. An allosteric model of circadian KaiC phosphorylation. *Proc. Natl. Acad. Sci. U. S. A.*, 104(18):7420–7425, **2007**.

[144] van Zuiden, B. C.; Paulose, J.; Irvine, W. T. M.; Bartolo, D.; Vitelli, V. Spatiotemporal order and emergent edge currents in active spinner materials. *Proc. Natl. Acad. Sci. U. S. A.*, 113(46):12919–12924, **2016**.

[145] Vissers, T.; van Blaaderen, A.; Imhof, A. Band formation in mixtures of oppositely charged colloids driven by an AC electric field. *Phys. Rev. Lett.*, 106(22):228303, **2011**.

[146] Vissers, T.; Wysocki, A.; Rex, M.; Löwen, H.; Royall, C. P.; Imhof, A.; van Blaaderen, A. Lane formation in driven mixtures of oppositely charged colloids. *Soft Matter*, 7(6):2352, **2011**.

[147] Weeks, J. D.; Chandler, D.; Andersen, H. C. Role of Repulsive Forces in Determining the Equilibrium Structure of Simple Liquids. *J. Chem. Phys.*, 54(12):5237–5247, **1971**.

[148] Whitelam, S.; Klymko, K.; Mandal, D. Phase separation and large deviations of lattice active matter. *J. Chem. Phys.*, 148(15):154902, **2018**.

[149] Whitesides, G. M.; Grzybowski, B. Self-assembly at all scales. *Science*, 295(5564):2418–21, **2002**.

[150] Wierenga, H.; Ten Wolde, P. R.; Becker, N. B. Quantifying fluctuations in reversible enzymatic cycles and clocks. *Phys. Rev. E*, 97(4):042404, **2018**.

[151] Woelfle, M. A.; Ouyang, Y.; Phanvijhitsiri, K.; Johnson, C. H. The Adaptive Value of Circadian Clocks: An Experimental Assessment in Cyanobacteria. *Curr. Biol.*, 14(16):1481–1486, **2004**.

[152] Wysocki, A.; Löwen, H. Oscillatory driven colloidal binary mixtures: Axial segregation versus laning. *Phys. Rev. E*, 79(4):041408, **2009**.

[153] Yan, J.; Bae, S. C.; Granick, S. Rotating crystals of magnetic Janus colloids. *Soft Matter*, 11(1):147–153, **2015**.

[154] Yeo, K.; Lushi, E.; Vlahovska, P. M. Dynamics of inert spheres in active suspensions of micro-rotors. *Soft Matter*, 12(12):5645–5652, **2016**.

[155] Yoshida, T.; Murayama, Y.; Ito, H.; Kageyama, H.; Kondo, T. Nonparametric entrainment of the in vitro circadian phosphorylation rhythm of cyanobacterial KaiC by temperature cycle. *Proc. Natl. Acad. Sci. U. S. A.*, 106(5):1648–1653, **2009**.

[156] Zhang, D.; Cao, Y.; Ouyang, Q.; Tu, Y. The energy cost and optimal design for synchronization of coupled molecular oscillators. *Nature Physics*, 16(1):95–100, **2019**.

[157] Zia, R. K. P.; Leung, K. T. Interfacial correlation and dispersion in a non-equilibrium steady state system. *J. Phys. A-Math. Gen.*, 24(24):L1399–L1404, **1991**.